UNIVERSITY OF OKLAHOMA

GRADUATE COLLEGE

AN INTEGRATED LIDAR-XRF STUDY AND GEOMECHANICAL LITHOFACIES ANALYSIS OF THE LEONARDIAN UPPER BONE SPRING FORMATION, BONE CANYON, TEXAS:

A THESIS

SUBMITTED TO THE GRADUATE FACULTY

In partial fulfillment of the requirements for the

Degree of

MASTER OF SCIENCE

BY

TRAVIS OWEN OLIVER PLEMONS

Norman, Oklahoma

2019

AN INTEGRATED LIDAR-XRF STUDY AND GEOMECHANICAL LITHOFACIES ANALYSIS OF THE LEONARDIAN UPPER BONE SPRING FORMATION, BONE CANYON, TEXAS

A THESIS APPROVED FOR THE

CONOCOPHILLIPS SCHOOL OF GEOLOGY AND GEOPHYSICS

BY

Dr. John D. Pigott, Chair

Dr. Kulwadee Pigott

Dr. Brett Carpenter

This work is dedicated to God, my father Billy W. Plemons Jr., and my loving family

ACKNOWLEDGEMENTS

First and foremost, I would like to thank Dr. John Pigott for giving me an opportunity to fulfill my goal of becoming an exploration geoscientist. This project has been improved through his tireless efforts to coordinate research trips and inspire me to think critically of my research and the problems associated with it. I will never forget Dr. Pigott's enduring efforts to support his student's projects.

None of this research would have been possible if not for the National Park Service and the efforts of Dr. Jonena Hearst, along with the entirety of the Guadalupe Mountains National Park staff. From the first moment I began working with Dr. Hearst, she has always strived for the well-being of myself and colleagues working within the National Park. I am hopeful that the data collected from this will be used to further advance our understanding of the Delaware Basin. In addition to the vital research given to me, the peacefulness, fresh air and tranquility will always hold a special place in my memories.

I wish to thank the ConocoPhillips School of Geology and Geophysics for the resources and equipment provided in order to conduct my research. This includes use of the LiDAR scanning system, SilverSchmidt measuring device, GPS systems, transportation, accommodations, and facilities to write and conduct research. My gratitude is yours.

I also wish to thank the members of my committee, Dr. Kulwadee Pigott and Dr. Brett Carpenter for their time and invaluable suggestions regarding this research project. Your expertise led to the revision and overall improvement of this manuscript.

Thank you to my colleagues and friends for the fruitful conversations and comprehensive insight given on this project, including Tanner Shadoan, Travis Moreland, Christina Hamilton, Matt Lynch, Andrew Layden, Cyril Frazier, Sam Berg, and Andrew Brown. The special memories of laughter and hardships are enduring and will forever hold a special place in my heart.

Lastly, thank you to my wonderful fiancée Emily Anne Pool, who always encourages, always supports, and always loves unconditionally during the most trying times in life.

TABLE OF CONTENTS

List of Tables…….…….……x

List of Figures…….……..xi

ABSTRACT……...…….…..…xvi

1.INTRODUCTION

1.1 Problem Statement…….……..…….…….……....1

1.2. Background……..…….1

1.2 Previous Work….. ……..……...….6

1.3 Study Area……..….....10

2. GEOLOGIC BACKGROUND

2.1 Wolfcampian Deposition……..…..…..14

2.2 Bone Spring Deposition…….……...….……..16

2.3 Guadalupian-Ochoan Deposition……...…….…….21

2.4 Tectonic History……..……23

2.5 Fault History……..…..…….27

3. METHODS

3.1 Field Methods……..……30

3.2 Light Detection and Range Device Collection Mechanics……..……31

3.3 LiDAR Processing……...33

3.4 X-Ray Fluorescence Data Collection and Processing……..……...35

3.5 SilverSchmidt Data Collection and Mechanics……..……....…..……...36

4. DATA AND OUTCROP CHARACTERISTICS…….....38

4.1. Petrography and Outcrop Descriptions……...…….……..39

4.2. XRF Data…….……..48

4.3 SilverSchmidt data……..49

5. RESULTS

5.1. LiDAR Constrained Stratigraphy…….……..…..……..51

5.2. Split-FX…….. ……..……...……...……...53

5.3. Fracture Populations…..……..……...54

5.3.1. North Wall: Cutoff Conglomerate……...55

5.3.2. North Wall: Cutoff Channel Sand……58

5.3.3. Scan Position 3: Bone Spring unconformity……60

5.3.4. Transect 7: Bone Spring Carbonate A……..…….……..65

5.3.5. Transect 6: Bone Spring Carbonate B…….……....70

5.3.6. Population Summary……72

5.4 XRF cluster analysis……...…….……..……..…..……..72

5.4.1. Transect 1 (1st Bone Spring Sand)……..……..74

5.4.2. Transect 6 (1st Bone Spring Carbonate A)……...76

5.4.3. Transect 7 (1st Bone Spring Carbonate B)……...77

5.5. XRF and LiDAR Constrained Lithology……78

5.5.1. 1st Bone Spring Carbonate B…….……..79

5.5.2. 1st Bone Spring Carbonate A…….……...……...80

5.5.3. Upper Bone Spring Limestone …….…….……..81

5.5.4. Cutoff Sand……..82

6. DISCUSSION

6.1. Anoxic/Euxinic Proxy Correlation.…..……..…...……83

6.2. Trends in Rebound Hardness…..……...…....……...…….88

6.3. Fracture Characterization ……..……...……...…...89

6.3.1. Fracture Orientation Distribution..……...……89

6.3.2. Distribution of Fracture Density and Bed Thickness……...……91

6.3.3. 2D Geomechanics Model……...…….. ……...……92

6.4. Implications for Future Work……..……...……94

7. CONCLUSIONS……...……..……..……...…..96

REFERENCES…….....…….98

APPENDIX A……...103

APPENDIX B……...108

LIST OF TABLES

Table 1. Empirical correlations from several studies attempting to derive Unconfined Compressive Strength from Schmidt Hammer Hardness. Modified from Rajabi et al., (2017)……..10

Table 2. Thin section descriptions of samples collected from Bone Canyon……..43

LIST OF FIGURES

Figure 1: Relationships of stress and strain, showing points of elastic and plastic strain, as well as maximum stress, failure, and residual stress (Holt, 2011)……..……..5

Figure 2: Fracture communication with shale matrix and associated shale gas (Zhang et al., 2018)……..5

Figure 3. Idealized cross section of the Delaware Basin, from NW to SE. Red box indicates relative stratigraphic position of study area (from Scholle site, 2002)……..……..9

Figure 4. Satellite view of area surrounding Guadalupe Mountains National Park. Upper Left: Illustration of the Permian Basin, outlining the Delaware, Midland Basins, as well as the Diablo Platform, Central Basin Platform, Northwestern Shelf, Val Verde Basin, and Southern Shelf. Red box on both the satellite image and upper left image mark the approximate position of the Bone Canyon outcrop. Modified from (Stolz, 2014)……..……12

Figure 5: Bone Canyon with relative sample positions highlighted. Waypoint flags illustrated mark GPS positions of sampling locations. Note that samples 050 and 051 were omitted from this study……..……13

Figure 6: Stratigraphic column of the Permian Basin region. From Yang and Dorobek (1995)……..……...13

Figure 7. Idealized stratigraphic column illustrating early through late Permian sedimentation within the Bone Canyon outcrop. Red circles mark sections observed in the study area, with transects marked to the right. Modified from Alabbad, 2017…….……...16

Figure 8: Bone Canyon outcrop, Bone Spring formation, 1st Carbonate B. Taken at Transect measurement 2. Note the presence of bedded chert, common in the lower part of the canyon..…….……..20

Figure 9: Illustration of simplified reciprocal sedimentation within the Delaware Basin, during high stand carbonate deposition with mud supported debris flows, and Low stand siliciclastic deposition dominated by platform sandstones and turbidites. Adapted from Scholle, 2002 through www.sepmstrata.org......**21**

Figure 10: Outcrop of Brushy Canyon formation within Bone Canyon. This section was subject to studies conducted by Alabbad (2017) in which fracture orientations were interpreted and recorded……..…….……23

Figure 11: Transgression of tectonic events from the early Pennsylvanian to present. Modified from Kullman, (1999)…….……26

Figure 12: Outline of Delaware Basin, with relation to Tobosa Basin, Texas Arch and Diablo Arch. Modified from Adams, (1965)……..27

Figure 13: Cenozoic fault map of west Texas and Southeastern New Mexico. Red Square marks relative position of study area. Orange Pin marks GPS position of Bone Canyon. After Kullman, (1999)……..29

Figure 14: Relation of LiDAR scan positions to field-measured transects (red) within Bone Canyon……..……..34

Figure 15: Point cloud data displayed in true color. Also shown is scan position 002 and formation boundaries of the Bone Spring/Cutoff formations (bottom line) and Brushy Canyon/Cutoff formations (Top line)……...…….35

Figure 16: Correlation of SilverSchmidt Q value to rebound ratio and unconfined compressive strength, Modified from Wang (2018)……..……...38

Figure 17: (A) Transect 1 measured interval, inferred 1st Bone Spring Carbonaceous Sand, (B) Transect 6 measured interval, interpreted Bone Spring Carbonate B, (C) Transect 8 measured interval, inferred Bone Spring Limestone, (D) Transect 9 measured section, interpreted Cutoff channel sand. Power 4x…….....45

Figure 18: (A) Siliceous mudstone, from sample OU-2154-PMNM. Note Radiolarian present within slide. Benthic foraminifera present with ~40% biogenic silica grains. Dolomitization is dominated by planar-rhombic structure, cloudy centers with hypotropic mosaic. (B) Radiolarian-rich Mudstone, identified within the Bone Spring Carbonate A. Vuggular pore space identified with dissolution-dominated diagenetic features were observed. (C) Predominantly biogenic chert, with presence of micritic calcite and fossils also present. Trace feldspar (<5%) observed sparsely. Kerogen-filled crinoids due to center dissolution also present. Note presence of radial ooid, interpreted to be transported from upward shelf, due to its trace amount (<1%). (D) From inferred Bone Spring Limestone; Radiolarian-dominated mudstone. Cementation is micrite with high volumes of kerogen-filled fractures present within the sample. Chert replacement of crinoids are common throughout, with biogenically sourced silica also present. Outcrop photograph can be observed in Figure 14C. Power 4x, CPL……..……..……46

Figure 19: (A) Arkosic Quartzarenite identified within the Cutoff conglomeritic unit. Note the presence of secondary fracture porosity. (B) Calclithite identified within the Cutoff Formation in Bone Canyon. Two generations of isopachous cement can be observed, giving evidence for re-cementation involved with sub-aqueous, shallow exposure. Hydrocarbon staining around cementation rims indicates later hydrocarbon migration. Power 4x, CPL…… 47

Figure 20: (A) Southwest oriented photograph of Bone Canyon, with the Brushy Canyon formation defined. (B) inferred later Guadalupian sedimentation……..…….47

Figure 21: Chert-cemented, high angle fractures identified with an approximate NE-SW orientation. Complimentary, shallow angle fracture with chert cementation also identified, with chert nodules being prevalent. Fractures labeled by red arrow…….48

Figure 22: Correlation of SilverSchmidt Q readings with XRF-derived quartz (left) and dolomite (right) mineralogy…….50

Figure 23: Approximation of stratigraphic positions within Bone Canyon. It should be noted that the Bone Spring Limestone is combined with the Bone Spring Carbonate A, for the purpose of clarity within a compressed satellite image. Pseudo gamma-ray collected from XRF data is also recorded, including an inferred sea level curve……..……...…….52

Figure 24: Relation of field-measured transects to Bone Canyon outcrop formations illustrating lateral variation……..……..53

Figure 25: Ground truth (left) fracture orientations measured within the Bone Spring outcrop, and (right) fracture orientations measured in Split-FX. The substantial increase between data collected from the field and LiDAR extraction should be noted, with 6 field measurements in ground truth measurements and 545 extracted through Split-FX……..…….……...55

Figure 26: LiDAR image of cutoff conglomerate, proximal to transect 10. Average bed thickness observed within the analyzed interval was 1.2 meters, with a fracture density of 0.821 per meter squared……..……56

Figure 27: Illustration of extracted fracture information from the north wall exposure of the Cutoff conglomerate. Stereonet view includes all fracture poles, with great circles representing fracture sets (Holcombe, 2019)…….……57

Figure 28: True color point cloud view of Cutoff channel within Split-FX……..…...58

Figure 29: Illustration of strike frequency, rose diagram of data frequency, stereonet representation of fracture great circles, and area observed, total fractures identified, and fracture density per square meter (Holcombe, 2019)……...59

Figure 30: LiDAR reflectance displayed in Riscan Pro. Color change observed in image indicates a variation in point reflectance, indicative of a mineralogy variation (Giddens, 2016)……..61

Figure 31: Strike frequency, stereonet view showing set great circles with fracture poles, rose diagram displaying data frequency, with area (m^2), total fractures, and fracture density also displayed above unconformity (Holcombe, 2019)……..……62

Figure 32: Strike frequency, stereonet view showing trace fracture poles and total fracture great circles, rose diagram displaying data frequency, with area (m^2), total fractures, and fracture density also displayed below unconformity (Holcombe, 2019)……...…...63

Figure 33: Strike frequency, stereonet view showing set great circles (black and red) with large through fracture poles (blue) and total fracture poles, rose diagram displaying data frequency, with area (m^2), total fractures, and fracture density also displayed for total section (Holcombe, 2019)……...…..64

Figure 34: Transect 7 true color scan within Split-FX. Red filled dots show XRD and Schmidt Hammer measuring positions. Magenta planes indicate fracture traces…….....65

Figure 35: Strike frequency, stereonet view showing total fracture poles and trace fracture great circles, rose diagram displaying data frequency, with area (m^2), total fractures, and fracture density also displayed within the top of Transect 7 (Holcombe, 2019)……..……66

Figure 36: True color point cloud image from Split-FX. Red infilled circles denote XRF/Schmidt Hammer measurement positions 1-7. Unconformity identified above measurement position 2……...68

Figure 37: Illustration of fracture data, displaying strike frequency, stereonet view (blue showing main fracture set, red secondary set, black trace fractures), rose diagram of data frequency, area (m^2), total fractures, and fracture density (Holcombe, 2019)…….....69

Figure 38: True color point cloud image of transect 6, within the Bone Spring Carbonate B…….....70

Figure 39: Illustration of fracture data, displaying strike frequency, stereonet view with fracture set great circles, rose diagram of data frequency, area (m^2), total fractures, and fracture density within Bone Spring Carbonate B (Holcombe, 2019)……..71

Figure 40: Dendrogram representing cluster analysis results from elemental abundances and R values from transect 1. Partitions are labeled adjacent to dendrogram……..74

Figure 41: X-Y plots showing Si/Al, Ca/Al, Ti, Zr, Cu, and Q, with black line indicating zone of elevated Ca/Al, with decreased Ti and Zr, indicating possible increase of relative sea level……75

Figure 42: Dendrogram representing cluster analysis results from elemental abundances and R values from transect 6. Partitions are labeled adjacent to dendrogram……..76

Figure 43: Dendrogram representing cluster analysis results from elemental abundances and R values from transect 7. Partitions are labeled adjacent to dendrogram……77

Figure 44: LiDAR reflectance displayed with derived mineralogy. Red filled circle indicates scan position. It should be noted that Transect 4 collected from studies done by Alabbad (2017) align with transect 6 of this study. Therefore, transect 4D was is displayed, as opposed to Transect 6 measurements……..……79

Figure 45: LiDAR reflectance displayed with derived mineralogy. Red filled circle indicates scan position. Measurement positions are 3,4,5…….....80

Figure 46: LiDAR reflectance displayed with petrographic slide OU-2161-PMNM Red arrow indicates relative sample collection location……..81

Figure 47: LiDAR reflectance displayed with petrographic slide OU-2132-PMNM, with derived mineralogy. Red arrow indicates relative sample collection location……..……82

Figure 48: Schematic diagram illustrating the relative enrichment of Ni, Cu, Mo, U and V versus total organic carbon (TOC). TE stands for trace elements and OM stands for organic matter (Trillovallard et al., 2006)…….86

Figure 49: 2D scatter-plot view, depicting a substantial correlation between Q and Ni in data points collected from transects 1-10. Q vs Cu show a less substantial correlation It should be noted that data points within the x-y plots consist primarily of data collected from mudstone beds.……87

Figure 50: (A) R values derived from SilverSchmidt hardness test, (B) XRF mineralogy in weight percent, (C) nickel concentration in ppm, (D) copper concentration in ppm……87

Figure 51: (A) R values from SilverSchmidt hardness test, (B) XRF mineralogy, (C) nickel concentration in ppm, (D) copper concentration in weight percent for Transect 7.....88

Figure 52: (left) transects 1-5 with (A) Rebound values and (B) XRF-derived mineralogy. (right) defines high-low strength couplets with identical logs views shown. Green shading shows R < 60, Red shading defines intervals where R >60……90

Figure 53: stratigraphic column identifying relative stratigraphy, (middle) log view plotting fracture density, (right) rebound values derived from Q (Mpa). Measured transects are also identified in their approximate stratigraphic positions, adjacent to the stratigraphic column. Measured section recorded in ft……...93

Figure 54: (A) X-Y plot illustrating a strong negative logarithmic correlation between fracture density and average bed thickness, minus the addition of fracture densities measured below the Bone Spring unconformity. (B) highlights identical correlation, with the addition of fracture densities measured at the Bone Spring unconformity. Note substantial decrease in R^2. (C) fracture density vs. average bed thickness separated by lithology……..……...94

ABSTRACT

The purpose of this study is to constrain geomechanical parameters effecting hydraulic stimulation networks within the upper Bone Spring formation, through the collection and examination of outcrop data. Data utilized in this study was gathered from the Bone Canyon, located within the western escarpment of the Guadalupe Mountains, Texas. LiDAR scans were conducted at 13 stations within the Bone Canyon outcrop, utilizing 110 Schmidt Hammer measurements and 140 XRF recordings in order to form a lithofacies-constrained geomechanical model. LiDAR point cloud data was also utilized to characterize fracture orientations, fracture density, and average bedding thickness within the Bone Spring outcrop. Inferences of geomechanical properties are assigned to 5 facies packages identified within the upper Bone Spring formation. Outcrop descriptions and petrographic analysis were performed with the purpose of forming a heightened interpretation of stratigraphic intervals present within the Bone Canyon outcrop.

The findings of this study suggest that: 1) Primary fracture orientations within the upper Bone Spring include a NW-SE trending primary set, consisting of a hexagonal NE-SW strike secondary set present within an interbedded chert-mudstone package identified in the canyon. Primary fracture orientations alternate into a nodular chert-mudstone package positioned stratigraphically above, with NE-SW orientations dominant. 2) The highest fracture densities are observed within the nodular chert-mudstone package and an interpreted detritally-sourced channel within the Cutoff Formation. Fracture densities also show an inverse logarithmic correlation with bedding thickness 3) Anoxic/Euxinic proxies show substantial positive correlations with Schmidt Hammer-corrected rebound hardness values within the nodular chert-

mudstone package (Carbonate A) and interbedded chert-mudstone package (Carbonate B). Positive correlations were also observed between dolomite/quartz volume and rebound values. 4) Fine-scale high/low strength couplets have been inferred from data observations collected within a biogenic silica identified in the 1st Bone Spring Carbonate.

`

1. INTRODUCTION

1.1 Problem Statement

Within the Delaware Basin, Texas, the Bone Springs Formation is one of the most prolific oil producers in the United States. With a daily oil production of 460,000 Boe/d in 2017 (Droege, 2018), the Bone Spring ranks first among plays within the lower 48, in terms of oil production (Droege, 2018). Though the Permian basin, including the areas of the Delaware and Midland sub-basins, have been studied for almost 140 years, there still remains much to be learned regarding the geomechanical properties of these prolific oil producers within the Delaware Basin. The correlation of geomechanical properties to lithology, depositional environment, stratigraphy, fault orientations, and large-scale facies interpretations are critical parameters for the exploration and evaluation of unconventional reservoirs (Slatt et al., 2011). The purpose of this study is to investigate the geomechanical properties of the upper Bone Spring outcrop to rock cycles which may be related to interpreted lithofacies.

1.2 Background

In order to properly characterize mechanical properties within unconventional reservoirs, an analysis of strain and their relationship within an anisotropic rock mass can provide important information with respect to reservoir performance when hydraulically stimulated. Figure 1 illustrates the relationship between stimulated reservoir volumes and multi-stage horizontal wells. Figure 2 illustrates relationships observed between a tight gas shale matrix and fractures. In order to characterize the ease at which a fracture will propagate through a formation, it is common to utilize brittleness measurements. The most common correlation to brittleness used in the oil and gas industry is that of the correlation between Young's Modulus and Poisson's ratio,

`

derived by Rickman et al (2008). Based on laboratory-conducted ultrasonic testing, Rickman et al provided the following equation:

$$B_r = \frac{50}{7}(E - 28v + 10.2)$$

Where B_r represents brittleness, E refers to young's moduli and *v* refers to velocity. A study conducted by Holt et al. (2011) attempted to show that the earlier experimentation conducted by Rickman et al (2008) are reproducible, showing similar P and S wave velocities by performing ultrasonic testing under similar hydrostatic loading conditions. Holt et al inferred that under similar stress and strain, testing would show the results from Rickman et al (2008) are reproducible. The study indicated a positive correlation between brittleness and confining stress with P and S wave propagation, similar to the results from Rickman et al (2008). Because of positive correlations of P and S waves with density – brittleness of the rock, brittleness of a rock can be used to define the mechanical failure or stress/strain relationships of a rock. Other studies defining brittleness include research conducted by Altindag (2003), which describes brittleness as the measure of a material's relative preference to two competing mechanical responses; that of fractures and deformation in transition from ductile to brittle. Recent studies by Bai (2016) on the Woodford Shale using similar variables with the Holts experiment suggested different results, showing negative correlations between P-S wave velocities and density-brittleness. This experimentation suggests that the ultimate failure of a rock mass, for the purpose of fracability, may not be synonymous with brittleness.

Furthermore, Bai (2016) also suggested that the standard Brittleness Index adopted by the oil and gas industry has been widely used inappropriately to characterize the fracability of a rock mass. Instead Bai (2016) suggests that the standard Young's Modulus versus Poisson's ratio

`

relationship, used as a brittleness indicator, should not be a sole indicator of formation fracability. This is because formation fracability is defined by the ultimate rock failure of a formation characterized by the breakdown pressure of a given mass (Bai, 2016). He concludes that unconfined compressive strength (UCS) is a good indicator of breakdown pressure, however in environments of restricted fracturing this may be difficult to analyze, owing to the limits in size of fracturing and lack of free fracture propagation in the bottom hole, inhibited by an increased pressure response (Bai, 2016). Overall, Bai explains that relating brittleness to fracability may inhibit the ability to correctly characterize geomechanical properties, because a brittle formation may have a higher rock strength at higher confining pressures. For example, brittleness index calculations involving approximate mineral volumes (such as Wang et al., 2007) do not compensate for formation pressures, and is only an estimation of how particular mineralogic compositions will react under ideal conditions. Therefore, it is better to use unconfined compressive strength, or UCS, as well as quantifying fracture toughness in some instances (Bai, 2016) to characterize soft rock. Additional acceptable methods of quantifying fracability and fracture toughness include deriving closure stress gradients from maximum and minimum stress, then cross-plotting this data with a dipole-derived brittleness index. However, this method can also be costly, as it would involve performing dipole sonic log measurements, or laboratory testing of core plugs (Holt, 2011).

Little research has been done to better characterize the Bone Springs Formation for artificial fracturing. Furthermore, very little (if any) research has been done to properly characterize geomechanical properties which will allow optimized characterization of rock strength, even when considering tests of brittleness in vertical dipole sonic logs. Furthermore, very little research has been conducted on outcrop-recorded fracture orientation and intensity within the

`

Bone Spring outcrop. There exists only a recent study performed by Alabbad (2017) that has attempted to characterize faults and fractures within the Bone Spring Formation, though miss-interpreting stratigraphic intervals examined within Bone Canyon. Therefore, this work will supplement that of Alabbad's 2017 study, focusing upon the upper Bone Spring formation within Bone Canyon.

This research is purposed to support the identification of strain and its relative relationships to the upper Bone Spring formations. Although utilizing dipole sonic, as well as other stress-strain testing equipment can be more precise, the implementation of these tools can be costly and time consuming. Using the non-destructive testing methods of the SilverSchmidt Hammer, as well as LiDAR acquired point-cloud imagery, hundreds of data points can be collected from samples in a time effective manner, for little cost. Furthermore, XRF data and LiDAR point cloud information were collected to define geomechanical properties, such as Q and corrected R values from Schmidt Hammer measurements, to elemental proxies and lithologies. Stratigraphic lithofacies are further heightened by 17 interpreted petrographic thin sections. LiDAR point cloud data sets are significant as they allow the fracture identification software to identify fracture density, as well as the average thickness of beds within the Bone Canyon outcrop.

`

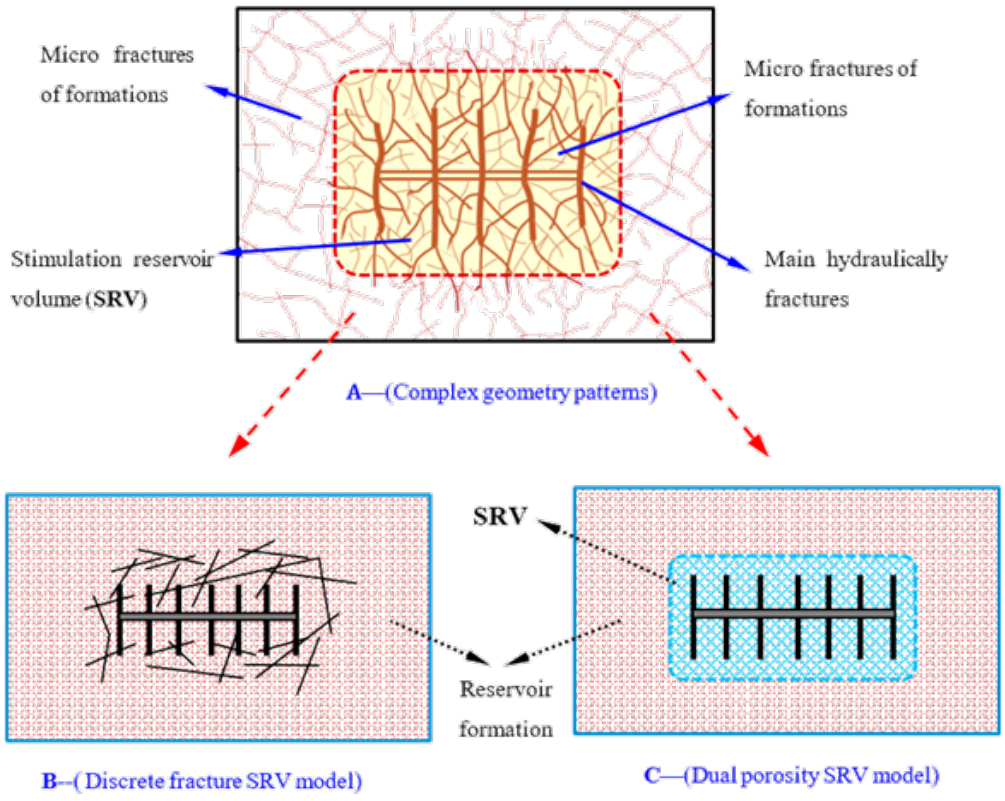

Figure 1: Illustration of a stimulated reservoir volume (SRV), with dual porosity and discrete fracture models shown. Complex fracture geometry patterns are also illustrated (Zhang et al., 2018)

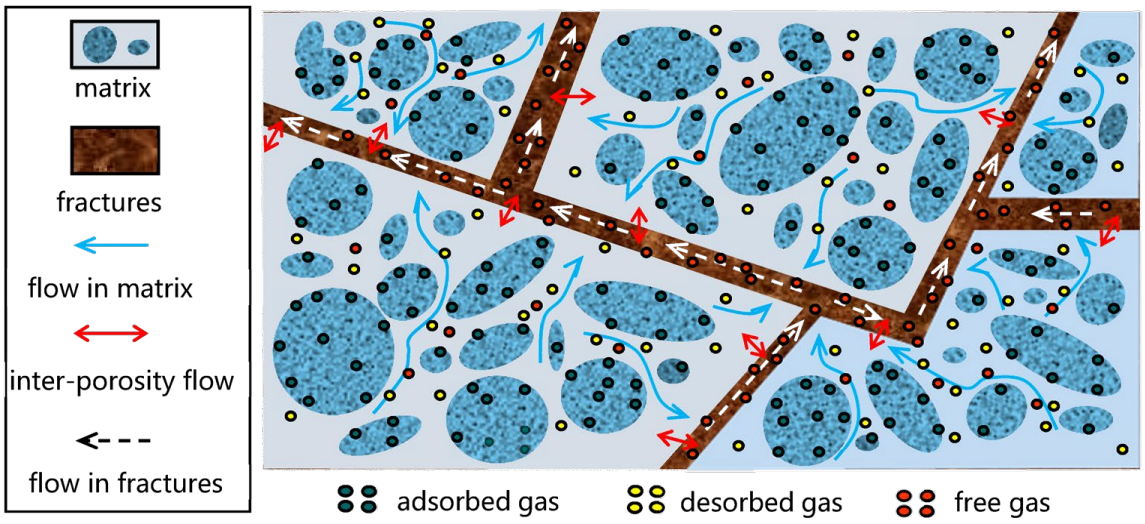

Figure 2: Fracture communication with shale matrix and associated shale gas (Zhang et al., 2018)

`

1.3 Previous Work

P.B King initially described the challenges in differentiating and mapping lithologic sub-units within the Permian Basin in his 1942 publication, which manifested into King's famous characterization of the expansive West Texas Permian-aged strata in his 1948 publication. One of the early flaws in attempting to subdivide the West Texas Permian-aged rocks at the time were the presence of non-uniform lithology within rock units, both laterally and vertically. King chronologically defined lithologic units within the Permian Basin, by constraining collected data with known fossils, unconformities, and time/deposition of various sediments. Figure 3 shows the upper Permian stratigraphy of the Delaware Basin. The Bone Spring type section focused upon in this study is located in the Bone Canyon, present on the western escarpment of the Guadalupe Mountains (King, 1948). In King's 1948 study, the Bone Spring outcrop in Bone Canyon has been described, along with the Cutoff formation, Victoria Peak Limestone, as well as the shelf-margin equivalent to the Bone Spring Formation (King, 1948). According to Crosby (2015), The Bone Spring Formation also crops out approximately 670m North-Northwest in Shummard Canyon, named after the famous G.G Shummard. This classic 1948 study by King has laid out the ground work for many other studies in the Delaware Basin since.

In 1951, John Emery Adams was one of the first to demonstrate that the Delaware Basin experienced a large period of starved basin deposition. He argued that the waning of the Panthalassa Ocean due to decreased relative sea level resulted in an environment restricted of regulatory ocean circulation. This research pioneered the evolution of sequence stratigraphy and lithologic interpretations in the area. In 1965, Adams had proposed a tectonic-stratigraphic development for the Permian Basin and concluded that shelf deposits in the area of west Texas and New Mexico formed as a result of the Tobosa Sag, a largely negative structure effecting

`

deposition through the Ordivician and Permian (Adams, 1965). He suggested that subsurface structure in the area present today was largely attributed to the presence of the Tobosa Sag.

Other important work pertaining to this study include Keller et al., (1983), Hills, (1984), and Ross and Ross, (1994). As well as research done by Kullman (1999). Kullman (1999) discussed the deep-sea fan deposits of the Brushy Canyon Formation as it relates to fault and fractures. Kullman describes the two sets of major faulting within the northern portion of the Delaware Mountains, and that faults with associated fractures acts as conduits for fluid flow. Kullman illustrated that the primary control on fracture density is stratigraphic thickness, whereas lithology seemed to have little control. Finally, he described the permeability of Delaware Mountain fault zones as being most dependent on the definition of strain features, with fault zone alteration (calcification, decalcification, iron-oxide precipitation) being a limited factor to permeability of fault zones within the Delaware Mountains (Kullman, 1999). These concepts are important when interpreting fracture mechanics from Schmidt Hammer data, then comparing small scale interpretations to basin wide fault activity.

Other work studying the Delaware Basin area utilizing LiDAR scanning, XRF data, other various interpretations, such as superposition, interpretation of depositional environments, and utilization Schmidt Hammer measurements include Crosby (2015), Hornbuckle (2017), Wang (2018), Moreland (2018). Some works on the Bone Springs Formation involving SilverSchmidt Hammer data analysis to investigate geomechanical properties include Katz et al., (2000), Yilmaz et al., (2002), Celik et al., (2008), Deghan et al., (2010.). The studies of Katz et al (2000) produced an elaboration of the ability to evaluate mechanical rock properties through Schmidt Hammer data. Their study derived a sequence of linear regressional equations in order to predict mechanical rock properties of various sample types. These rock properties, resulting from testing

`

54mm diameter core plugs (Katz et al., 2000), include Young's Modulus, Uniaxial compressive Strength, and Density. However, Katz et al's also concluded that the hammer rebound values can also be correlative with several additional parameters. Furthermore, it is important to note that core plug testing conditions required a well cemented, perfectly flat testing surface.

Other studies such as Celik (2008) have utilized a form of frame strength analysis of mechanical properties known as point load index. Point Load Test (PLT) is an acceptable rock mechanics test program used to calculate rock strength index. This indicator can also be used to estimate other rock strength parameters. Rock strengths determined by PLT represent complete rock strengths, such as their estimated load frame strengths, not necessarily the actual strength of the rock. Therefore, owing to its facility in collection and utility to correlate to wireline logs, rebound values were utilized primarily in this study, as well as correlations to UCS.

Another study relavent to this research is that of Amani and Shahbazi (2013). In their study, Amani and Shahbazi describe a method to derive Unconfined Compressive Strength (UCS) measured from sonic logs and formation porosity within a carbonate reservoir. This method is important because it allows for the correlation of subsurface UCS derived from wireline logging tools within the Bone Spring Formation. A recent study by Rajabi et al (2017) which attempted to correlate UCS to Schmidt Hammer tests and Point Load Values is also relevant to this study. However, many other studies applying to correlations with other relevant rock types and different equations associated with these studies introduced through time are listed in table 1.

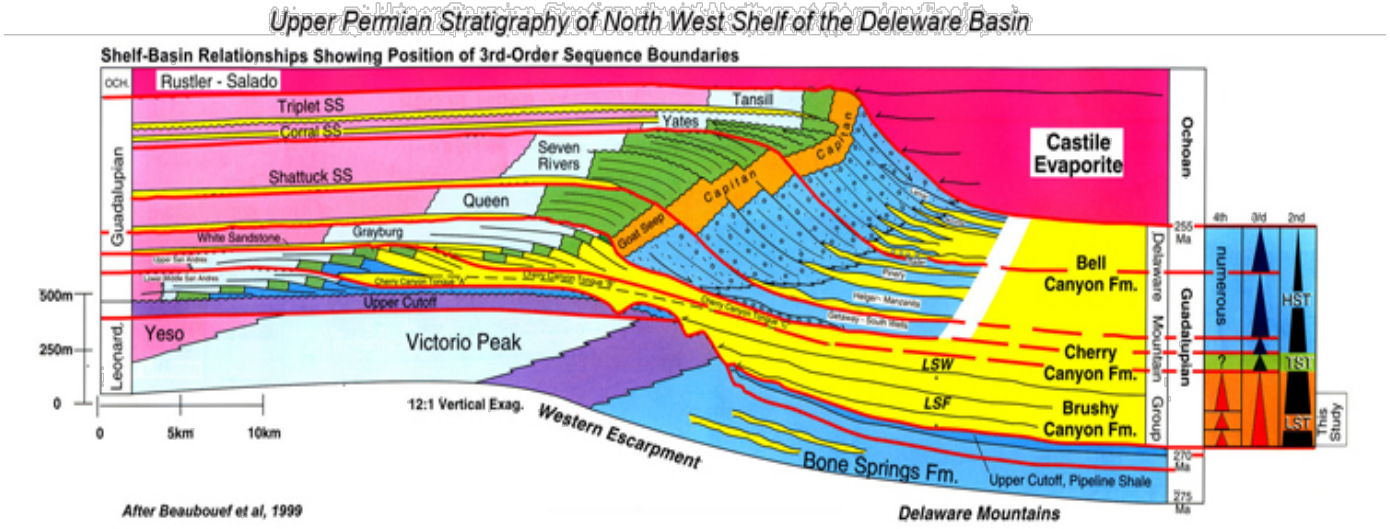

Figure 3. Idealized cross section of the Delaware Basin, from NW to SE. Red box indicates relative stratigraphic position of study area (from Scholle site, 2002)

`

Table 1. Empirical equations through multiple studies, attempting to derive Unconfined Compressive Strength from Schmidt Hammer Hardness. Modified from Rajabi et al (2017)

*** indicates equation used in this paper**

Equation	R^2	Author	Rock Type
$UCS= 9.97e^{(0.02*p*R)}$	$R^2=0.94$	Deer and Miller (1966)	Various Lithologies
UCS=0.4R-3.6	$R^2=0.94$	Shorey et al. (1984)	Coal
UCS=4.92R-67.52	$R^2=0.93$	Sachpazis (1990)	Carbonate rocks
$*UCS=2.21e^{(0.07*R)}$	$R^2=0.94$	Katz et al. (2000)	Limestone and Sandstone
$UCS=e^{0.059R+0.818}$	$R^2=0.98$	Yilmiz and Sendir (2002)	Gypsum
UCS=2.75R-36.83	$R^2=0.97$	Dincer et al. (2004)	Basalts and Tuff
$UCS=0.000004R^{4.29}$	$R^2=0.89$	Yaser and Erdogan (2004)	Carbonates, Limestone
$UCS=1.45e^{(0.07R)}$	$R^2=0.92$	Aydin and Basu (2005)	Granitic Rocks
UCS=3.2R-46.59	$R^2=0.76$	Shalabi et al (2007)	Dolomite, Limestone
$UCS=0.0028R^{2.584}$	$R^2=0.92$	Yagiz (2009)	Travertine, Limestone, Schist
UCS=1.233R-2.846	$R^2=0.91$	Tondon and Gupta (2015)	Dolomite

1.4 Study Area

The Delaware Basin, a sub-basin of the Permian Basin and greater Tobosa Basin, is an asymmetric basin spanning 33,500 kilometers of present-day west Texas and New Mexico (Hill, 1996). The main hydrocarbon producing interval consists of roughly 7620 meters of Paleozoic sediments (Payne, 1976). It is bounded to the north by the Northwestern Platform, to the west by the Diablo Platform, and to the south by the Marathon-Ouachita Fold Belt, being separated from the Midland Basin by the Central Basin Platform, illustrated in Figure 4. This research is conducted on the Bone Spring outcrop, located within the Bone Canyon and positioned on the

`

western Escarpment of the Guadalupe Mountains. Also outcropping within/proximal to Bone Canyon are the Cutoff Formation, Brushy Canyon Formation, Cherry Canyon, and El Capitan reef complex, illustrated in figure 2.

The study area of this research is shown in Figure 4, with basin geometry and Bone Canyon geometry also being illustrated. Measurement transects within the study area are highlighted in Figure 5. Marker 317 indicates the approximate starting position of XRF and Schmidt Hammer sampling. It is noteworthy to mention that, proximal to the Bone Canyon study area, Bone Spring Formation outcrops can also be found. for example, in Shummard Canyon, positioned adjacent to the Bone Canyon outcrop and also located within the western escarpment of the Guadalupe Mountains, a similar Bone Spring stratigraphic section can be observed.

All research was conducted on property owned and managed by the National Park Service, and therefore permission was required in order to enter the property for data acquisition and sample collection. Schmidt Hammer data collected for this study, as well as XRF data utilized from past research (Andrew Brown, unpublished) was implemented in this research. The Bone Canyon outcrop lies at the end of the road leading to the historic house, known as the William's Ranch House. In order to reach the historic house, vehicle transportation is inevitable to transport research equipment safely and effectively. Vehicles were then parked off of the road away from the property, with research equipment being hiked to the mouth of the Bone Canyon outcrop.

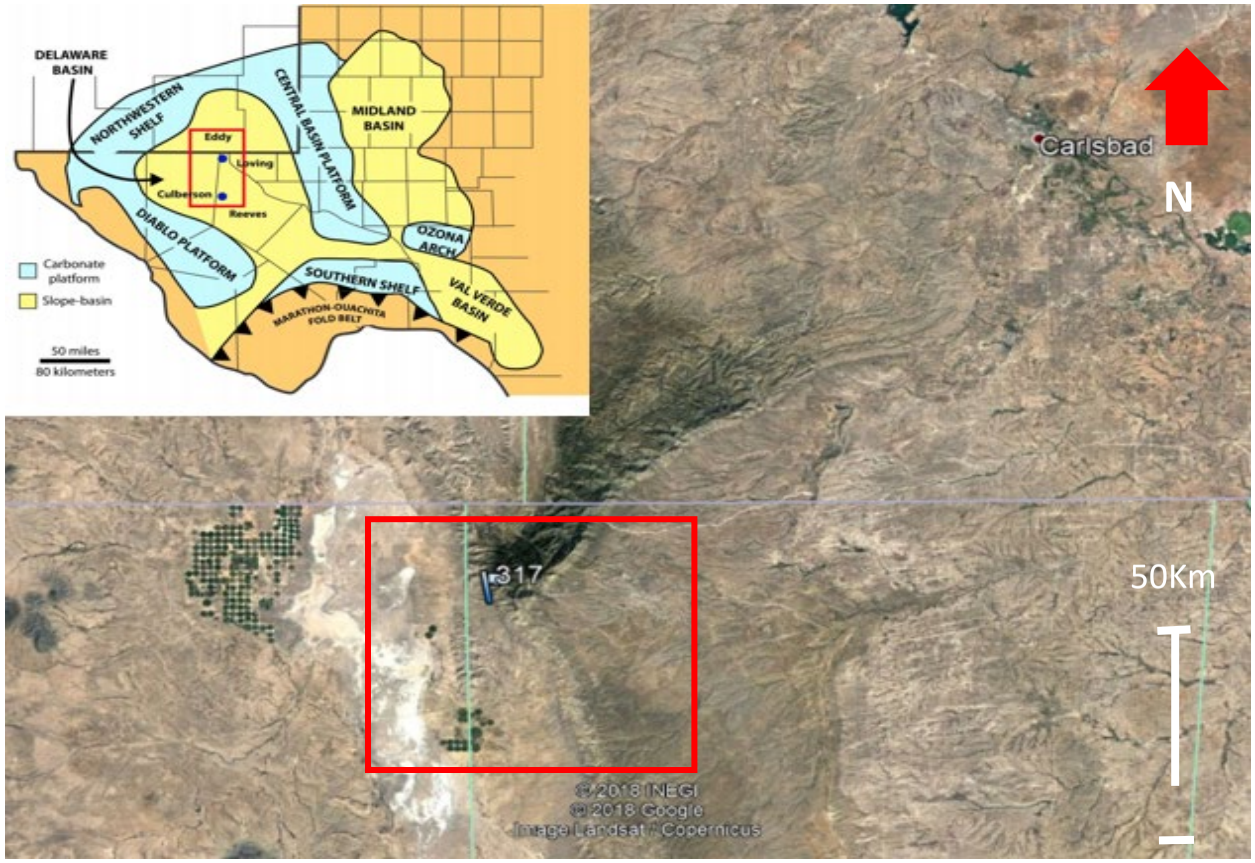

Figure 4. Satellite view of area surrounding Guadalupe Mountains National Park. Upper Left: illustration of the Permian Basin, outlining the Delaware, Midland Basins, as well as the Diablo Platform, Central Basin Platform, Northwestern Shelf, Val Verde Basin, and Southern Shelf. Red box on both the satellite image and upper left image mark the approximate position of the Bone Canyon outcrop. Modified from (Stolz, 2014).

`

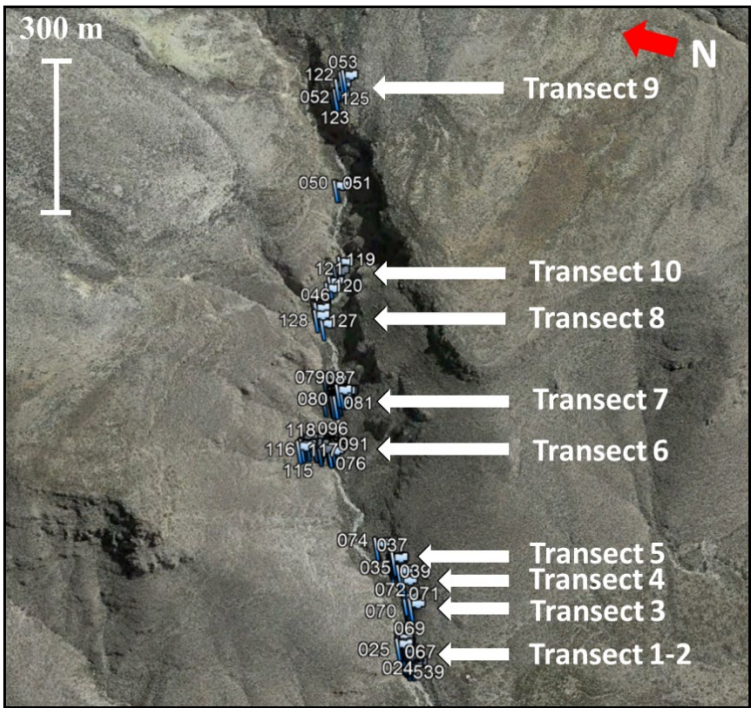

Figure 5: Bone Canyon with relative sample positions highlighted. Waypoint flags illustrated mark GPS positions of sampling locations. Note that samples 050 and 051 were omitted from this study.

Generalized stratigraphic correlation chart for the Permian Basin region

SYSTEM	SERIES/ STAGE	NORTHWEST SHELF	CENTRAL BASIN PLATFORM	MIDLAND BASIN & EASTERN SHELF	DELAWARE BASIN	VAL VERDE BASIN
PERMIAN	OCHOAN	DEWEY LAKE RUSTLER SALADO	DEWEY LAKE RUSTLER SALADO	DEWEY LAKE RUSTLER SALADO	DEWEY LAKE RUSTLER SALADO CASTILE	RUSTLER SALADO
	GUADALUPIAN	TANSILL YATES SEVEN RIVERS QUEEN GRAYBURG SAN ANDRES GLORIETA CLEAR FORK YESO WICHITA	TANSILL YATES SEVEN RIVERS QUEEN GRAYBURG SAN ANDRES GLORIETA CLEAR FORK WICHITA	TANSILL YATES SEVEN RIVERS QUEEN GRAYBURG SAN ANDRES SAN ANGELO LEONARD SPRABERRY, DEAN	DELAWARE MT GROUP BELL CANYON CHERRY CANYON BRUSHY CANYON	TANSILL YATES SEVEN RIVERS QUEEN GRAYBURG SAN ANDRES
	LEONARDIAN	ABO			BONE SPRING	LEONARD
	WOLFCAMPIAN	WOLFCAMP	WOLFCAMP	WOLFCAMP	WOLFCAMP	WOLFCAMP
PENNSYLVANIAN	VIRGILIAN	CISCO	CISCO	CISCO	CISCO	CISCO
	MISSOURIAN	CANYON	CANYON	CANYON	CANYON	CANYON
	DESMOINESIAN	STRAWN	STRAWN	STRAWN	STRAWN	STRAWN
	ATOKAN	ATOKA —BEND—	ATOKA —BEND—	ATOKA —BEND—	ATOKA —BEND—	(ABSENT)
	MORROWAN	MORROW	(ABSENT)	(ABSENT ?)	MORROW	(ABSENT)
MISSISSIPPIAN	CHESTERIAN MERAMECIAN OSAGEAN KINDERHOOKIAN	CHESTER MERAMEC OSAGE KINDERHOOK	CHESTER MERAMEC OSAGE "BARNETT"	CHESTER MERAMEC OSAGE "BARNETT"	CHESTER MERAMEC OSAGE "BARNETT"	MERAMEC OSAGE "BARNETT"
			KINDERHOOK —WOODFORD—	KINDERHOOK —WOODFORD—	KINDERHOOK —WOODFORD—	KINDERHOOK —WOODFORD—
DEVONIAN		—WOODFORD— DEVONIAN	DEVONIAN	DEVONIAN	DEVONIAN	DEVONIAN
SILURIAN		SILURIAN (UNDIFFERENTIATED)	SILURIAN SHALE FUSSELMAN	SILURIAN SHALE FUSSELMAN	MIDDLE SILURIAN FUSSELMAN	MIDDLE SILURIAN FUSSELMAN
ORDOVICIAN	UPPER	MONTOYA	MONTOYA	SYLVAN MONTOYA	SYLVAN MONTOYA	SYLVAN MONTOYA
	MIDDLE	SIMPSON	SIMPSON	SIMPSON	SIMPSON	SIMPSON
	LOWER	ELLENBURGER	ELLENBURGER	ELLENBURGER	ELLENBURGER	ELLENBURGER
CAMBRIAN	UPPER	CAMBRIAN	CAMBRIAN	CAMBRIAN	CAMBRIAN	CAMBRIAN
PRECAMBRIAN						

Source: Yang and Dorobek 1995)

Figure 6: Stratigraphic column of the Permian Basin region. From Yang and Dorobek (1995)

`

2. GEOLOGIC BACKGROUND

2.1 Pennsylvanian - Wolfcampian Deposition

Within the Permian Basin, the Pennsylvanian through Wolfcampian (Permian) strata consist of the Springer, Morrow, Atoka, Strawn, Canyon, Cisco, and Wolfcamp Formations, illustrated in figure 6. The Pennsylvanian was a time of increased tectonic exertion, which brought forth rapid subsidence, and in broad terms, a starved basin experiencing deep burial (Adams, 1965). Further uplift and subsidence were induced by the Ouachita-Marathon orogeny which generated the greater ancestral Rocky Mountains. Overall, deposition during the Pennsylvanian within the Delaware Basin was dominated by deep-basin shales, partly due to an exacerbated period of subsidence (Adams, 1965; Hills, 1984; Crosby, 2015). This rapid subsidence and growth of Pennsylvanian sedimentation created significant accommodation space for the subsequent deposition of Permian sediments. Furthermore, past research also suggests that carbonate deposition occured along the northwest shelf within the Cisco Group, with sporadic appearances on well logs near the base of the Wolfcamp/Pennsylvanian unconformity (Hills, 1984).

The deposition of carbonates proximal to the Pennslyvannian/Wolfcamp boundary primarily consists of platform carbonates and continued throughout Permian time. Because the Pennsylvanian Morrow and Atoka Formations thicken towards the Central Basin Platform likely as a product of flexure, accommodation space was created at the conclusion of the Ouachita-Marathon Orogeny (Wright, 2008). Though not the primary focus of this paper, increasing tectonic activity within Pennsylvanian time created significant fault-related structures (Kullman, 1999). Pennsylvanian sedimentation thins to the east and is absent as a result of erosion on fault blocks, associated with the uplift of the Central Basin Platform.

`

The dominance of clastic deposition initiating the Wolfcampian sequence is due to continued tectonic uplift, initiating a period of relative sea level change and sustained reciprocal sedimentation. This reciprocal sedimentation was primarily being sourced from the west, southwest, and northwest parts of the Delaware Basin (Adams, 1965). Clastic sedimentation during the Wolfcampian were predominated by the deposition of turbidity sediments sourced from the west. Agitation of the water column from turbidity deposits caused mixing of the water column, allowing for the enhancement of nutrient-rich water which increased the production of hydrocarbon source materials. As a further result, an increase of algae, and planktonic/nektonic organisms occurred within the paleo-water column (Adams, 1965; Hills, 1984). Throughout the Wolfcampian, waning of siliciclastic deposition allowed for the development of carbonate deposition along the shelf of the Delaware Basin. The creation of carbonate build-ups was further supported by a continuing decrease in clastic deposition towards the end of the Wolfcampian (Hills, 1984; Crosby, 2015). Seen as the first instance of extensive shelf carbonate build-ups within the Delaware, the build-up seen within the center of the basin consists of interbedded shale deposits with skeletal hash-rich mounds (Silver and Todd, 1969).

`

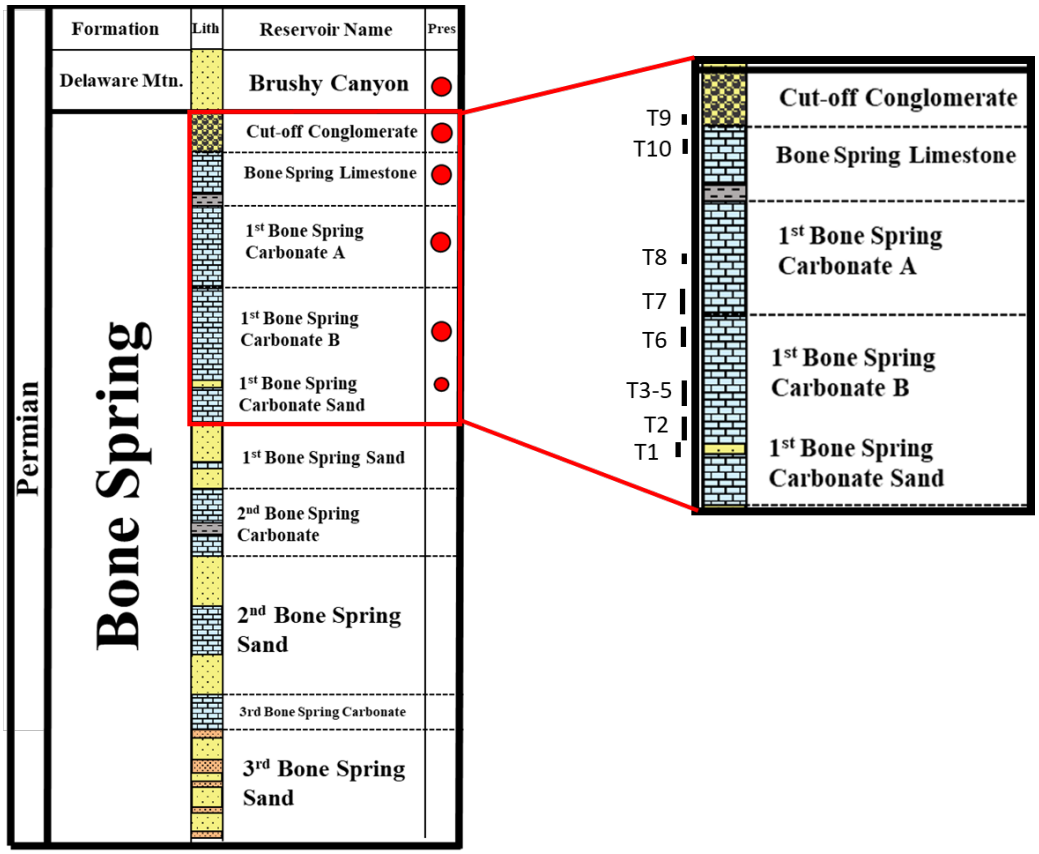

Figure 7. Idealized stratigraphic column illustrating early through late Permian sedimentation within the Bone Canyon outcrop. Red circles mark sections observed in the study area, with transects marked to the right. Modified from Alabbad, 2017.

2.2 Bone Springs Deposition

The Delaware Basin in the time of the Leonardian experienced multiple fluctuating depositional episodes of highstand carbonates and lowstand clastics, encompassing the Bone Spring Formation. Illustrated in Figure 7, the Bone Spring in the subsurface is generalized to consist of three oil-bearing siliciclastic intervals alternated with three organic-rich carbonate mudstone intervals. The Highstand deposition of the Wolfcamp Formation was followed by a sea level fall during the Leonardian whilst the subsequent lowstand and transgressive deposition of the 3rd Bone Spring Sand occurred (Hart, 1998; Crosby, 2015). The cyclic transition of changing sea level from high to lowstand system's tracts ultimately led to the deposition of highstand

`

carbonates, followed by lowstand siliciclastic deposition in the form of sediment gravity flows transporting carbonate material from the shelf edge (Pray, 1988; Montgomery, 1998; Crosby, 2015). Figure 8 outlines this form of reciprocal sedimentation involving highstand carbonates and lowstand clastic sedimentation.

Research conducted by Montgomery (1998) suggested that deposition during the Leonardian was primarily controlled by tectonic subsidence, even stating that the Leonardian saw similar or more tectonic activity than the Wolfcampian. This suggestion supports previous studies which show that low relief structures formed during high tectonic activity of the Pennsylvanian controlled paleobathemetry and the depositional axis of deposition (Hart, 1998).

The 3rd Bone Spring Sand, overlying the Wolfcamp Formation, marks the top beginning of the Bone Spring. Though debate exists on the stratigraphic marker demarcating the 3rd Bone Spring and the Wolfcamp (Montgomery 1997), a well-known oil play referred to as the Wolfbone play lies just above a limestone bed which marks the separation between the Bone Spring and Wolfcamp. Research done by Mazullo and Reid (1987) suggested that this particular limestone bed can be dated by age-related fusulinid fossils. The 2nd Bone Springs Carbonate, located above the 2nd Bone Springs Sand, is an allochthonous carbonate deposited at a time when sea level highstands were contributed to maximum deposition of carbonates on the Northwest Shelf (Davis, 2014). Carbonates within this zone primarily consist of spiculitic, carbonaceous wackestones, with lime mudstones common in the basin. Laminated dolomitic mudstones and dolomitized megabreccias are also common on the slope (Gawloski 1987; Davis, 2014). The main mechanism for deposition involves turbidity and debris flows containing shelf derived carbonate material. Therefore, the lithology of the 2nd Carbonate is entirely dependent on that of the shelf-equivalent Abo-Yeso carbonate formation. Furthermore, dolomitization of clasts within

`

the 2nd Carbonate underwent early dolomitizing prior to deposition (Davis, 2014). The 2nd Bone Spring Formation is also one of the most active horizontal drilling targets within southeast New Mexico oil plays within the Delaware Basin, with an average initial production rate of 1,300 BOE/d (Crosby, 2015).

Overlying the 2nd Bone Spring Carbonate are the 1st Bone Spring Sand and Carbonate being similar in ways to the 3rd Bone Spring Carbonate, mainly composed of spiculitic mudstones and wackstones: Carbonate deposition occurred during high-stand deposition in a time when shelfal carbonates were experiencing high production, as shown in Figure 8 within the Bone Canyon outcrop. Carbonate siltstones can also be observed within the 1st Bone Spring Carbonate interval. Delineation between bedded chert and carbonate mudstone and nodular chert, interbedded with carbonate mudstone was observed between the lower and upper sections of the canyon. This is thought to be due to fluctuations in biogenic silica precipitation within the upper Carbonate of the Bone Spring formation within Bone Canyon. Though categorized as an independent lithologic subsection, the six packages comprising the Bone Spring can be defined under a reciprocal depositional model. The primary formations within the Bone Spring as defined by Hart's 1998 study consist of (in chronologic order) 3rd Bone Spring Sand, 3rd Bone Spring Carbonate, 2nd Bone Spring Sand, 2nd Bone Spring Carbonate, 1st Bone Spring Sand, 1st Bone Spring Carbonate (Hart, 1998). Figure 9 illustrates the relationship of depositional environmental models alternated between the sub-units of the Bone Spring, during the changing of sea level.

Above the 1st Bone Springs Sand lies the clay rich Avalon Shale (Davis, 2014), which has been a popular completion target for horizontal drilling and hydraulic fracturing by public operators in the region (droege, 2018). Overlying the clay rich Avalon Shale is the Avalon Carbonate, defined by dark carbonate shaly siltstone interbedded with mudstone. This

`

interbedded siltstone acts as permeable conduit for vertical fluid flow (Bachmann et al., 2013). The Avalon shale interval is theorized (Davis, 2014) to consist of sedimentation stratigraphically above the 1st Bone Spring Carbonate (divided into Carbonate A and Carbonate B in this study). Furthermore, the Avalon shale is obviously being identified within subsurface logging data. However, confirmation of the Avalon shale within Bone Canyon has not been confirmed in this study, owing to a lack of comparable outcrop information in the area. Therefore, the upper section of the 1st Bone Spring Carbonate has been characterized based on transitions in identifiable lithofacies, illustrated in figure 7. The Upper Bone Spring Limestone is dominated by massive, blocky mudstones towards the Bone Spring/Cuttoff boundary. Within the Bone Canyon outcrop, past research studies have hypothesized that the Bone Spring Formation, Cutoff and Brushy Canyon Formations are the main intervals exposed within Bone Canyon (Beaubouf et al., 1999) though this study focuses primarily on the Brushy Canyon formation. As shown in Figure 7, the outcrop units identified in this research consists of the 1st Bone Spring Carbonate Sand interval, 1st Bone Spring Carbonate B layered chert dominated (potential lower Avalon Shale interval), 1st Bone Spring Carbonate A nodular chert dominated (potential upper Avalon Shale interval), the Bone Spring Limestone, Cutoff Conglomerate, and the Brushy Canyon formation. Intervals positioned stratigraphically above the Brushy Canyon formation, including the Bell Canyon formation and Cherry Canyon formation, were observed in the field and inferred, however not confirmed in this study.

Figure 8: Bone Canyon outcrop, Bone Spring formation, 1st Carbonate B. Taken at Transect measurement 2. Note the presence of bedded chert, common in the lower part of the canyon.

`

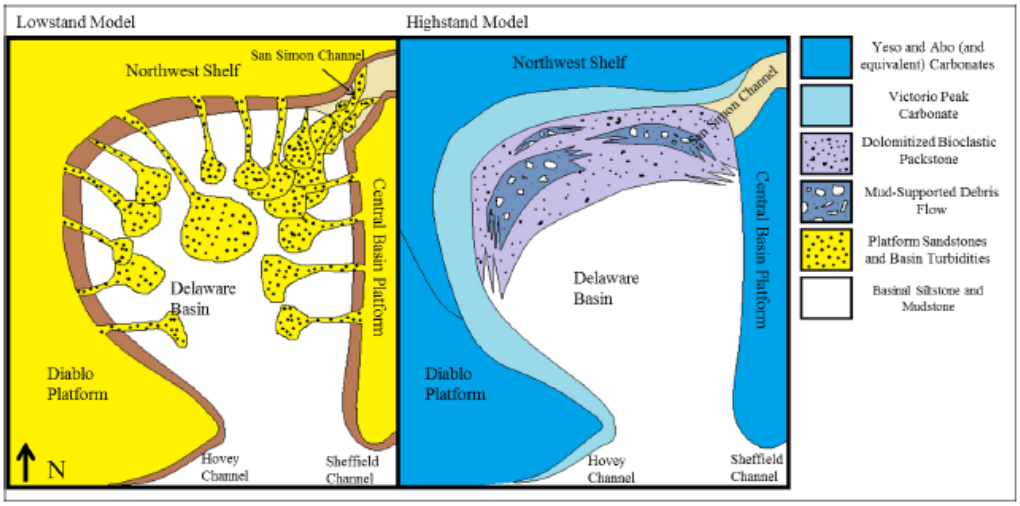

Figure 9: Illustration of simplified reciprocal sedimentation within the Delaware Basin, during high stand carbonate deposition with mud supported debris flows, and Low stand siliciclastic deposition dominated by platform sandstones and turbidites. Adapted from Scholle, 2002 through www.sepmstrata.org

2.3 Guadalupian – Ochoan Deposition

The Brushy Canyon formation belongs to the Delaware Mountain Group, initiating the lower Guadalupian and middle Permian (King, 1948). Associated with global sea-level fall in the Panthalassa Ocean, further fluctuations of relative sea-level within the Delaware Basin produced low stand deposition of detrital within the region. Recent studies published by Higgs (2015) have suggested that interpretations of the Brushy Canyon Formation as a product of shallow water deposition, which most operators within the Delaware Basin have adopted, would be better instead modeled as a deep-sea turbidite fan model. Higgs goes on to suggest that the Brushy Canyon is an analogue for deep sea turbidite deposits, analogous to “Flysch” deposits, that is orogenically external in nature. The appropriate terminology (dubbed by Higgs, 2015) is a miogeosynclinal Flysch. The Brushy Canyon formation is also dominated by storm-wave-base

`

dominated hyperpycnites, exhibiting fine grain deposition with hummocky cross-stratification prevalent. Also, present within the inner-most Brushy Canyon are mega breccia originating from limestone-block conglomeritic debrites (Higgs, 2015). Other deposits within the Brushy include incised slope channels, prograding deltaic complexes and as previously mentioned, hyperpycnites (Higgs 2014; Higgs 2015). Figure 10 displays the Brushy Canyon outcrop within Bone Canyon.

The final lowering of sea level within the Panthalassa Ocean during the Ochoan caused the Delaware Basin isolated from connected oceanic circulation, causing the deposition of the world-renowned Castille Evaporites. Other evaporites consist of the Salado and Rustler Formations, which lie within the northern and eastern margins of the basin (Adams, 1965). Following evaporite deposition is terrestrial red beds prograding into the basin (Adams, 1965). Late Permian deposition (Late Ochoan) consists of an extended hiatus and subaerial erosion through the early Mesozoic (Hills, 1984)

`

Figure 10: Outcrop of Brushy Canyon formation within Bone Canyon. This section was subject to studies conducted by Alabbad (2017) in which fracture orientations were interpreted and recorded.

2.4 Tectonic History

In order to thoroughly understand geomechanical properties inferred from field-collected data in this study, it is important to report the previous tectonic history of the region. The location encompassing the westward Delaware Basin has been subject to multiple orogenic events within the last one billion years. Orogenic events relevant to the overall tectonic development of West Texas, the Trans-Pecos Texas region and the Permian Basin include three principal events: early Precambrian orogenic events, late Paleozoic compression following the formation of the Pangean supercontinent, compression from the Laramide Orogeny during the late Cretaceous, concluding with Cenozoic extension relating to the formation of the Basin and Range Province (Kullman, 1999). Figure 11 shows a schematic representation of regional

`

extension and fault propagation within the Permian Basin – Basin and Range Provence. The early Ordovician witnessed cooling of underlying rifted crust, creating subsidence and the creation of coastal plains known as the Tobosa Basin (Galley, 1958; Yalmaz, 2015; Wang, 2018).

Precambrian tectonic events within the area between the Trans-Pecos Texas region and westward from New Mexico to Arizona once was associated with the southwestern margin of the ancient North American Plate (Muelberger and Dickinson, 1989), and are thought to have formed as part of large branching rift system due to southeasterly extension around 1450 ma (Kullman, 1999). Precambrian tectonic activity is ultimately the main catalyst for the observed regional structural grain, including the location and orientation of structure produced in later orogenies. Terranes in chronologic order include the Chaves Granitic Terrane, overlain by the Precambrian siliciclastic rocks of the Debaca Terrane (Denison et al., 1971; Kullman, 1999), followed by the Franklin Mountains igneous terrane above. This succession is then followed by the Van Horn metamorphic mobile belt, thrusted onto the Debacca. Furthermore, K-Ar age dating of the Llano/Chaves unconformity suggests that is could represent a southward extension of the Grenville Front (Denison et al., 1969; Kullman, 1999).

Early Paleozoic-Late Cretaceous: Associated with the larger Tobasa basin, the late Precambrian to late Mississippian section is characterized by the presence of faint crustal extension with a low rate of tectonic subsidence in a passive margin setting (Kullman, 1999). The Permian is considered to be Tectonically stable. Vertical movement between fault bounded zones can be attributed to the accretion of the Pangean supercontinent within the late Mississippian. According to earlier work done by Muehlberger and Dickerson (1989) and Kullman (1999), weakness seen along vertical movement in zones can be attributed to hyper-

`

tectonic activity within the late Precambrian. This fault block movement subsequently caused the creation of Horsts (Diablo Platform and Central Basin Platform) and Grabens (Delaware Basin and Midland Basins). The Permian is thought to consist of relatively stable basin subsidence and tectonic activity (Hills, 1984; Kullman, 1999). Figure 12 illustrates the sub-basins of the Delaware and Midland Basins as the relate to the overall Tobosa Basin.

The Laramide Orogeny is thought to had little to no influence upon the Delaware Basin, other than slight uplift of the Delaware Mountains. The result of Laramide compression consists of limited broad arching (Kullman, 1999).

Cenozoic Deformation: The formation of the Salt Flat Graben and Delaware Mountains resulted from Trans-Pecos tectonism in the Cenozoic (Kullman, 1999). Laramide compression transitioned into Basin and Range extension, preceded by a brief volcanism event within the Eocene-Oligocene. The end of the Paleocene saw a period of extension preceding rifting and graben creation.

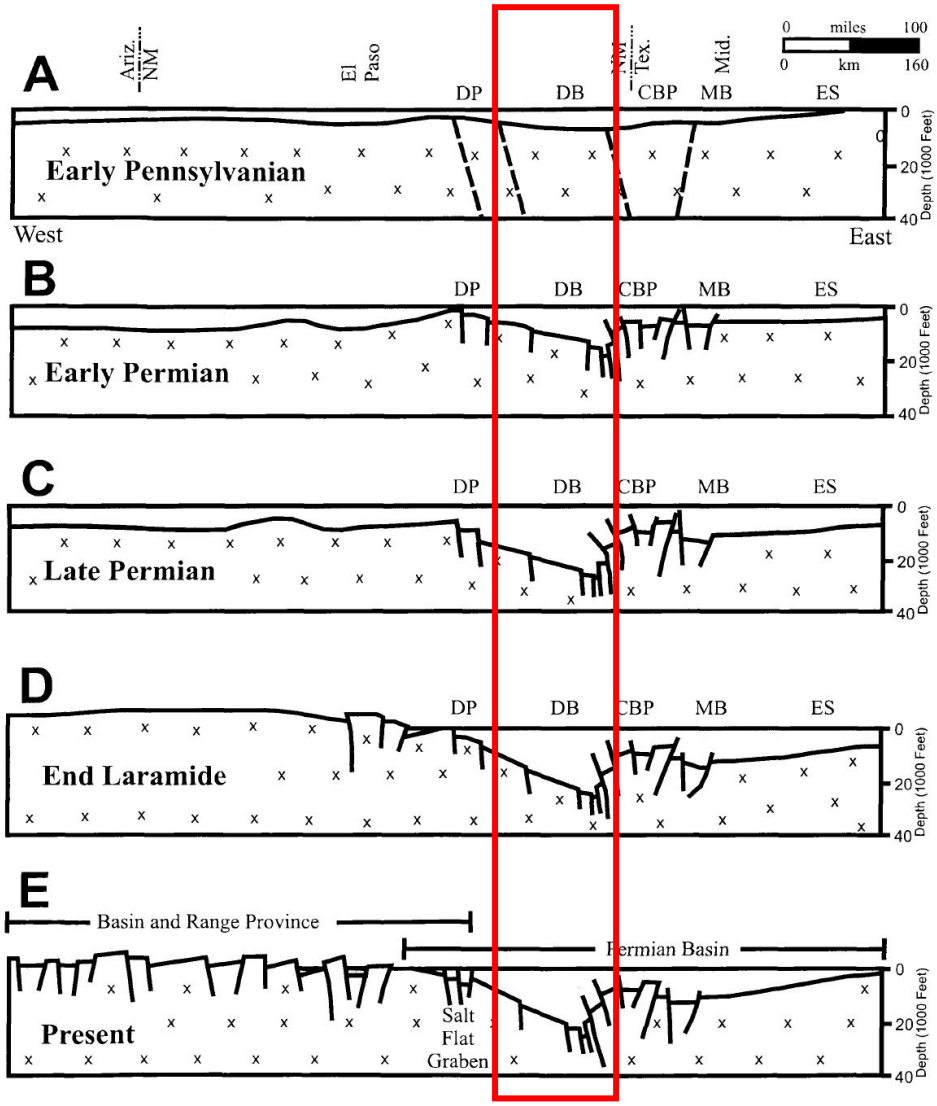

Figure 11: Transgression of tectonic events from the early Pennsylvanian to present. Modified from Kullman, 1999

`

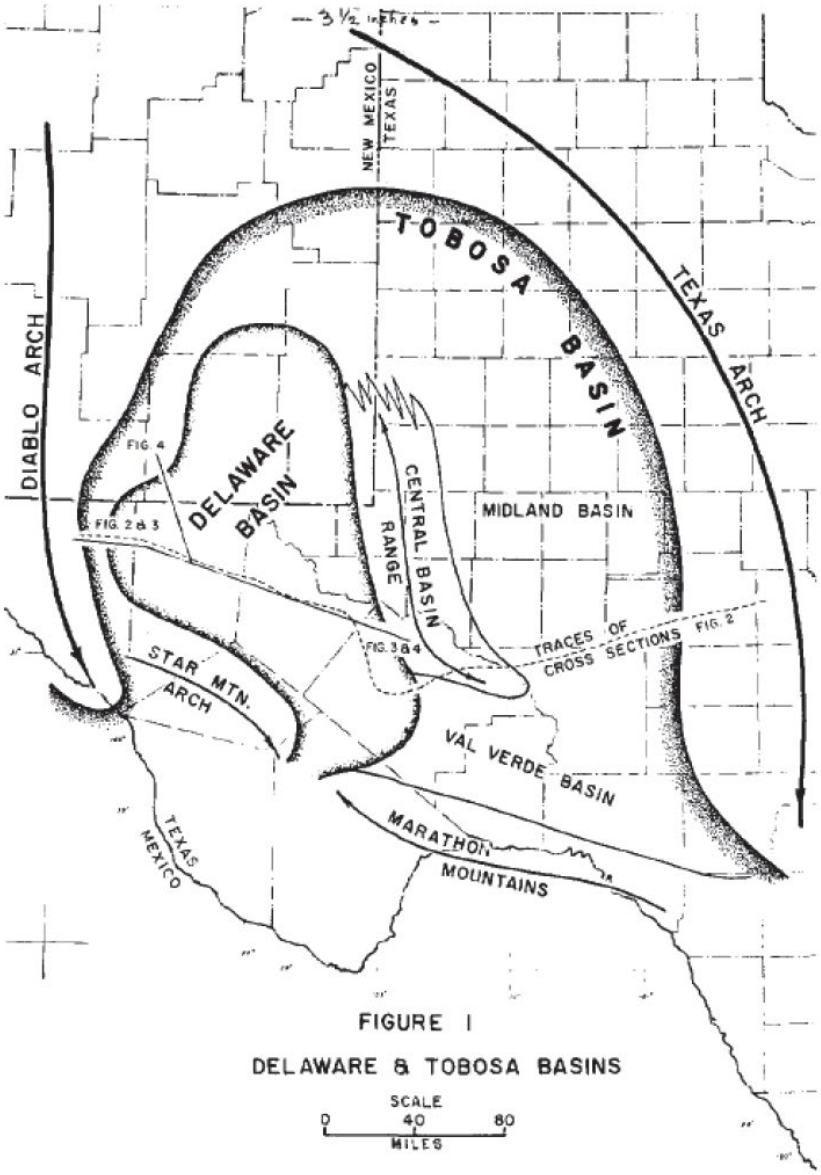

Figure 12: Outline of Delaware Basin, with relation to Tobosa Basin, Texas Arch and Diablo Arch. from Adams (1965).

`

2.5 Fault History

Regional fault characteristics, as defined in the previous section, are partially controlled by the early tectonic development of the Tobosa Basin during the Precambrian. Fault trends within the region are primarily northwest/southeast (King, 1948). As will be defined, these findings correspond to those found in this study, with secondary fracture orientations from East/West. Fault development within the Early-late Permian were developed through weakness seen in vertical fault sections due to increased tectonic activity in the Precambrian, further experiencing minimal uplift within the Laramide Orogeny (Hills, 1984). Figure 13 shows known major fault populations through west Texas and the Delaware Basin. Relative position of the study area examined in this paper is highlighted in red. The main fault within the Bone Canyon outcrop and Williams Ranch region is defined by a large degree of vertical separation, displacing formations above the Cherry Canyon formation by over 5000 feet (Hills, 1984). Smaller fault complexes can be identified in the lower sections of Bone Canyon encompassing the Leonard sand package. Further fault growth within the Cenozoic to present day is largely a consequence of Basin and Range expansion within West Texas and New Mexico along the Trans-Pecos region (Hills, 1984; Kullman, 1999).

Though the Delaware Basin shows signs of modern tectonic activity, the development of faults and fractures in relation to hydrocarbon development during this time is extraneous. Work done by Dumas (1980) and Goetz (1980) show evidence of seismic activity and modern tectonic readjustment of the Diablo Plateau (shown in figure 11) by roughly 23 cm between 1934 and 1977 (Kullman, 1999).

`

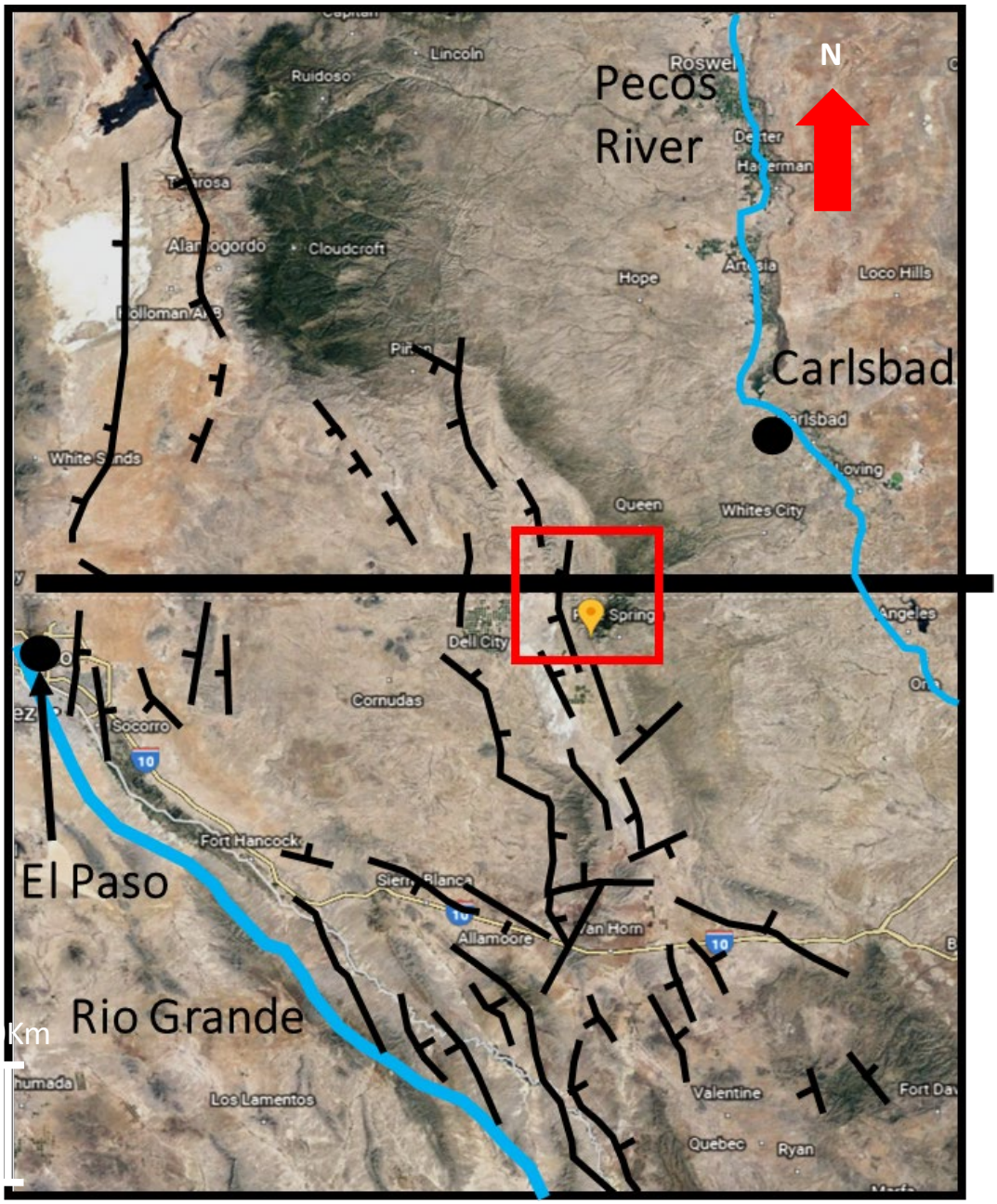

Figure 13: Cenozoic fault map of west Texas and Southeastern New Mexico. Red Square marks relative position of study area. Orange Pin marks GPS position of Bone Canyon. After Kullman, 1999.

`

3. METHODS

3.1 Field Methods

Collection of LiDAR, Schmidt Hammer and XRF data was conducted within the Bone Canyon outcrop, positioned in the Guadalupe Mountains National Park. These outcrops are believed to represent the 1st Carbonate of the upper Bone Spring, a conglomeritic unit of the Cutoff Formation, and the Brushy Canyon Sandstone (seen in Figure 7), though no data was collected from the Brushy Canyon in this study. Intervals within Bone Canyon consisting of the Brushy Canyon were analyzed by Alabbad's 2017 research. Sampling intervals vary between transects which four samples were collected between the bedded chert and limestone, detailed transects with sampling intervals of roughly 15 feet, and transect 1, which includes a 1-foot sampling interval. Figure 7 illustrates measured transects and their relative position to lithofacies. Variations in sampling intervals are to identify small scale mechanical variations as well as large scale correlations. The roughly 3000 ft of measured section, most being extremely difficult to reach on foot, is split into 10 different measurement transects, analyzed using Schmidt Hammer Collection, LiDAR, and XRF. Figure 14 outlines the relative locations of individual measurement transects. Transect 1, 6 and 7 are defined by fine scale sampling, which consists of a sampling interval of 1-15 ft. Transects 2,3,8,9, and 10 consist of sampling intervals of 15-50ft intervals. Both transects 6 and 7 consist of Schmidt hammer analysis, Light Detection and Range (LiDAR) scanning, and X-Ray Fluorescence (XRF) measurement. Transect 1 consists of XRF and SilverSchmidt analysis. Varying sampling intervals of different transects can also save valuable time in the field and can be used to infer relative information regarding rock strength-lithologic composition. Transect 1 was measured along a lithologic transition from sandy mudstone to carbonate-rich mudstone, which is interpreted to be a transition from biogenic silica

`

precipitation into Bone Spring Carbonate deposition. Transect 9 was gathered toward a suspected channel of detrital sediment deposition within the Brushy Canyon/Cutoff formation boundary, likely from sediment gravity flows easily observed in the Shummard Canyon outcrop.

3.2 Light Detection and Range Device Collection and Mechanics

Acquisition of LiDAR readings required the traversing of hazardous terrain through Bone Canyon, in order to collect data on the entirety of the Bone canyon outcrop (roughly 450m vertical depth). Conditions appropriated the use of four researchers to carry equipment through the canyon. A RIEGL VZ-400i 3D terrestrial laser scanner with an attached Nikon D810 utilizing a Nikor 20mm lens was used in this study. The LiDAR's effective range of 1000m, at these altitudes and low humidity, allows the observer to image an outcrop from multiple positions, while accuracy of 5mm and precision of 3mm allows for accurate readings and interpretations of measurements (REIGL, 2013; Hornbuckle, 2017). The investigator can then compile multiple scans into a high resolution, three-dimensional model using reflectors as tie points.

The reflector geometry is designated so that shadows caused by canyon walls, trees, boulders, and other objects obstructing the view of the camera are minimized. Reflectors are also necessary to tie scans together in the 3D model. Three common reflectors are required between scans in order to perform a tie of discrete scans. Reflectors consist of 10cm cylinders and 5cm flat reflectors which possess a cohesive material on the backside. The number of reflectors necessary and relative position depend on outcrop geometry and length of desired measurement area. Scanning positions were determined prior to reflector placement in order to optimize each reflectors ability to maximize shadow reduction. Once scanning positions have been set and

`

reflectors have been placed, the LiDAR is carefully attached to a tripod, then connected to a portable laptop directly with an ethernet cable. Each scan is recorded individually to the laptop via ethernet and simultaneously stored on the RiScan Pro v2.5.3. A 360° scan is then conducted with a 0.02° resolution and a Pulse Repetition Rate (PRR) of 300 kHz (REIGL 2013, Hornbuckle, 2017). Total time per scan was set at 15 minutes, with the LiDAR internal GPS Positioning system set to FAST. During the full scan, six individual photographs are taken with the LiDAR identifying overlap. Identification of longitude and latitude position are recorded on top of the LiDAR internally during pose estimation (internal GPS positioning system). Once the LiDAR has concluded a scan, reflectors are repositioned if necessary and another scan is performed. The user also can perform an additional 0.005mm fine scan after the initial scan. Duration varies depending on size of measured section. Once this process is complete, the user must locate corresponding reflector points with the RiScan Pro software.

In total, 13 scans were performed in the span of three days. The initial estimation of 17 scans was undermined by the internal system failure of the LiDAR after scan 13, thus scans at the entrance to the canyon were not conducted. Scan positions utilized in this study are identified in figure 14, with approximate transect locations and formation boundaries also outlined. Visibility was clear, with wind speeds of roughly 20MPH from the Northwest. Camera settings were set to a shutter speed of 1/250 seconds, aperture of f/22, and ISO of 250 for all 13 scans. Though the shadows from the canyon walls were initially thought to become a problem once in the field, the initial images from the Nikon D810 revealed a balanced exposure and true color present, therefore no corrections for shadows were needed.

`

3.3 LiDAR Processing

Once LiDAR data are acquired, scans are processed in RiScan Pro v2.5.3 as point cloud data. Sizes of point clouds can range in size, from thousands to millions of points depending on outcrop size. Point cloud data are defined as "a set of points with coordinate values in a well-defined coordinate system" (RIEGL Glossary, 2012; Hornbuckle, 2017). The LiDAR multi-scan model makes stratigraphic interpretations more comprehensible, with the ability to observe facies changes at the millimeter scale. Figure 15 displays interpreted formation boundaries between the Bone Spring, Cutoff, and Brushy Canyon formations. Figure 13 displays a set of point cloud data shown in true color. Furthermore, each point within the point cloud has data associated specific to each individual point, such as reflectance, amplitude, time stamp, and pulse shape deviation (REIGL, 2013; Giddens, 2016). Once all data are converted to polydata, an octree filter is applied to the point cloud in order to create a uniform data set. This octree application ultimately deletes the polydata created by the user and evenly distributes points. After the octree filter is applied and the image has been cleared of noise, points are then triangulated to create the mesh which the user can use to display reflectance and amplitude.

Reflectance and amplitude of wave signals recorded by the LiDAR can be a helpful mechanism for outcrop interpretation. The amplitude of each point is given as a ratio of the echo signal of the detection threshold of the LiDAR scanner, given in decibels. It should be noted that the amplitude signal given by a point within the mesh should only be considered accurate if the scanning position relative to said point is exactly perpendicular. Reflectance of a point can be defined as the incident of optical power given by a point at a given wavelength. The reflectance measured is a ratio of the amplitude given by a point to the amplitude given by a flat target, with an orthonormal orientation to the beam. Because of this, it is considered independent of target

`

angle (REIGL 2013; Giddens, 2016). This measurement therefore reveals the strength of a light point hitting a point and returning to the reflector. Because of this reliability, reflectance is the major LiDAR attribute applied to the outcrop measured at Bone canyon.

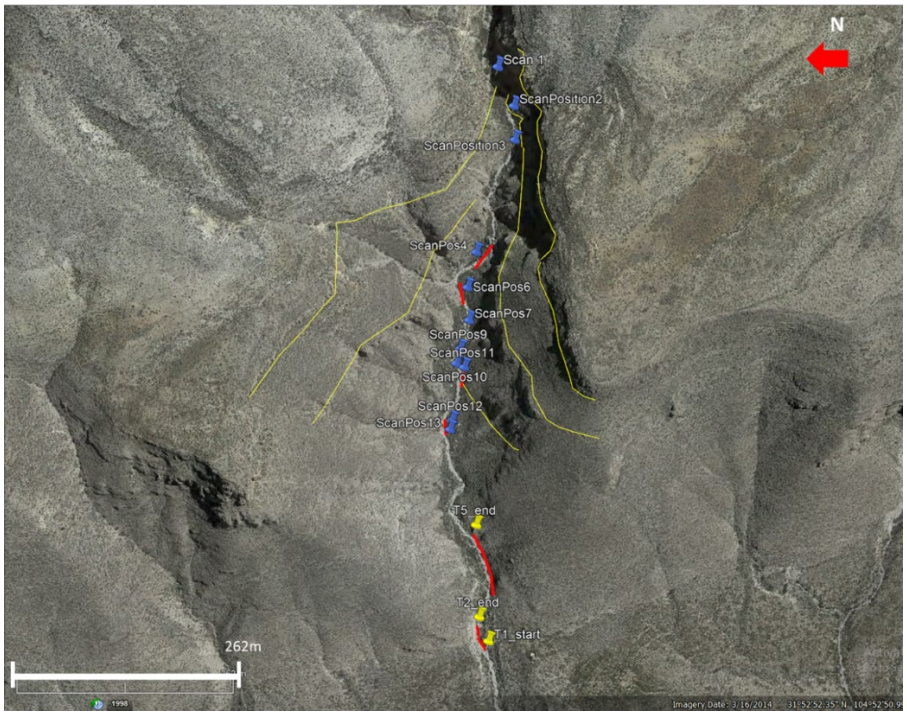

Figure 14: Relation of LiDAR scan positions to field-measured transects (red) within Bone Canyon

`

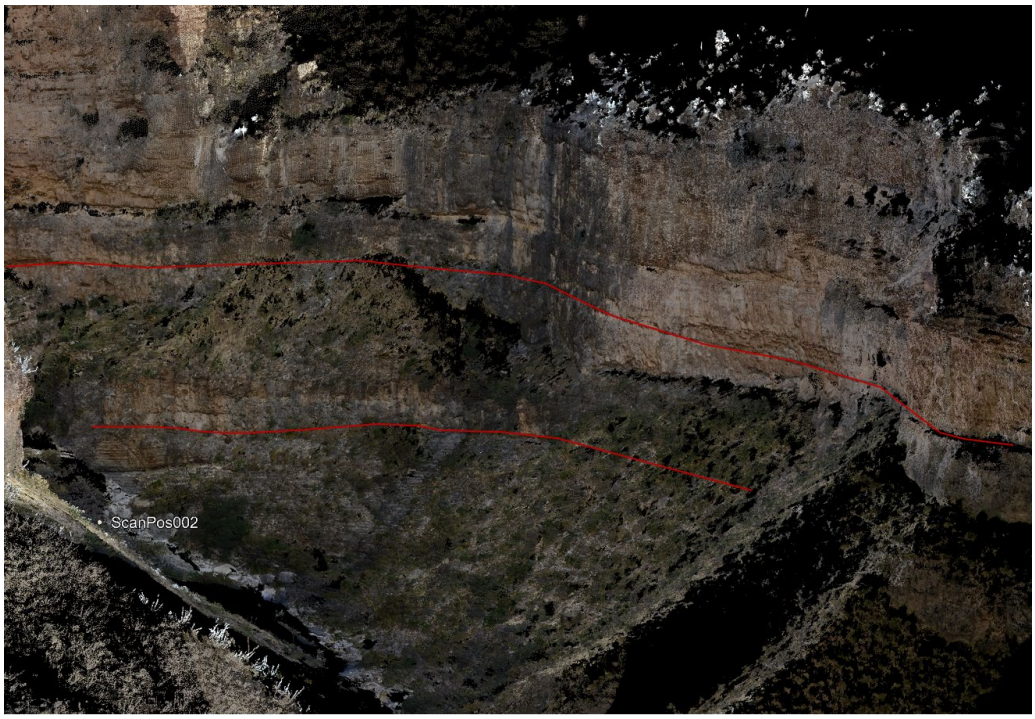

Figure 15: Point cloud data displayed in true color. Also shown is scan position 002 and formation boundaries of the Bone Spring/Cutoff formations (bottom line) and Brushy Canyon/Cutoff formations (Top line)

3.4 X-Ray Fluorescence data collection and processing

X-Ray Fluorescence measurements were taken using a Thermo-Fisher Scientific XRF device, in order to further support lithology interpretations made by LiDAR reflectance and amplitude. These were combined with petrographic interpretations of lithofacies, to compare with SilverSchmidt readings for potential relationships between measured lithology, elemental analysis, and mechanical measurements. Other uses of XRF data include the interpretation of paleoenvironment using various geochemical proxies and ratios. XRF readings consisted of a 220 second measurement interval, with three measurement filters designed to measure highly sensitive elements.

Filters consisted of high, main, and low, with each assigned to a relative range of elements. “Main range” filter corresponds to elements ranging from Manganese to Bismuth.

`

“Low” range is used to optimize the sensitivity of elements Titanium through Chromium. Finally, “High range” is ideal for sensitive elements such as Silver through Barium. Internationally accepted standards were used to calibrate the XRF device including PAAS and SARM-41 sample provided by Thermo Scientific. Once measurements occurred, all data was transferred from the device to the Thermo Scientific software, which was then correlated through multiple cluster analysis. All measurements are reported in ppm. A light range filter was also applied for a duration of 60 seconds and was applied in order to read elements with a sensitivity not recorded by other filters. As measurements recorded at transect 1 failed to measure Uranium and Thorium contents due to internal system errors, they have been omitted from the creation of pseudo-gamma ray curves conducted on other transects. In total, 180 data points were recorded within the Bone Canyon outcrop. XRF-derived mineralogies were computed using programs created by Pigott (unpublished).

3.5 SilverSchmidt data collection and mechanics

The Schmidt Hammer has long been used in outcrop studies as a method to derive mechanical data in an affordable, non-destructive manner. With easy portability, utilization was necessary considering the harsh terrain, as well as to support the ongoing effort to not disturb outcrop features in Bone Canyon. The original mechanical Schmidt hammer was developed by Ernest Schmidt in 1951, in which a metal plunger with a spring-loaded mass impacts the surface of a rock. The rebound of the energy returning from the rock is then recorded internally. The rebound value collected from the sample is dependent on the hardness of the rock. Considering the relationship between rock hardness and rock density (Viles et al., 2011), rebound hardness could give insight into the mechanical characteristics of the Bone Spring.

`

Though Ernest's first development of the Schmidt Hammer required the correction of directional bias using conversion charts, the modern development of SilverSchmidt hammer records data electronically, internally corrected for horizontal or vertical variation (Q value) (Viles et al., 2011). It should be noted that measurements ideally should be recorded perpendicular to the rock face. The recorded Q value from the SilverSchmidt can also be defined as the inbound velocity divided by the rebound velocity. Figure 16 shows the correction of Q to R, and the correlation of R to unconfined compressive strength. All samples were collected using an L-type SilverSchmidt rebound device. All sample locations were sanded before data was collected. Samples were consistently recorded perpendicular to a relatively flat, prepared rock surface, either from the vertical direction or the horizontal direction.

In total, 110 data samples were taken, all associated with XRF measurements in identical positions. 17 of these samples also correspond to petrographic samples. All samples were sanded before testing commenced. It should be noted that previous studies have stated that variation exists between hydrous and anhydrous samples. However when samples were tested before and after water was applied and allotted time to become hydrous, measurements showed negligible variations in this scenario.

As mentioned previously, Studies done by Katz (2000) demonstrated a correlation between the R value of the Schmidt hammer to unconfined compressive strength. Although this correlation was used in this study, it should not be implemented due to the non-ideal rock conditions in this study. Other correlations, defined in table 1, have also been referred to in this research as a method to compare the Katz data correlations. The Katz study consisted of even rock types, varying in lithology. Lithologies sampled ranged from fine grained/granular sedimentary rocks to crystalline igneous samples, with sedimentary rocks ranging in calcite

`

cementation (Katz, 2000). The correlation coefficient of R^2=0.964 was achieved, though excluding soft rock samples drastically reduced the resulting R^2.

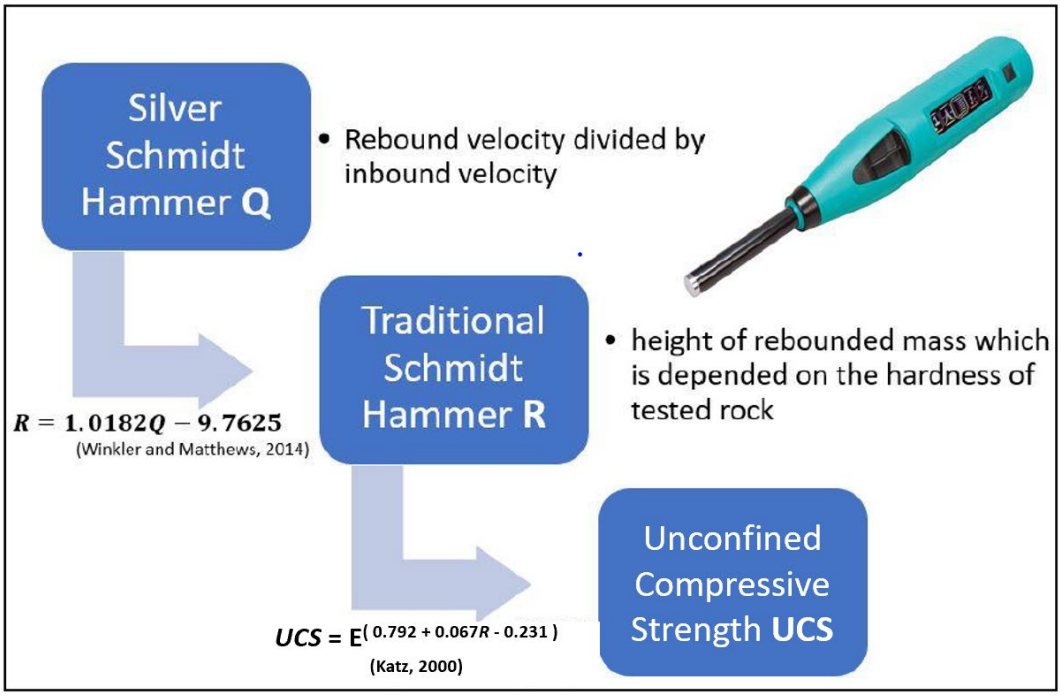

Figure 16: Correlation of SilverSchmidt Q value to rebound ratio and unconfined compressive strength, Modified from Wang 2018

4. DATA AND OUTCROP CHARACTERISTICS

This study utilized hand samples collected from Bone Canyon to create thin sections for petrographic analysis. Overall, two hand samples were collected from this research study, with the utilization of 13 thin sections previously created from Bone Canyon research collected through Andrew Brown (unpublished). Thin sections incorporated in this study encompass the intervals of the Cutoff Formation and 1st Bone Spring Carbonate. Table 2 displays thin section descriptions for all samples analyzed. Outcrop descriptions were also recorded for the Cutoff Formation and 1st Bone Spring Carbonate, with further separation of the 1st Bone Spring Carbonate into sub-formations of Carbonate A and Carbonate B. A siliceous mudstone identified

`

at the mouth of Bone Canyon, denoted as the 1st Bone Spring Carbonaceous Sand. The separation of the 1st Bone Spring Carbonate into intervals A and B was determined based upon variations in biogenic chert formation, and the identification of truncating beds and onlapping fill within the carbonate interval. Data collection within Bone Canyon also included the collection of XRF and Schmidt Hammer measurements. Overall, 140 XRF and 110 Schmidt Hammer Measurements were gathered, spanning the Cutoff Formation to the 1st Bone Spring Carbonaceous Sand.

4.1. Petrography and Outcrop Descriptions

In addition to sample collection, outcrop observations were recorded within areas of interest identified within the canyon. Figure 17 displays outcrop photography of four identified areas of interest, including the 1st Bone Spring Carbonate Sand (17A), 1st Bone Spring Carbonate B (17B), upper Bone Spring Limestone (17C), and the Cutoff channel sand (17D). Petrographic samples taken from each area serve to heighten stratigraphic interpretations within the canyon, with the confirmation of lithologic transitions. Overall, distinct lithology variations can be identified on a 1st order inference, transitioning from biogenic siliceous carbonate in 17A, to bedded chert-dominated mudstone within 14B, blocky, massive mudstone illustrated by 17C, as well as very fine, amalgamated sandstones in 17D. Between 17B and 17C exists a Carbonate A, identified as nodular chert-dominated mudstone more prevalent. Outcrop interpretation from Carbonate B concluded that the presence of bedded chert is dominant, with the presence of few, large (~0.5-1m diameter) nodules are present. This interpretation is heightened by an observed stratigraphic unconformable surface present between the bed-dominated chert and nodular-chert dominated sequence, thus the two have been separated into Carbonate B followed by Carbonate

`

A stratigraphically above. Overall, this stratigraphic interpretation serves as a framework to infer mechanical properties from the outcrop and assign within a particular stratigraphic interval within the canyon.

Figure 18B illustrates the presence of radiolarian, coupled with benthic foraminifera and bivalve skeletal fragments. Trolibite skeletal fragments were observed sparsely through the sample. Trace amounts of biogenic silica (<5%) were also observed. Overall the sample displays amorphous pore space throughout, coupled with dissolution dominated diagenetic features (Pigott, 2017). The cement consists of sparry calcite with kerogen-rich fibrous layers also present. No fracture-produced secondary porosity was observed within the sample.

A kerogen-rich siliceous mudstone was identified within Transect 9, illustrated in Figure 18D. Sitting stratigraphically below the Cutoff Conglomerate, the sample could potentially have been derived from the upper Bone Spring Limestone. However, this cannot be confirmed due to a lack of stratigraphic boundaries observed thought the boundary is likely included within a covered interval in Bone Canyon. Biogenic silica was also observed in trace amounts. Chert replacement within allochems present in sample is dominant, often found within dissolution of crinoid centers. Matrix consists of primarily micrite, as opposed to the sparry-dimicrite common within the lower Carbonate interval. Sample OU-2154-PMNM collected from transect 1 indicated by Figure 18A displays a siliceous mudstone, dominated by biogenic silica and partial dolomitization. Dolomitization present within the sample can be described as having a planar-rhombic structure, with cloudy centers and displaying a hypotropic-mosaic (Pigott, 2017). Radiolaria, siliceous diatoms present with dissolved skeletal fragments. Sweeping extinction exists within calcic spears present in thin section, suggesting low-mg calcite replacement of aragonite. Grading can also be observed within thin section, with very fine-grained biogenic

`

quartz encompassing fined grained silica in a spar-dimicrite matrix. The presence of radiolaria, diatoms, and lack of sedimentary structures from outcrop observations suggests that the interval observed is associated with a high-stand depositional event, supporting the high frequency of radiolaria sponge (Pigott, 2017). Therefore, this interval is more appropriately associated with the HST of the 1st Bone Spring Carbonate, contradicting past work identifying the interval as the 1st Bone Spring Sand (Alabbad, 2017). Fractures observed from outcrop observations show a NW-SE trend (~120º/81SW) with calcite infill.

Figure 18C displays a chert/chalcedony dominated wackestone. With kerogen-filled crinoid centers, surrounded by a sparry calcite ring. Sample OU-21560-PMNM displayed in Figure 18C was collected from the interbedded chert/mudstone dominated transect 4. Overall, chert beds within the 1st Bone Spring Carbonate show high volumes of chert/chalcedony cement, with ~10-20% allochem concentration. Figure 18C also reveals the presence of a radial ooid, which is interpreted to be transported form the shelf. Trace amounts of potassium feldspar was also observed in trace amounts. Overall, petrographic investigation not only suggested the presence of biogenic silica

Figure 16A consists of a photomicrograph of the Cutoff sand channel proximal to scan position 1. It is a subarkose displaying calcite cement and partial dolomitization. Grains consist of very fined grained sub-angular to angular quartz, with Potassium and albite also identified in trace amounts (<5%). Furthermore, abundant fracture porosity was identified within the sample, corresponding to lower Schmidt Hammer rebound velocity measurements and an observed inverse relationship with average bedding thickness. Lack of trace fossils or replacement features within the sample suggests a detrital sourced siliceous input, in contrast to the 1st Bone Spring Carbonaceous Sand biogenic source. The sand channel identified within the Cutoff Formation

`

also displays soft sediment deformation features associated with sub-aqueous depositional features. This deposition is interpreted to be associated with a basin-wide low stand period, a transition period from high-stand (FSST) (Montgomery, 1997; Crosby, 2015).

Figure 19B illustrates the Cutoff conglomerate a Calclithite dominated by sparry calcite cementation. Grains are rounded to sub-rounded, poorly sorted clasts in a calcic/partially dolomitized matrix. Clast size ranges from 65 microns to 6 mm, consisting of allochem-abundant, calcite-rich cobbles. Cobbles are inferred to be sourced from shelf material into deeper water. Furthermore, two generations of isopachous cement have been identified within the sample, consisting of an early stage marine cementation, with a second stage calcic spar isopachous cementation ring. The spar observed within the second cementation is indicative of marine vadose cementation. Intraclastic microcrystalline dolomitization is also observed, with cloudy exposure

Table 2. Thin section descriptions of samples collected from Bone Canyon. Interpretations made through Pigott (2017).

Sample #	Transect #	Description
OU-2128-PMNM	Lower Bone Spring	Siliceous Mudstone: Radiolaria, Diatoms observed frequently with biogenic silica and calcite-rich clasts (605-40%). Dissolved skeletal fragments also present. Secondary fracture porosity present infilled by calcite grains.
OU-2130-PMNM	Upper Bone Spring	Wackestone: 10-20% allochems; Benthic Foraminifera, skeletal fragments dominant. High occurrence of calcic spears. Secondary porosity exists with infill of silica and feldspar grains
OU-2131-PMNM	Cutoff Conglomerate	grains: rounded-subrounded, poorly sorted clasts in calcite/partially dolomitized matrix. Clasts (65µ-6mm), consist of calcic cobbles. Allochems include brachiopods, Mollusca fragments, radiolaria, formainifera. Most clasts most likely shefal sourced. Two generation isopachous cement present
OU-2132-PMNM	Cutoff Channel sand	Subarkosic- Grains: angular/sub-angular, vf grained silica grains. Predominantly silca, with small amounts (~5%) of clasts being felsphathic. Calcic cement, partially dolomitized. Intergranular porosity present, with secondary fracture porosity present. Open fractures present
OU-2153-PMNM	Transect 1	Siliceous Mudstone-Wackestone, w/ biogenic silica prevalent through dissolution o/sponge radiolaria. Low-Mg Calcite replacement of aragonitic Bryzoan. Grading present within sample. Partial dolomitization also present, with secondary fracture porosity present
OU-2154-PMNM	Transect 1	Siliciceous Mudstone; foraminifera, bryzoan, brach fragments present (detrital, shelfal). Radiolaria, biogenic quartz prevalent. Diagenesis: dissolution dominant. Kerogen present through infill of crinoid dissolution. Dolomite: hypotropic mosaic, planar rhombic structure.
OU-2155-PMNM	Transect 3	Carbonaceous Chert: Chert precipitation dominant. Foraminifera, calcic spears, crinoids, siliceous radiolarian present. Trace k-feldspar present. Chert/chalcedony-length slow. Kerogen staining prevalent. Diagenesis: dissolution. Secondary fracture porosity present
OU-2156-PMNM	Transect 4	Siliceous Mudstone-Wackestone: dominated by Chert-Chalcedony precipitation. Kerogen staining present, with trace feldspars. Radial ooid identified, likely shelfal source material.
OU-2157-PMNM	Transect 5	Chert-bearing Mudstone-Wackestone: siliceous radiolarian sponge, crinoids, brachiopod fragments, sparry calcite spears, ostracod fragments present. Diagenesis: dissolution, with kerogen filled pores. Chert/Chalcedony-length fast. Planar dolomitization
OU-2158-PMNM	Transect 6	Chert-bearing mudstone. Biogenic silca present (~20%), with spar calcic matrix. Kerogen-filled pores present, with radiolarian sponge dissolution observed within kerogen pore space. Sparry calcite spears and brachiopod shell fragments also observed.

Sample #	Transect #	Description
OU-2159-PMNM	Transect 6	Radiolarian Mudstone-Wackestone: Prevalent Radiolarian sponge spicules observed with sparse brachiopod fragments, ostracod, benthic formainifera present. Spar calcic matrix prevalent with fibrous, kerogen-filled laminations observed. Vuggular porosity identified. Diagenesis: dissolution
OU-2160-PMNM	Transect 8	Radiolarian Mudstone-Wackestone: Benthic foraminifera identified with abundant radiolarian sponge spicules. Sparry calcite matrix with micritic fibrous laminations also observed. Kerogen-filled pores present. Sparry calcite replacement of outer ring of crinoids.
OU-2161-PMNM	Transect 9	Kerogen-rich Mudstone: lack of radiolarian sponge spicules commonly identified within other samples. Outcrop shows massive, blocky structure. Sparse foraminifera and radiolaria identified, along with sparse biogenic silica. Oil staining prevalent. Chert replacement also common.
OU-2162-PMNM	Transect 10	Radiolarian mudstone-wackestone: Similar to OU-2160-PMNM. Benthic Foraminifera, siliceous radiolaria, and crinoids present. Spar-dimicrite cementation identified within matrix material. Partial planar dolomitization also observed. Allochem lineation observed with length of slide.

`

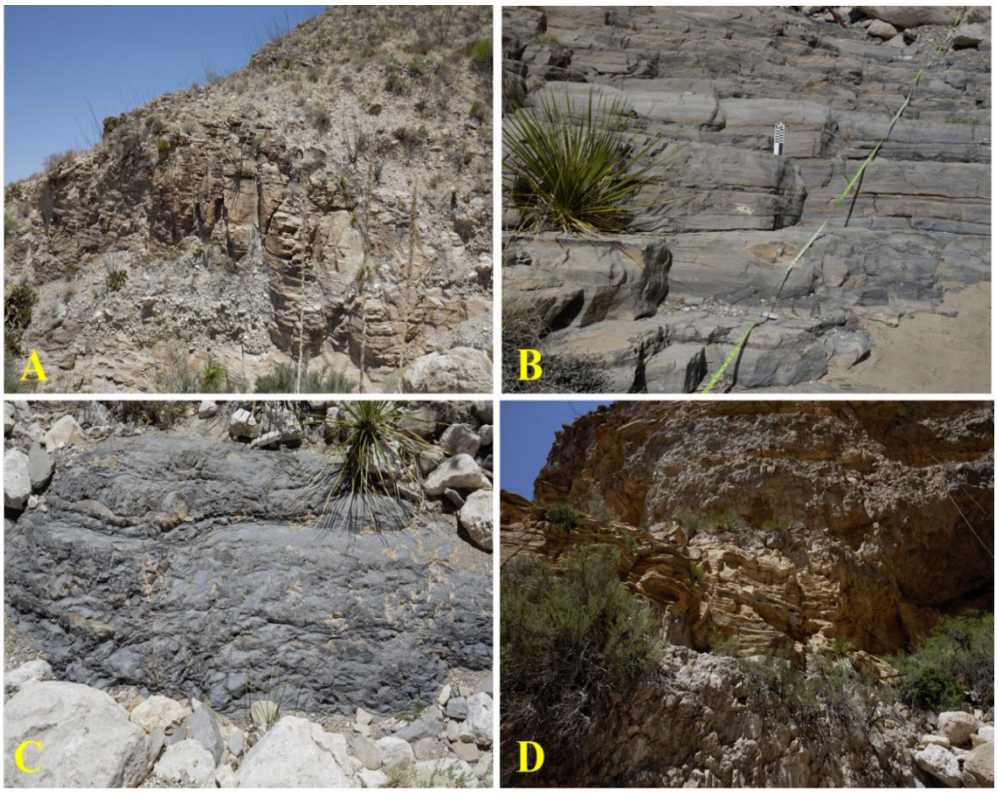

Figure 17: (A) Transect 1 measured interval, inferred 1st Bone Spring Carbonaceous Sand, (B) Transect 6 measured interval, interpreted Bone Spring Carbonate B, (C) Transect 8 measured interval, inferred Bone Spring Limestone, (D) Transect 9 measured section, interpreted Cutoff channel sand.

`

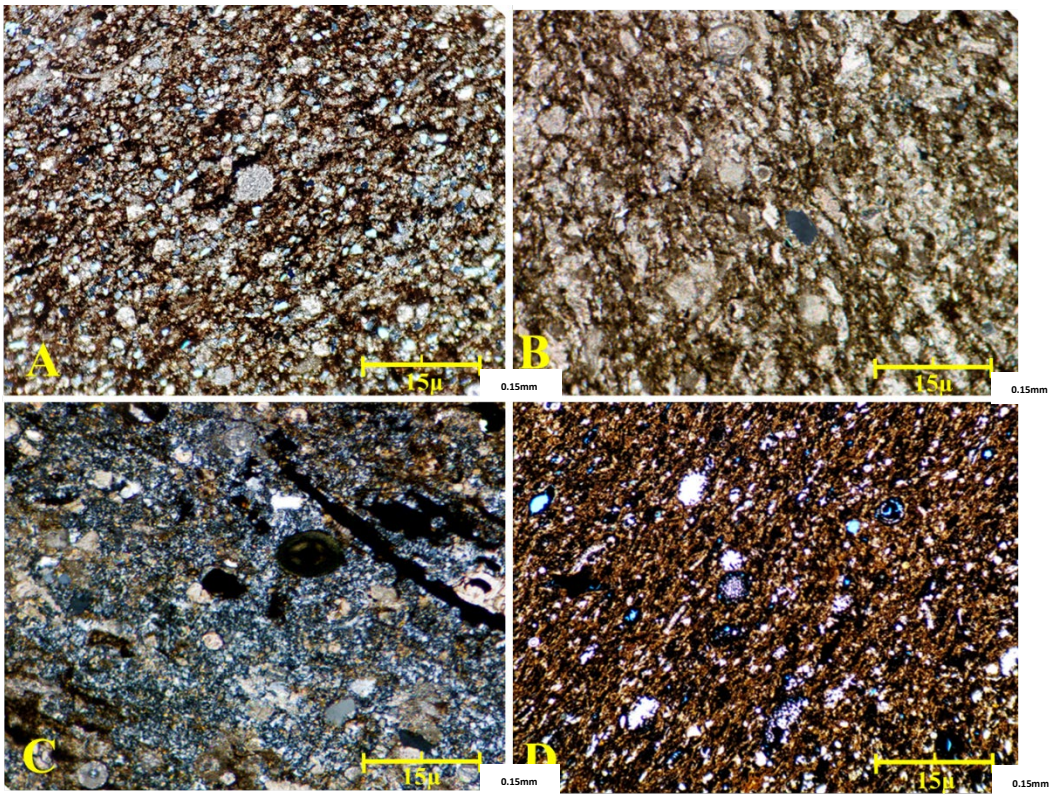

Figure 18: (A) Siliceous mudstone, from sample OU-2154-PMNM. Note Radiolarian present within slide. Benthic foraminifera present with ~40% biogenic silica grains. Dolomitization is dominated by planar-rhombic structure, cloudy centers with hypotropic mosaic. (B) Radiolarian-rich Mudstone, identified within the Bone Spring Carbonate A. Vuggular pore space identified with dissolution-dominated diagenetic features were observed. (C) Predominantly biogenic chert, with presence of micritic calcite and fossils also present. Trace feldspar (<5%) observed sparsely. Kerogen-filled crinoids due to center dissolution also present. Note presence of radial ooid, interpreted to be transported from upward shelf, due to its trace amount (<1%). (D) From inferred Bone Spring Limestone; Radiolarian-dominated mudstone. Cementation is micrite with high volumes of kerogen-filled fractures present within the sample. Chert replacement of crinoids are common throughout, with biogenically sourced silica also present. Outcrop photograph can be observed in Figure 14C. Power 4x cpl

`

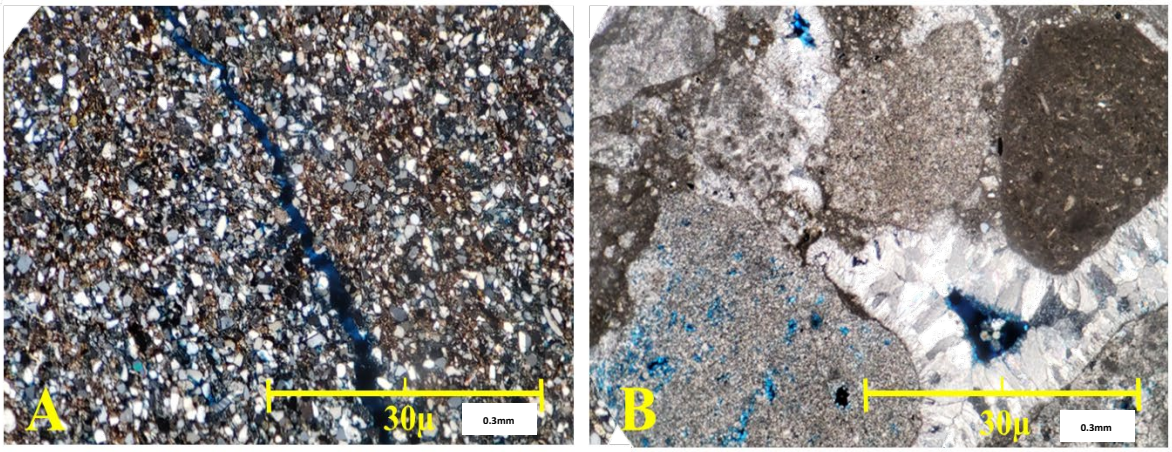

Figure 19: (A) Arkosic Quartzarenite identified within the Cutoff conglomeritic unit. Note the presence of secondary fracture porosity. (B) Calclithite identified within the Cutoff Formation in Bone Canyon. Two generations of isopachous cement can be observed, giving evidence for re-cementation involved with sub-aqueous, shallow exposure. Hydrocarbon staining around cementation rims indicates later hydrocarbon migration. Power 4x, CPL

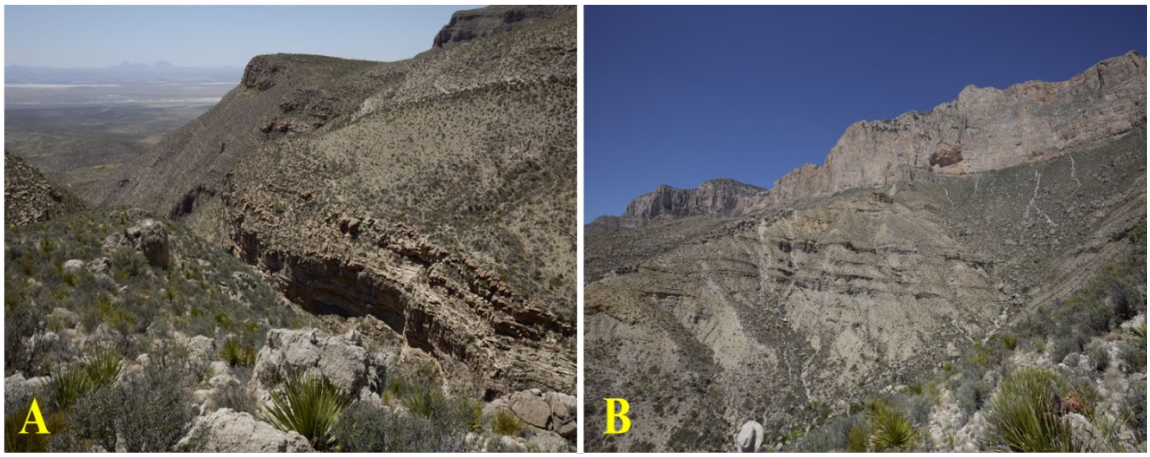

Figure 20: (A) Southwest oriented photograph of Bone Canyon, with the Brushy Canyon formation defined. (B) inferred later Guadalupian sedimentation.

`

Figure 21: Chert-cemented, high angle fractures identified with an approximate NE-SW orientation. Complimentary, shallow angle fracture with chert cementation also identified, with chert nodules being prevalent. Fractures labeled by red arrow

4.2. XRF Data

A total of 140 XRF measurements were recorded throughout the measured interval within Bone Canyon, with the purpose of identifying mineral composition of relevant stratigraphic intervals, and to attempt a correlation with Schmidt Hammer rebound intensity. Appendix A outlines derived XRF-mineralogy data from all transect measured. Sampling interval varies within all transects excluding transect 1, which is set at a 1ft sampling interval. This method was chosen with the effort to correctly represent chert bedding within the Bone Spring Carbonate. For determining relative correlations to the Schmidt Hammer data, the XRF estimated mineralogy was displayed using a weighted 2-point average, and a common sampling interval of

`

10 feet. Dominant mineralogy present within most transects consists of heavy calcite and chert precipitation, with secondary dolomite and clay minerals, with trace pyrite also present. It should be noted that transects within Bone Canyon represent measured section of the canyon and does not reflect vertical stratigraphic depth. Overall, trace amounts of gypsum (<6%) was observed only within transect 1. Pyrite was observed in larger amounts (10-20%) within all transects measured within Bone Canyon. Gypsum deposition within carbonates can be indicative of sub-aqueous deposition (Schreiber, 1987), while high pyrite precipitation may be indicative of hydrocarbon migration (Ghazban, 2010). A Psuedo-gamma ray log was also derived using correlations with spectral gamma for all transects measured excluding transect 1, owing to malfunctions in sampling equipment previously described.

4.3. SilverSchmidt data

Approximately 150 Schmidt Hammer rebound intensity readings were recorded throughout Bone Canyon, spanning roughly 914m of measured section, with 110 being utilized in this study. Overall, readings fluctuated from average Q of 15 to 90, with R values in the range of 20-85. The largest fluctuations were observed within Transect 6 and Transect 1 (Bone Spring Carbonate A and the 1st Bone Spring sand. Because this study did not allow for compressive strength tests or density measurements, Poisson's ratio was assumed to equal $\sqrt{3}$, representing isotropic rock. Columns marked with ln(E) represents an intermediary step involved with the correlation equation of Young's moduli, from Katz et al (2000). Furthermore, columns under ln(U) mark an intermediate step in the correlation equation of rebound values and unconfined compressive strength (UCS), also from Katz et al (2000). Rebound factors were derived from Q values measured with the SilverSchmidt device, using correlations derived through studies done

`

by Wrinkler and Matthews (2014). Correlation of the brittleness index defined by Wang et al to rebound values and R values shows no correlation. No correlations were also observed in clays vs R, or pseudo-gamma ray vs R. Figure 22 illustrates Quartz/Dolomite volume vs. R. Appendix B outlines all raw Q data collected from outcrop examination.

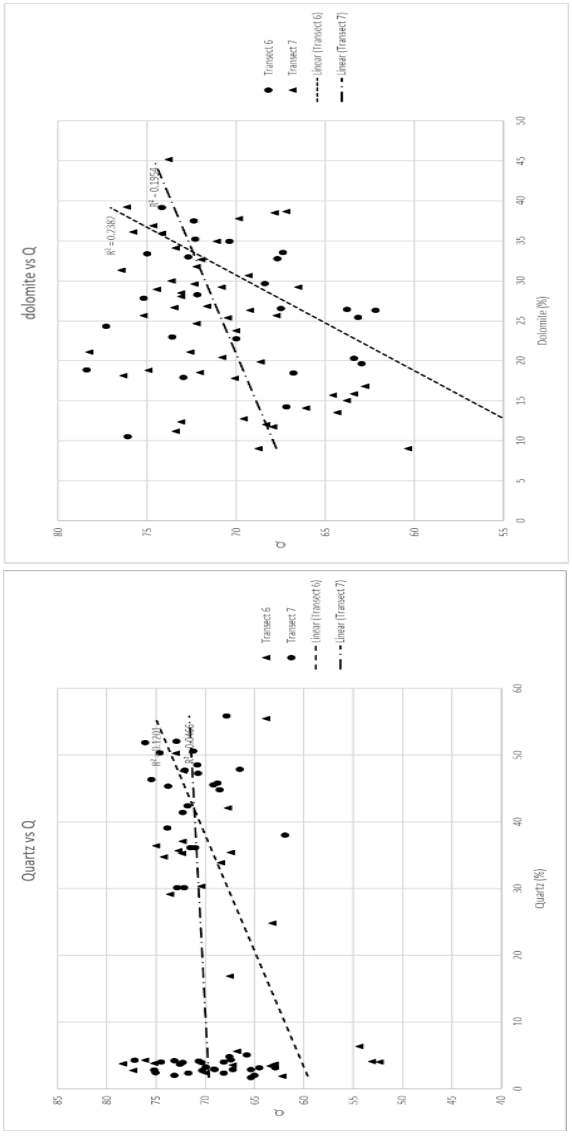

Figure 22: Correlation of SilverSchmidt Q readings with XRF-derived quartz (left) and dolomite (right) mineralogy.

`

5. RESULTS

5.1. LiDAR constrained stratigraphy

Figure 23 illustrates the approximate stratigraphy of Bone Canyon. Stratigraphic positions were determined through the description of outcrop samples, including LiDAR based facies interpretation from Transect 1 through Transect 10. Figure 23 also illustrates pseudo gamma-ray profiles recorded for stratigraphic intervals examined. Figure 24 defines lateral variation in transect measurements, and their relation to formation contacts. Furthermore, an inferred relative sea level curve has been included, showing correlation with pseudo gamma-ray measurements. Pseudo gamma-ray (PGR) correlations were performed using programs created by John Pigott (unpublished, 2019). Equations regarding the estimation of PGR can be found in figure 26. Stratigraphic boundaries were interpreted based upon 1) The presence of onlapping beds to an unconformable surface. 2) lithologic changes identified on X-Ray Fluorescence or LiDAR reflectance. 3) variation in elemental proxy responses. The boundary between The Cutoff formation and Brushy Canyon formation was determined based upon LiDAR imagery, which observed lithologic facies transitioning from massive, cobble dominated calclithite to bedded, fine grained detrital sandstone, similar to what was interpreted by Beaubouf et al. (1999).

Satellite images from Google Earth were used to further improve stratigraphic interpretations across the canyon, due to the incomplete coverage from the combined LiDAR image. Boundaries between the Bone Spring Limestone and the Cutoff Conglomerate were determined by lithology transition from detrital calclithite dominated siliciclastic deposition to carbonate deposition, identified from LiDAR true color images, LiDAR reflectance, thin section analysis and outcrop description. Stratigraphic boundaries between the Bone Spring Limestone

`

and Bone Spring Carbonate A were determined based off of the identification of a large unconformity, and lithology transition based on LiDAR reflectance. Boundaries between Bone Spring Carbonates A and B were determined through lithologic transitions from interbedded chert to nodular chert, accompanied by the presence of an unconformable surface at the base of the Transect 7 measured section. Finally, stratigraphic boundaries between the between the 1st Bone Spring Carbonate sand and Carbonate B were inferred based on field observations (gradual lithology variation throughout transects 1-3), as well as referencing to satellite imagery.

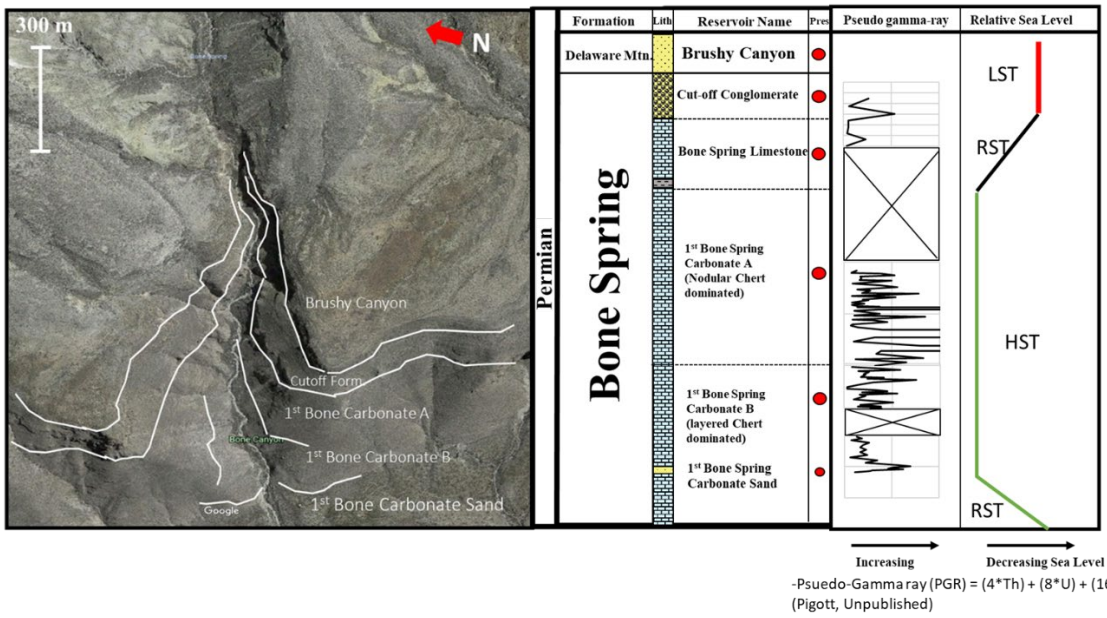

Figure 23: Approximation of stratigraphic positions within Bone Canyon. It should be noted that the Bone Spring Limestone is combined with the Bone Spring Carbonate A, for the purpose of clarity within a compressed satellite image. Pseudo gamma-ray collected from XRF data is also recorded, including an inferred sea level curve.

`

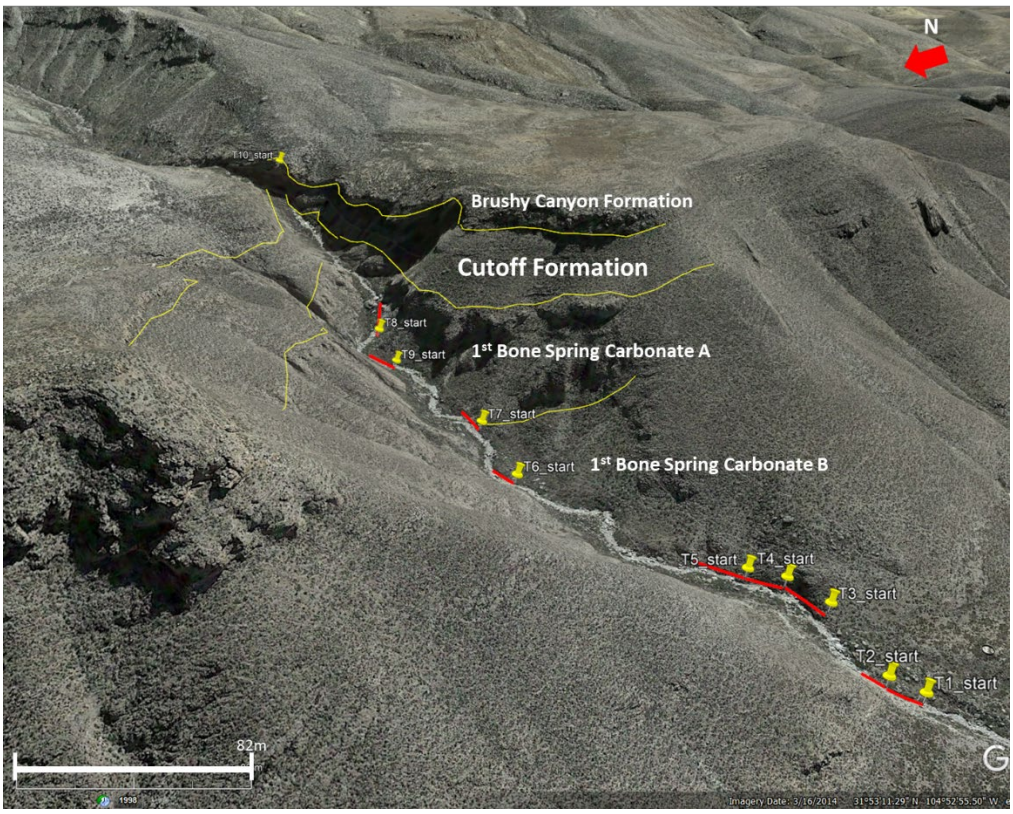

Figure 24: Relation of field-measured transects to Bone Canyon outcrop formations illustrating lateral variation

5.2. Split-FX

Rock mass characterization software Split-FX utilizes XYZ RGB ASCII formatted point cloud data to extract fracture information such as strike orientation, strike dip, total fractures, fracture trace identification, and volume measurements. XYZ refers to a Euclidean spatial reference system in which X is latitudinal spacing, Y is longitudinal, and Z is vertical. Split-FX also allows the user to import true color information, R representing red, B being blue, and G representing green. Once imported into the software, the point cloud data must be oriented in reference to the relative scanning position, by specifying pitch, yaw, and relative horizontal position of the scanner (Hanzel, 2014; Alabbad, 2017). The ideal scanning position is

`

perpendicular to the investigation surface (Split Engineering, 2019). Once the scanning position has been specified, a data QC is performed, eliminating noise and outcrop cover (plants, debris, shadows, etc.). The desired measurement space is then specified, recording overall area measured. Points within the desired measurement area are then triangulated based upon user specified parameters such as points per triangle. Minimizing shadows can be acquired by increasing point spacing (Hanzel, 2014; Alabbad, 2017). In order to identify small fracture planes present within the outcrop, this study utilized a point spacing of 1-10 minimum points per triangle. Triangles are then grouped by user defined similarities including minimum patch size and minimum neighbor angle. This study utilized a minimum patch size of 5-13 triangles per patch, and a maximum neighbor angle of 13. Patches can then be viewed on a stereonet and selected based on orientation. Patches can represent features such as bedding planes, outcrop orientation, and fractures surfaces. It is imperative that the user determines which orientations resemble fracture surfaces, based upon outcrop interpretation. Data must be quality controlled based upon interpretations made in the field, as well as point cloud interpretations made in Split-FX.

5.3. Fracture Populations

Fracture orientations were recorded from 7 different areas of interest, including scan positions 1, 3, 10, 11, and 13, or the approximate positions of transects 9, 10, 7, and 6 (refer to Figure 7 and Figure 14). The examined scan positions encompass the Cutoff Conglomerate, Cutoff sand channel, Bone Spring Carbonate A, and Bone Spring Carbonate B. Strike and dip information were exported from Split-FX and imported into Microsoft Excel and GEOrient for strike frequency analysis and rose diagram creation. Strike frequencies and dip information were

`

then referenced to field measured fracture strike and dip, defined in figure 25. This was conducted in order to confirm the precision of measurements within Split-FX.

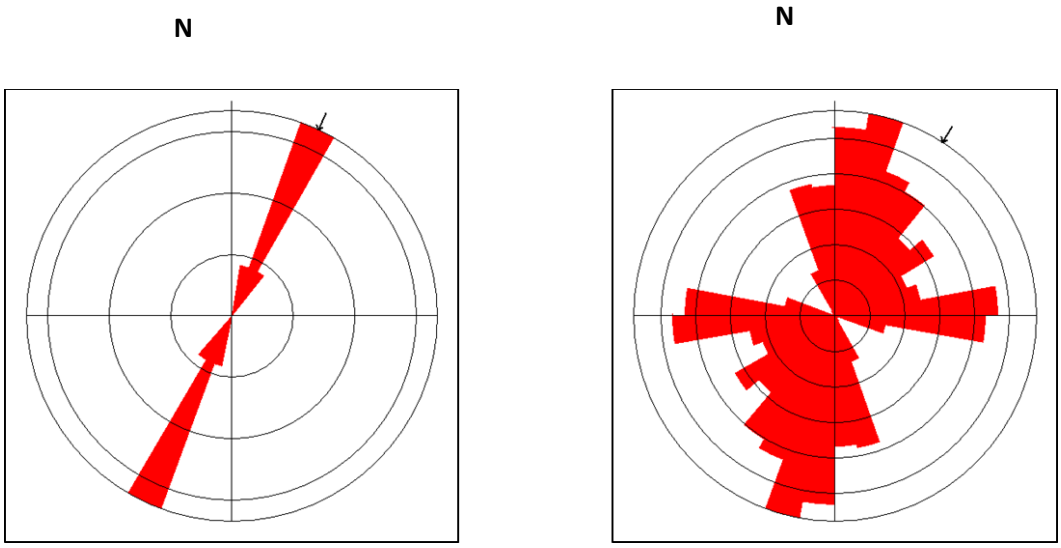

Figure 25: Ground truth (left) fracture orientations measured within the Bone Spring outcrop, and (right) fracture orientations measured in Split-FX. The substantial increase between data collected from the field and LiDAR extraction should be noted, with 6 field measurements in ground truth measurements and 545 extracted through Split-FX

5.3.1. North Wall: Cutoff Conglomerate

An area of 443.62 square meters of the Cutoff conglomerate north wall exposure was analyzed in order to extract fracture information. Figure 26 displays the analyzed section within Split-FX. Overall, 364 fracture planes were identified within the observed area, with bimodal distribution peaks in strike frequency observed within 30-70° and 150-250°. Mean resultant direction analyzed is 121°-301°. Primary sets are interpreted to be the NE-SW trending 30-70° set with a secondary set striking NW-SE. Fracture density was derived by dividing total the number of fractures by square meter of area observed. Subsequently, fracture density was observed to be 0.821 fractures per square meter. Average bedding thickness observed within the

`

Cutoff conglomerate was 1.646 meters to 1.746 meters. Average bed thickness was gathered using the ruler function within Split-fx and compared with field observations to ensure procession. The Cutoff Conglomerate within the North wall has the highest observed bedding thickness, with the lowest recorded fracture density. Figure 27 illustrates strike information from stereonet view, strike frequency, rose diagram view, area observed, total number of fractures, and fracture density.

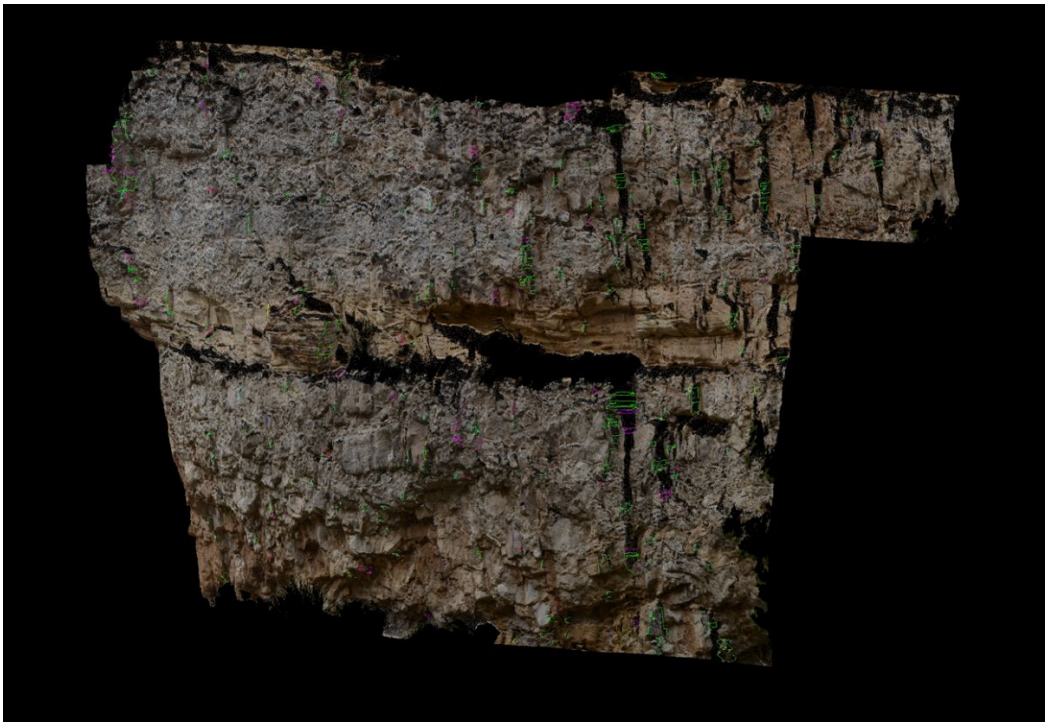

Figure 26: LiDAR image of cutoff conglomerate, proximal to transect 10. Average bed thickness observed within the analyzed interval was 1.2 meters, with a fracture density of 0.821 per meter squared.

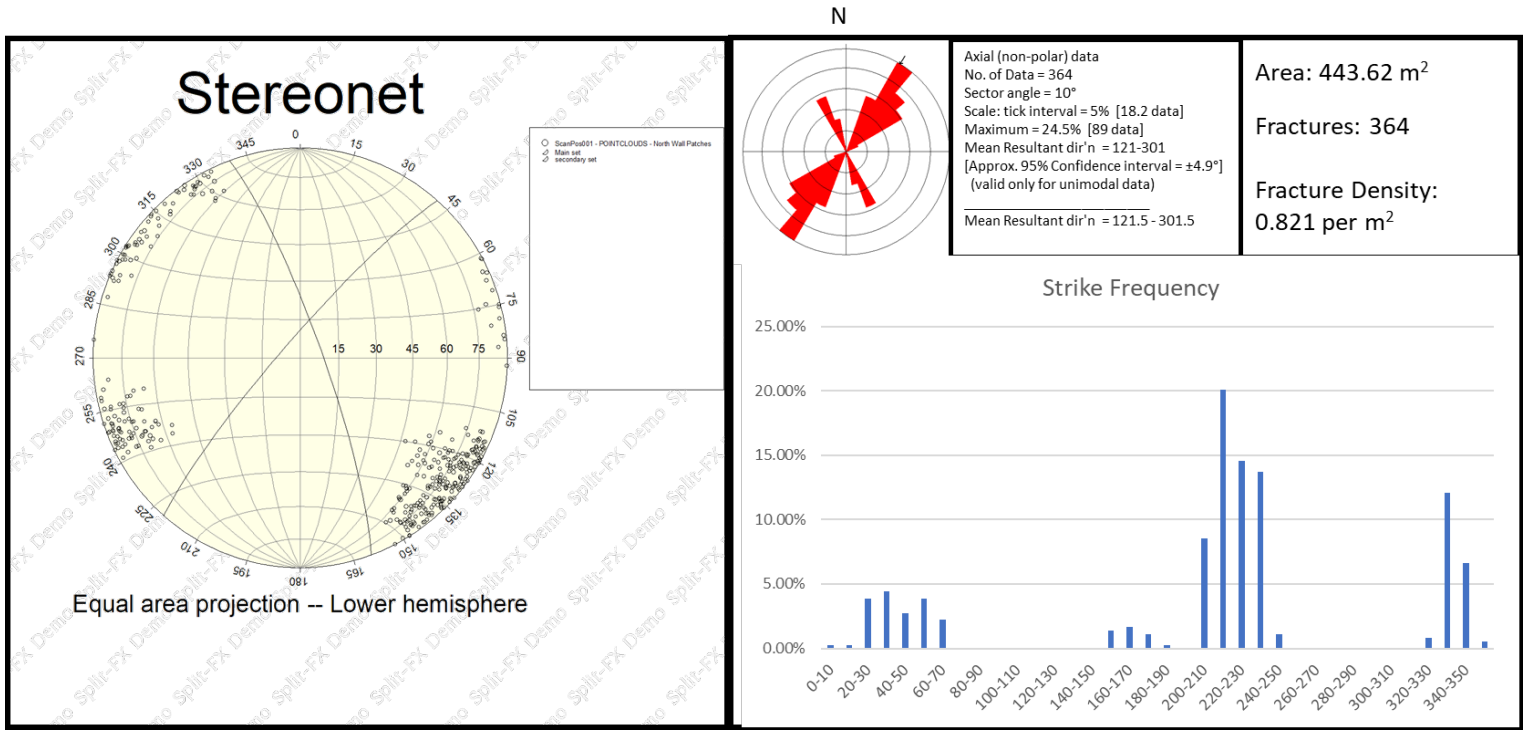

Figure 27: Illustration of extracted fracture information from the north wall exposure of the Cutoff conglomerate. Stereonet view includes all fracture poles, with great circles representing fracture sets (Holcombe, 2019).

`

5.3.2. North Wall: Cutoff Sand Channel

The Cutoff channel sand identified within the Cutoff conglomerate consists of 167 square meters of area, with a total of 772 fractures identified. Figure 28 shows the examined interval of point cloud data within Split-FX. Overall, strike frequencies extracted from Split-FX show a normal distribution, with a mode of 40-50° (NE-SW). a minor, orthogonal secondary fracture set can be observed at 120-140° strike (NW-SE). Average bed thickness observed within the examined interval is 0.266-0.321 meters, with a fracture density of 4.6 per square meter. Figure 29 displays strike frequency within a 2D chart view, with a stereonet view of all fracture great circles, as well as strike frequency in rose diagram view, with area observed, fracture density, and total fractures identified.

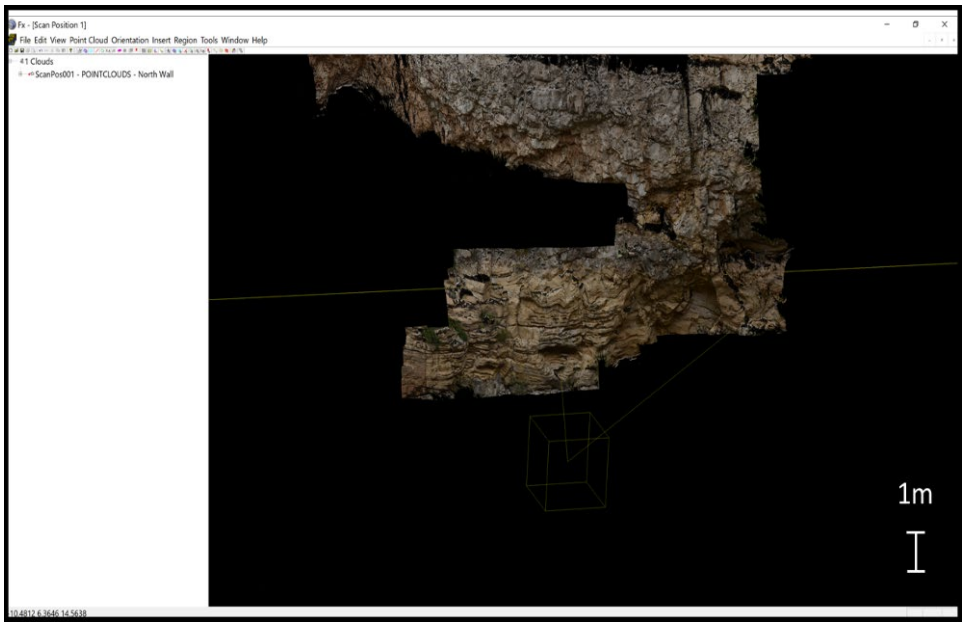

Figure 28: True color point cloud view of Cutoff channel within Split-FX.

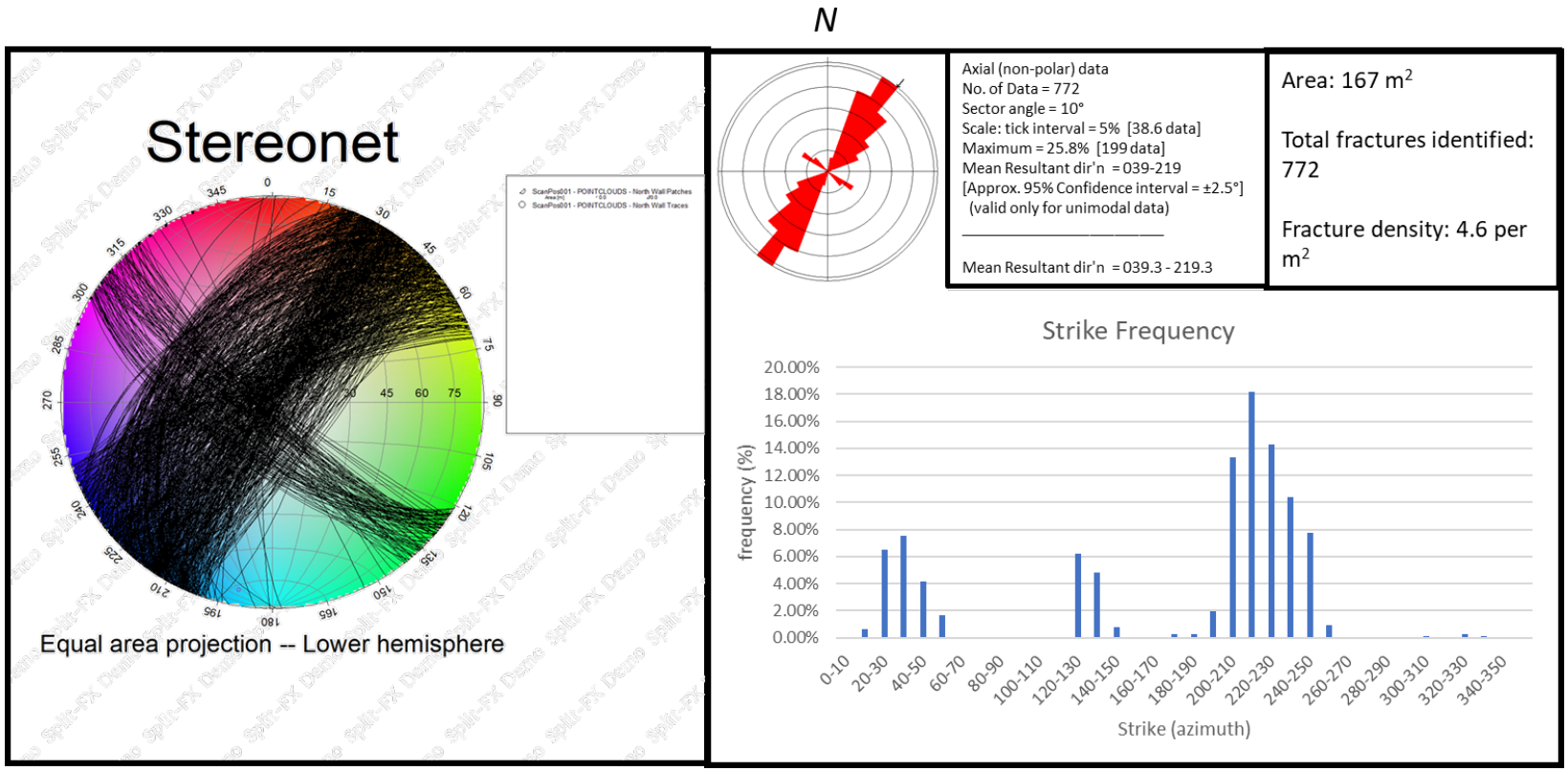

Figure 29: Illustration of strike frequency, rose diagram of data frequency, stereonet representation of fracture great circles, and area observed, total fractures identified, and fracture density per square meter (Holcombe, 2019).

`

5.3.3. Scan Position 3: Bone Spring unconformity

A large, laterally extensive unconformable surface was examined between the 1st Bone Spring Carbonate A and the upper Bone Spring Limestone (transect 8 and tranest 10), with LiDAR reflectance of the interval giving evidence for lithology changes across this surface. Figure 30 illustrates the LiDAR reflective image within Riscan Pro, with reflectance variation indicated by the fluctuation from high reflectance (warm colors) to low reflectance (green). Stratigraphic interpretation within this interval includes the 1st Bone Spring Carbonate A overlain by the Upper Bone Spring limestone at the unconformable surface. Positions above and below the unconformable surface was analyzed, as well as the entirety of the section, analyzed in a position juxtaposed to the area observed in Figure 30. Overall, a 103.82 square meter area analyzed above the unconformity identified 463 fractures, with a dominate NW-SE striking set and a minor hexagonal NE-SW striking set. Fracture density is approximately 4.46 per meter squared. Figure 31 illustrates fracture data collected from Split-FX. Furthermore, large fractures observed within the image appear to terminate at the unconformable surface. This could have significance in the relative chronology of fracture formation. An area of 105.46 square meters was analyzed below the unconformable surface, identifying 92 fractures. Dominate strike frequency changes to NE-SW, with a minor NW-SE hexagonal set present. Figure 32 illustrates fracture data gathered from Split-FX software. Fracture density below the unconformity was observed to be 0.87 per square meter, yielding a substantially lower fracture density than the previously analyzed section positioned above. This low fracture density could be due potentially to a vertical lithology fluctuation, based upon the correlations found in this study. Figure 33 illustrates fracture analysis of both above and below the unconformity.

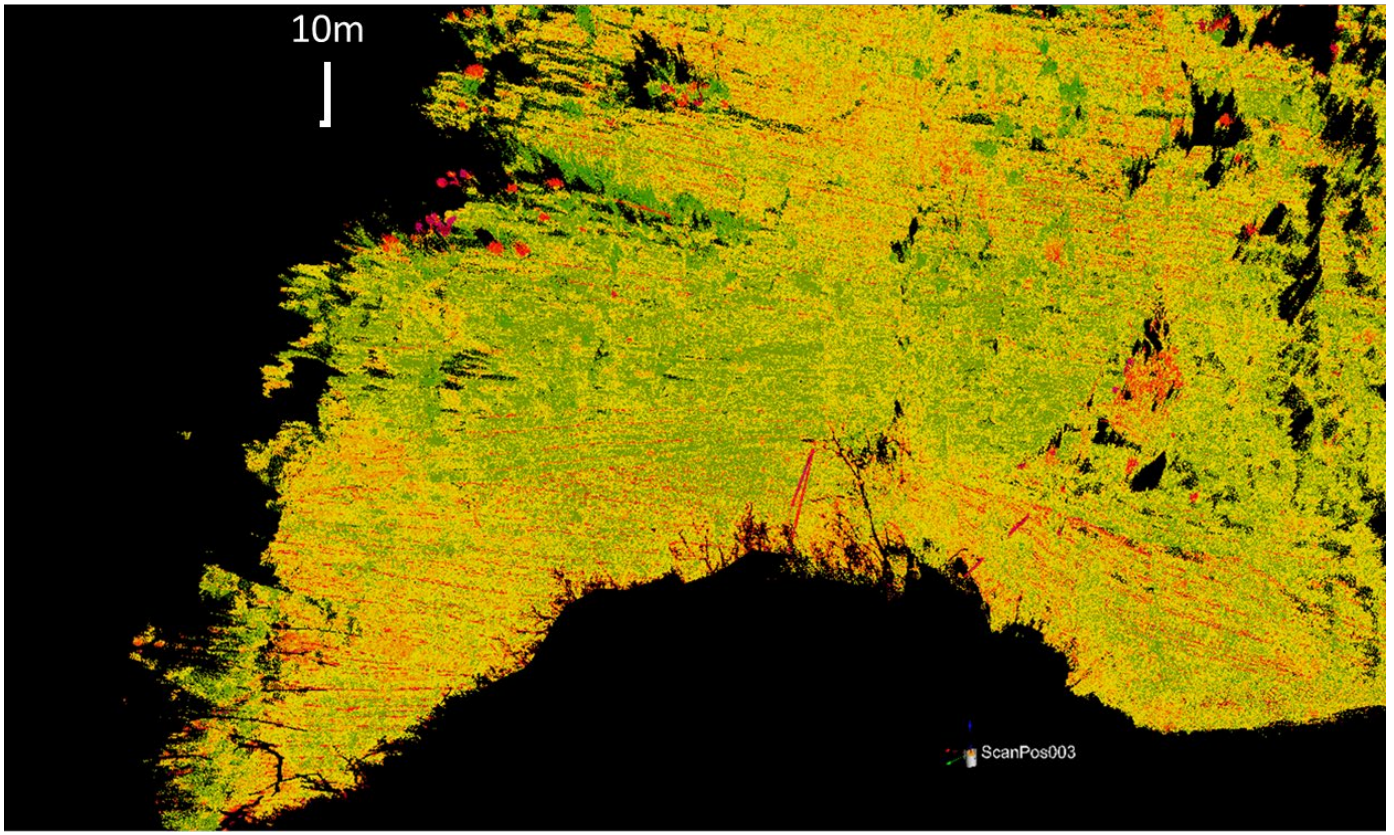

Figure 30: LiDAR reflectance displayed in Riscan Pro. Color change observed in image indicates a variation in point reflectance, indicative of a mineralogy variation (Giddens, 2016)

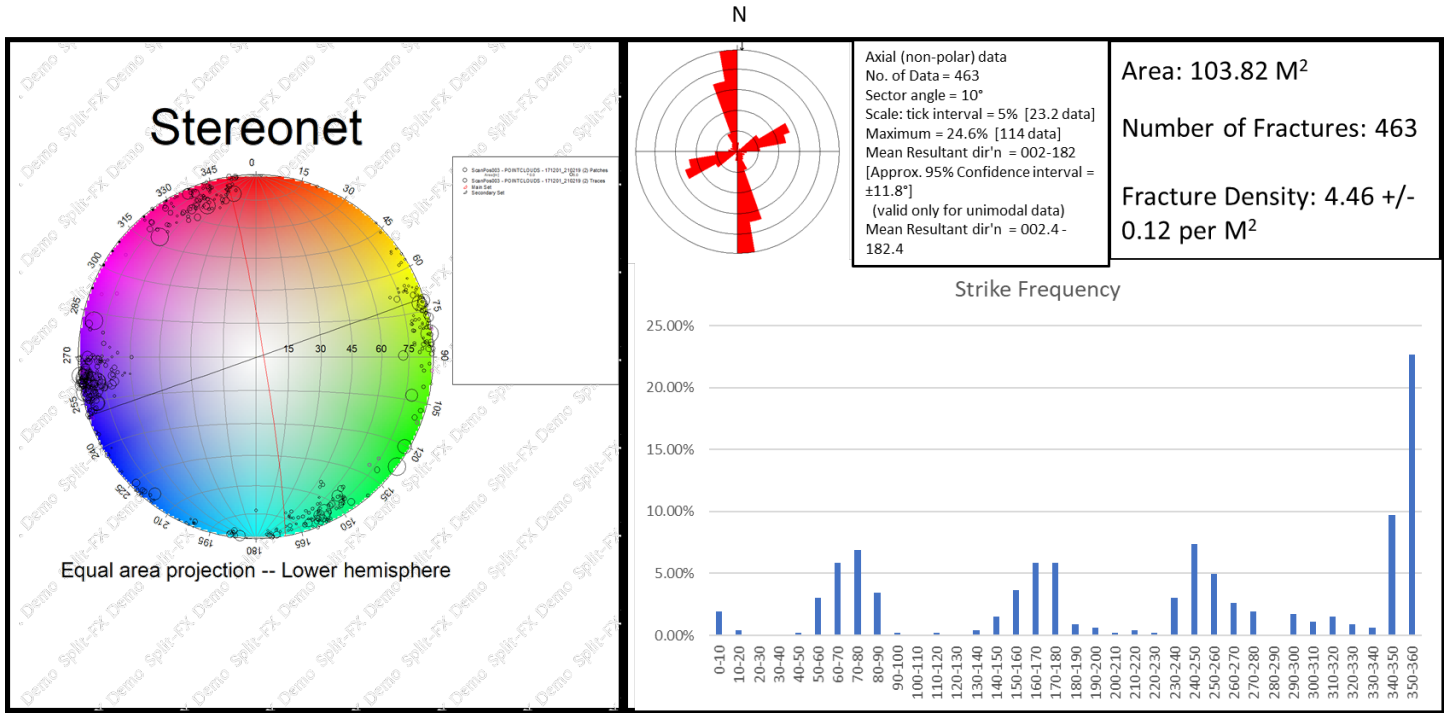

Figure 31: Strike frequency, stereonet view showing set great circles with fracture poles, rose diagram displaying data frequency, with area (m^2), total fractures, and fracture density also displayed above unconformity (Holcombe, 2019).

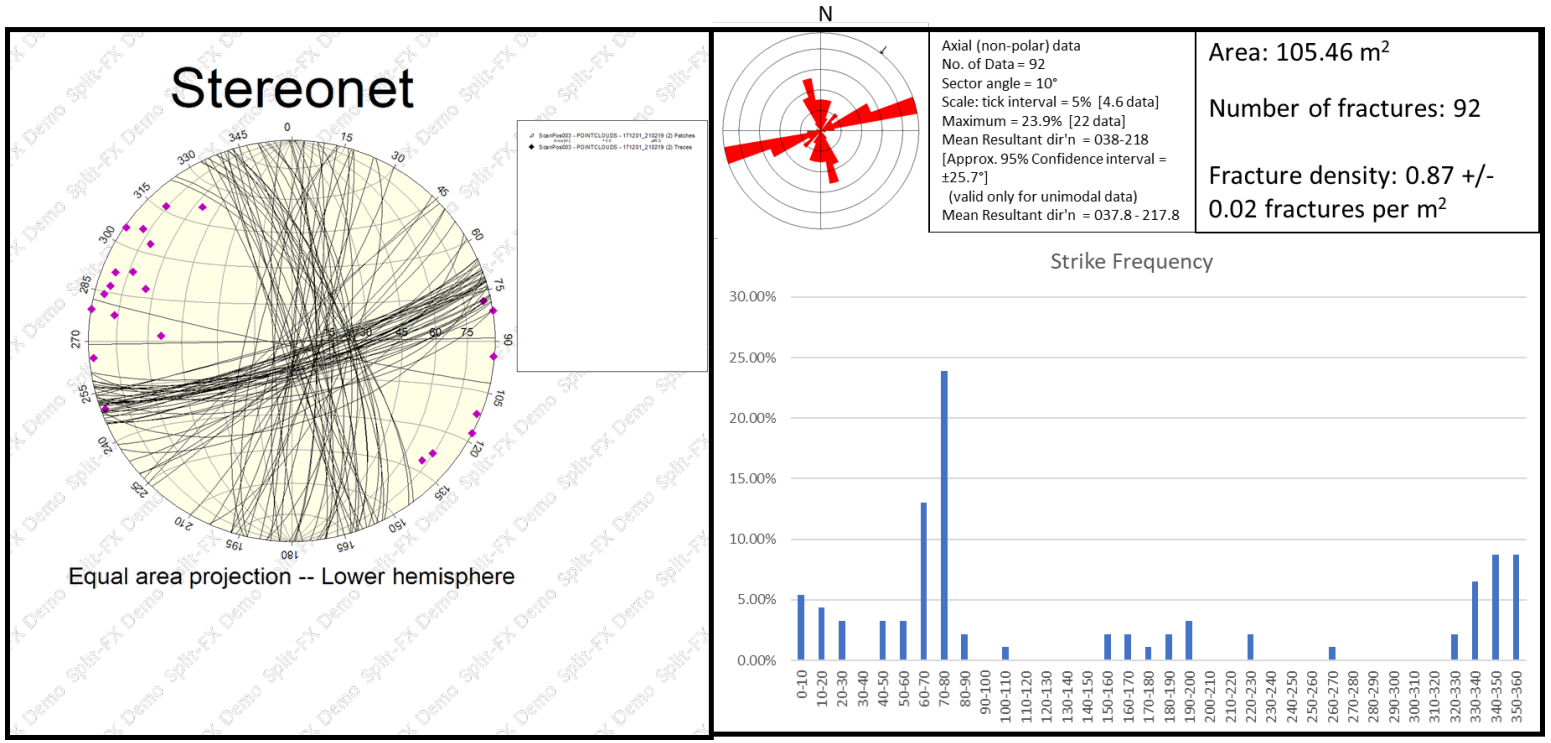

Figure 32: Strike frequency, stereonet view showing trace fracture poles and total fracture great circles, rose diagram displaying data frequency, with area (m^2), total fractures, and fracture density also displayed below unconformity (Holcombe, 2019).

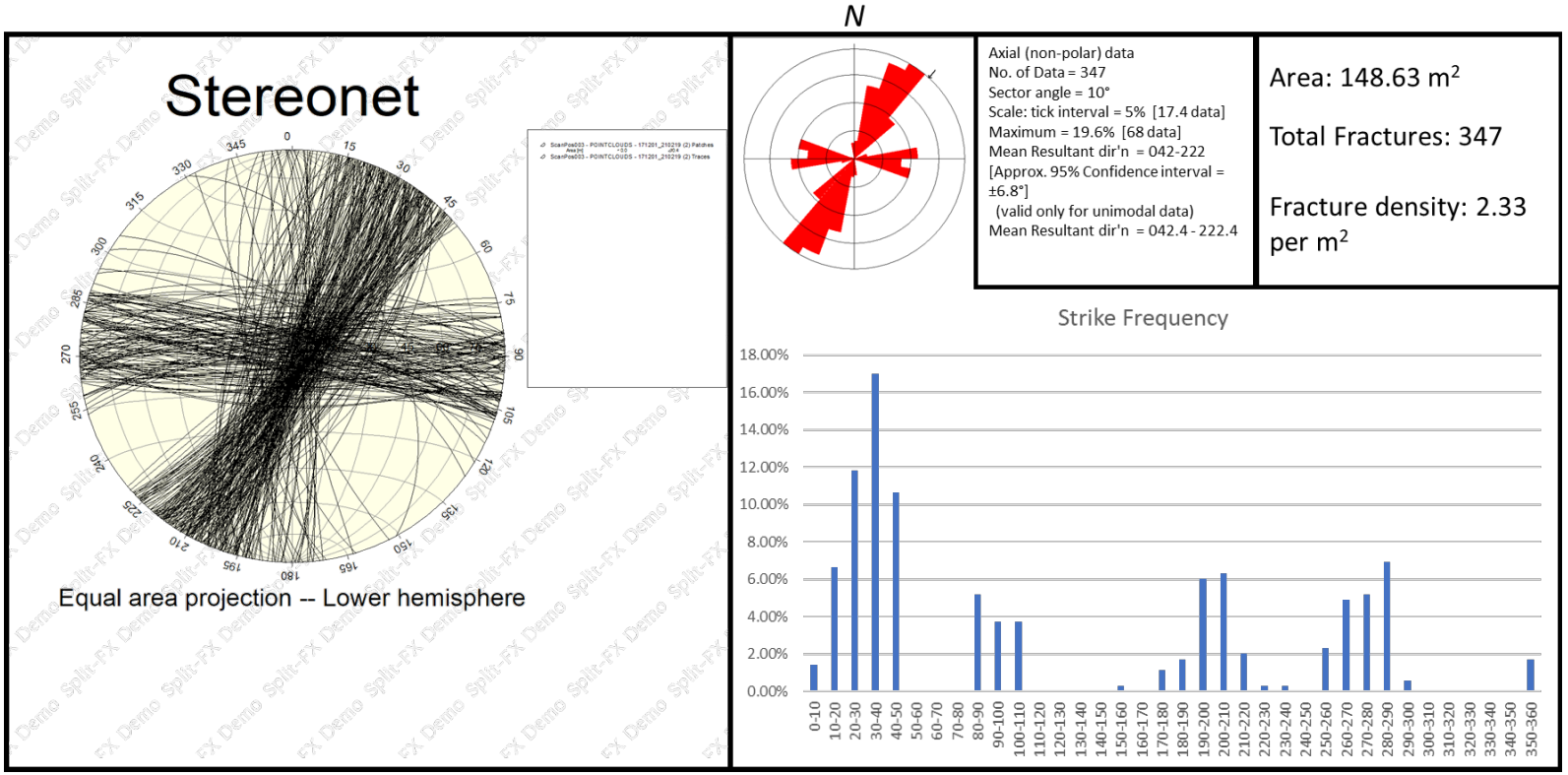

Figure 33: Strike frequency, stereonet view showing set great circles (black and red) with large through fracture poles (blue) and total fracture poles, rose diagram displaying data frequency, with area (m^2), total fractures, and fracture density also displayed for total section (Holcombe, 2019).

`

5.3.4. Transect 7: Bone Spring Carbonate A

Transect 7 consisted of 50 XRF and Schmidt hammer recordings, spanning ~ 400 ft of measured section. Figure 34 illustrates the measuring position of 13 scan locations (red-filled circles) as well as fracture traces identified within the outcrop (magenta planes). In total, 111.99 square meters were analyzed, with 545 fractures identified and multiple sets observed. The area analyzed within Transect 7 lacks the set uniformity which was observed in other positions. This could be a result of mass heterogeneities present within Carbonate A. relative strike direction identified within Transect 7 includes a relative NE-SW trending set, with a minor NW-SE trending minor fracture set. Transect 7 also possesses the highest fracture density of any interval examined, with 4.866 per square meter. This could potentially be due to the finer scan quality, giving the interpreter the ability to identify more fracture traces.

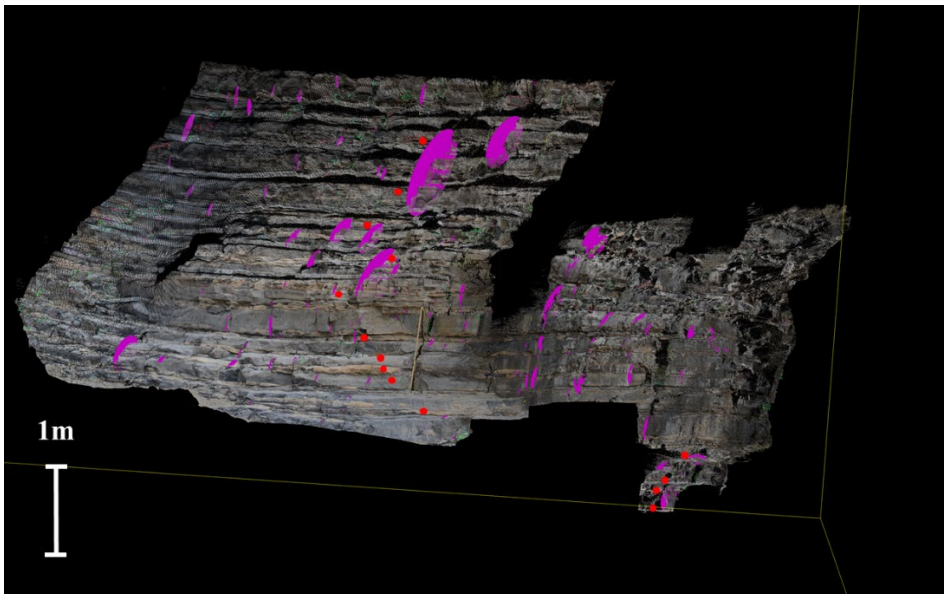

Figure 34: Transect 7 true color scan within Split-FX. Red filled dots show XRD and Schmidt Hammer measuring positions. Magenta planes indicate fracture traces

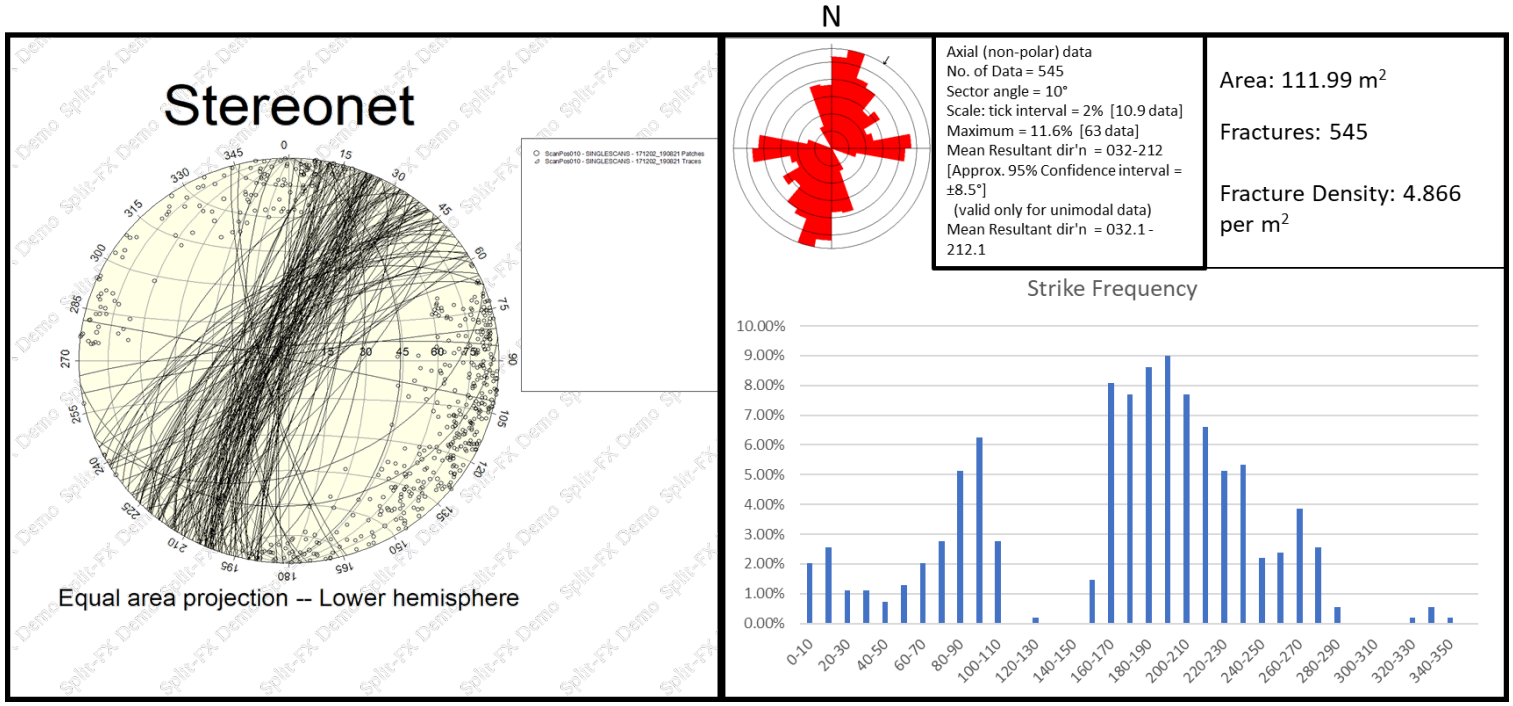

Figure 35: Strike frequency, stereonet view showing total fracture poles and trace fracture great circles, rose diagram displaying data frequency, with area (m^2), total fractures, and fracture density also displayed within the top of Transect 7 (Holcombe, 2019).

`

Figure 35 illustrates fracture data collected from Split-FX rock mass characterization software of transect 7. Figure 36 displays bed truncation in addition to onlapping sediment fill at the base of transect 7, with XRF/Schmidt hammer measurement positions identified through red-filled circles. Overall, the bottom section of Transect 7 shows clearer fracture sets, with strike frequency showing a dominant NW-SE trending set, and a minor, secondary set of hexagonal NE-SW striking fractures. Two fractures were identified which display substantially shallow dips, relative to other sets identified. It is likely that the stress associated with the formation of these individual fractures is unrelated to those forming the dominantly steep sets examined, and likely suggests multiple stress events with varying maximum stress orientations. Figure 37

illustrates fracture data collected from Split-FX, with stereonet view present. Stereonet view present within Figure 37 shows main fracture set (blue) with secondary hexagonal set (red) displayed with trace fracture great circles (black) and total fracture poles. Pole circumference corresponds to relative fracture length. The two great circles seen within stereonet view displaying shallow dip angles corresponds to previously mentioned tertiary set of shallow dipping fractures, however, display similar strike orientations with other fracture traces and the secondary fracture set identified. The observed fracture density for this observed interval is 2.79 per meter squared, with a total examined area of 122.31 meters squared and 342 fractures identified. Figure

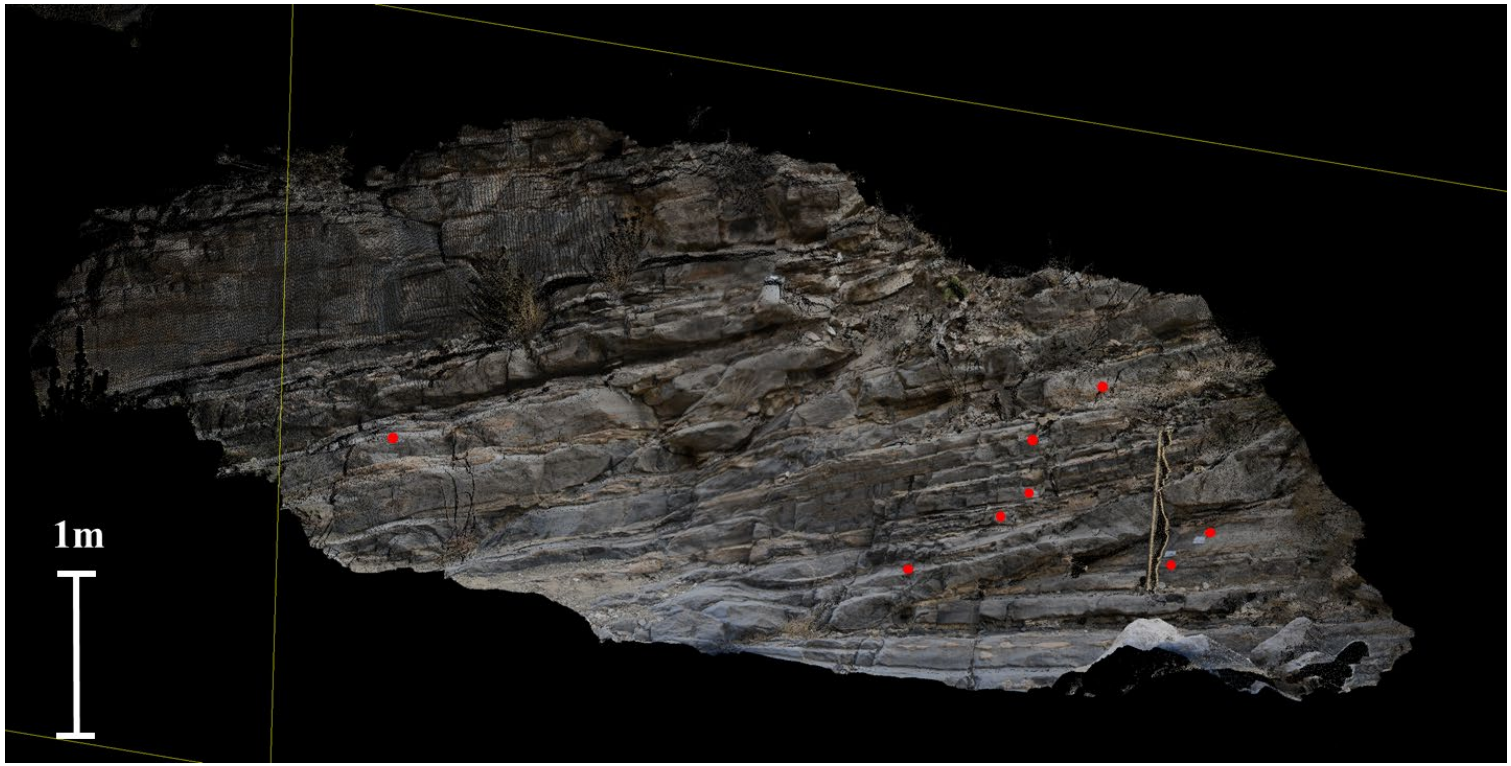

Figure 36: True color point cloud image from Split-FX. Red infilled circles denote XRF/Schmidt Hammer measurement positions 1-7. Unconformity identified above measurement position 2.

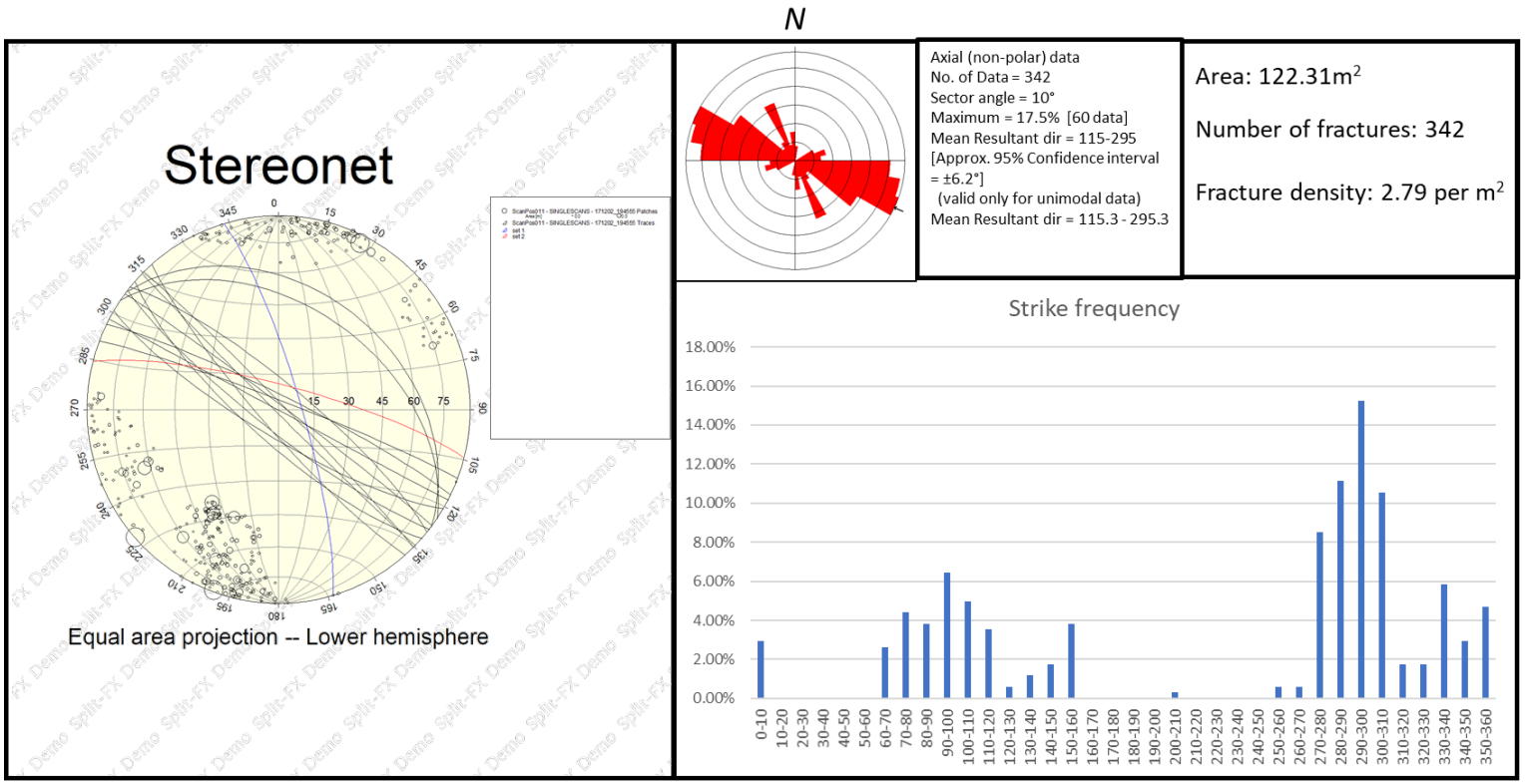

Figure 37: Illustration of fracture data, displaying strike frequency, stereonet view (blue showing main fracture set, red secondary set, black trace fractures), rose diagram of data frequency, area (m^2), total fractures, and fracture density (Holcombe, 2019).

`

5.3.5. Transect 6: Bone Spring Carbonate B

Strike frequencies within Transect 6 (Carbonate B) show a bimodal distribution, with a primary NW-SE trending fracture set and a secondary hexagonal NE-SW trending set. Difference angle between both modes is between 60-70°. Overall, a majority of fractures identified within the 188.41 square meters analyzed show shallow dip, with trace fractures striking approximately N-S. Fracture density observed within this interval show 2.558 per meter squared, with 482 total fractures identified. Highest frequency of fractures occurs at a strike of 120-130°. The reoccurrence of bimodal fracture sets within the Bone Spring Carbonate B could be due to the presence of bedded biogenic chert, as opposed to nodular chert observed within Carbonate A. However, further examination should be done to confirm this interpretation. Figure 38 illustrates the analyzed section. Figure 39 displays Fracture data gathered from Split-FX software.

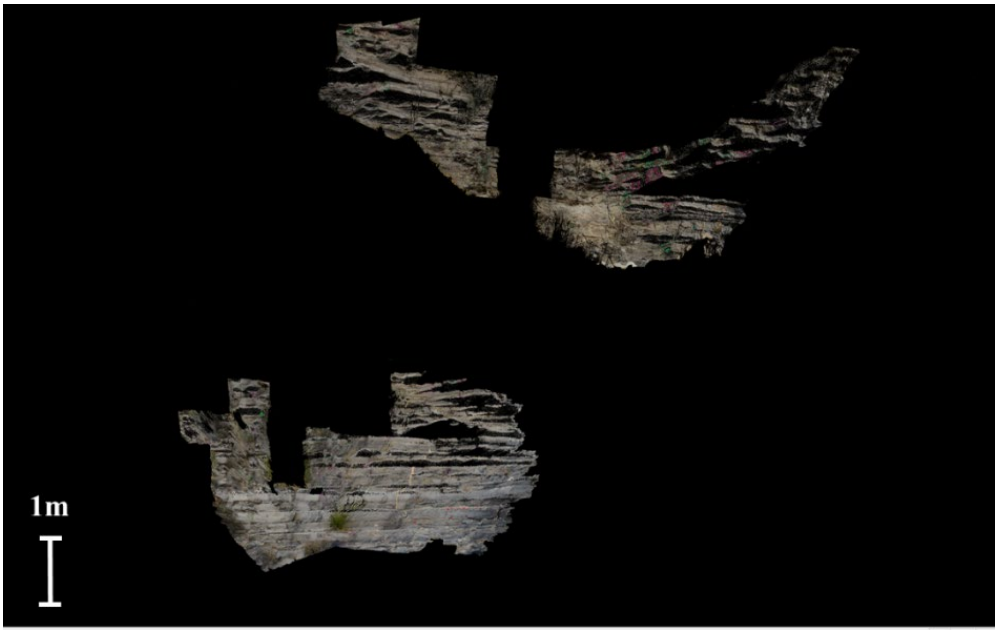

Figure 38: True color point cloud image of transect 6, within the Bone Spring Carbonate B.

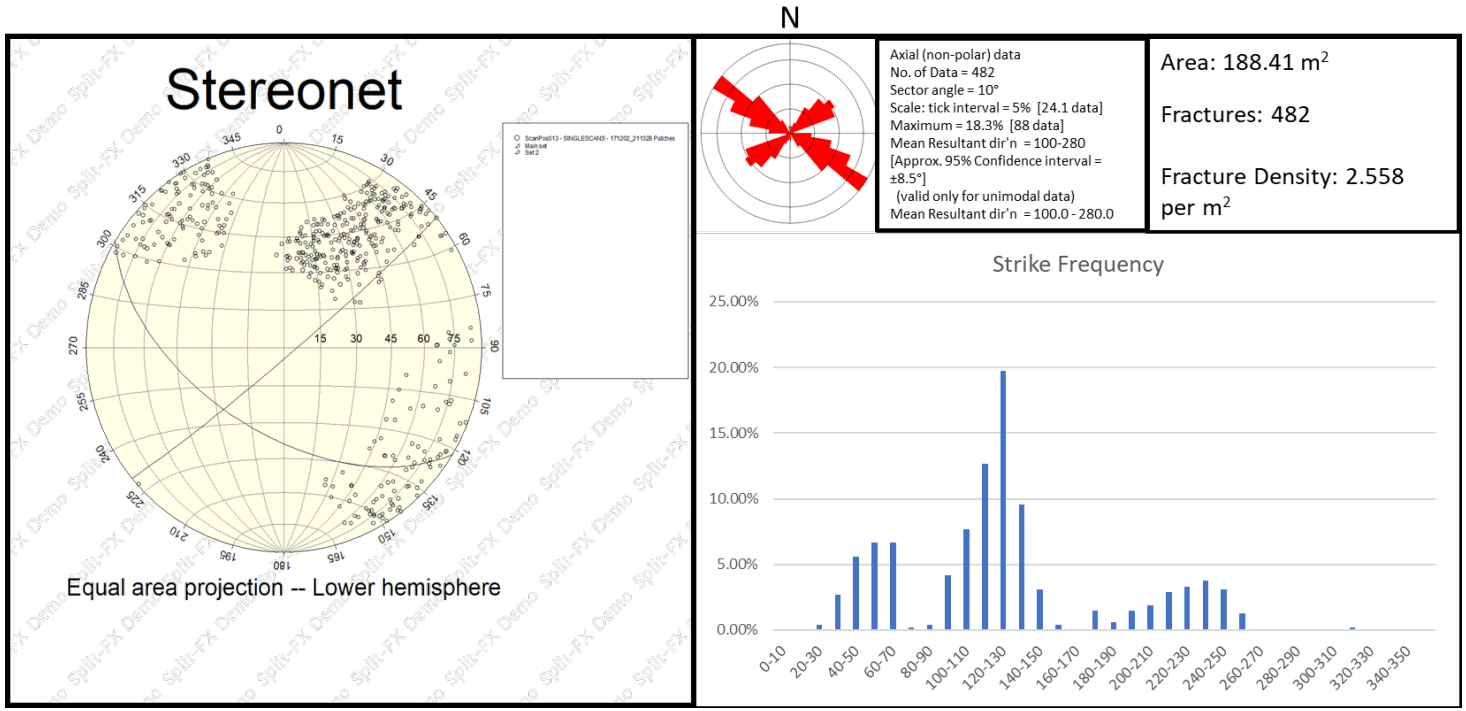

Figure 39: Illustration of fracture data, displaying strike frequency, stereonet view with fracture set great circles, rose diagram of data frequency, area (m^2), total fractures, and fracture density within Bone Spring Carbonate B (Holcombe, 2019).

`

5.3.6. Population Summary

Overall, fracture populations within Bone Canyon show NW-SE and NE-SW trending primary orientations, showing hexagonal sets within carbonate units and orthogonal sets within siliciclastic packages. The coulombic nature of fracture sets analyzed within Carbonate A and B could be indicative of heterogeneity within the 1st Bone Spring Carbonate, and highly isotropic rock mass observed within the cutoff sand channel. An initial interpretation of stratigraphy and fracture orientation frequency data reveals that primary orientations appear to shift above the unconformable surface identified at the top of the 1st Bone Spring Carbonate A and the Upper Bone Spring Limestone. These findings vary with work done by Alabbad (2017), which analyzed E-W orientations within the Brushy Canyon Formation within the Bone Canyon outcrop. Structural dip observed on fractures identified within Transect 6 show shallower dip angles than other intervals analyzed.

5.4. XRF cluster analysis

A statistical cluster analysis was performed on 27 major and trace elements collected from XRF measurements, with rebound values correlated from Q. Cluster analysis includes hierarchal cluster analysis performed on the Minitab statistical program, measuring correlations in fluctuations between rebound values corrections from the SilverSchmidt device to XRF-derived elemental abundances. Rebound values were also analyzed with elemental abundances. Elemental abundances are reported in weight (ppm) while R is a unitless value. The purpose of the statistical cluster analysis was to partition elements in correlation to rock type present within the Bone Canyon outcrop, and to correlate with rebound values. Overall, 6-8 clusters were identified within three individual cluster analysis. Figures 40, 42, and 43 display dendrograms of

`

cluster analysis conducted on transect 1 (1st Bone Spring Carbonate Sand), transect 6 (1st Bone Spring Carbonate B), transect 7 (1st Bone Spring Carbonate A). Overall, rebound values and inferred UCS values show a negative correlation with elements associated with clastic mineralization, including biogenic silica, detrital sedimentation (Cutoff formation), and clays with associated feldspar mineralogy. Figure 41 illustrates defined increases in Ca/Al, with decreases in Zr and Ti within the 1st Bone Spring Carbonate Sand. This further supports the interpretation regarding the presence of biogenic silica, produced during HST time. R values show similarity with elements associated with carbonate deposition. Furthermore, R shows a strong negative relation with Mo, Cu, Ni, U, and V. In Figure 40, transect 1 shows a non-correlation with Cu, Mo and V. Therefore, a x-y cross-plot correlation was applied in order to compare various elemental proxies to Q values, illustrated in figure 41. Displayed in Figure 43, R shows a neutral relation with Cu. The strongest positive elemental correlation seen with R is observed between Barium and Calcium. This infers that R shows highest similarity with high precipitation of dolomite and carbonate content. Uranium and Thorium are absent from cluster analysis of transect 1 due to internal errors within the Thermo Scientific X-Ray Fluorescence measurement device U and Th are present for all other examined intervals.

`

5.4.1. Transect 1 (1st Bone Spring Carbonate Sand)

Figure 40: Dendrogram representing cluster analysis results from elemental abundances and R values from transect 1. Partitions are labeled adjacent to dendrogram.

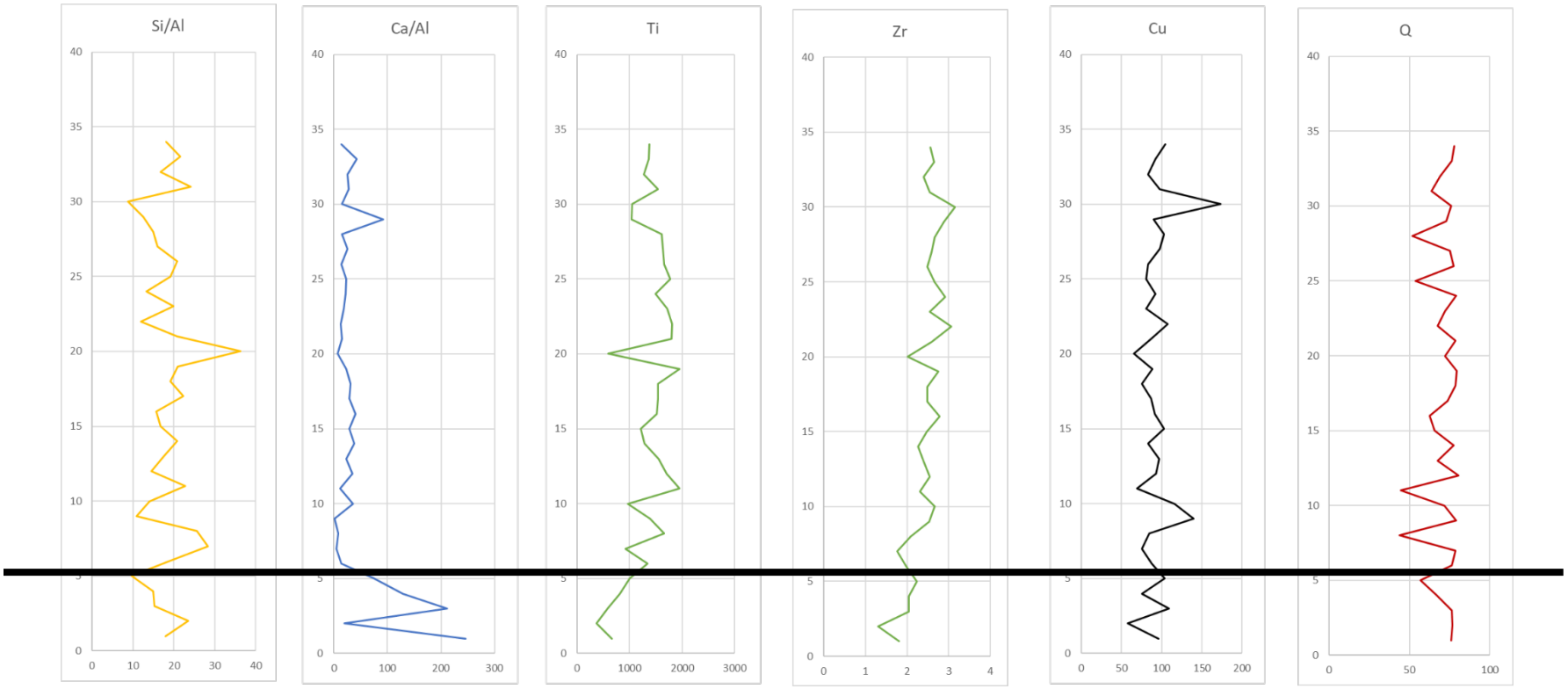

Figure 41: X-Y plots showing Si/Al, Ca/Al, Ti, Zr, Cu, and Q, with black line indicating zone of elevated Ca/Al, with decreased Ti and Zr, indicating possible increase of relative sea level.

5.4.2. Transect 6 (1st Bone Spring Carbonate A)

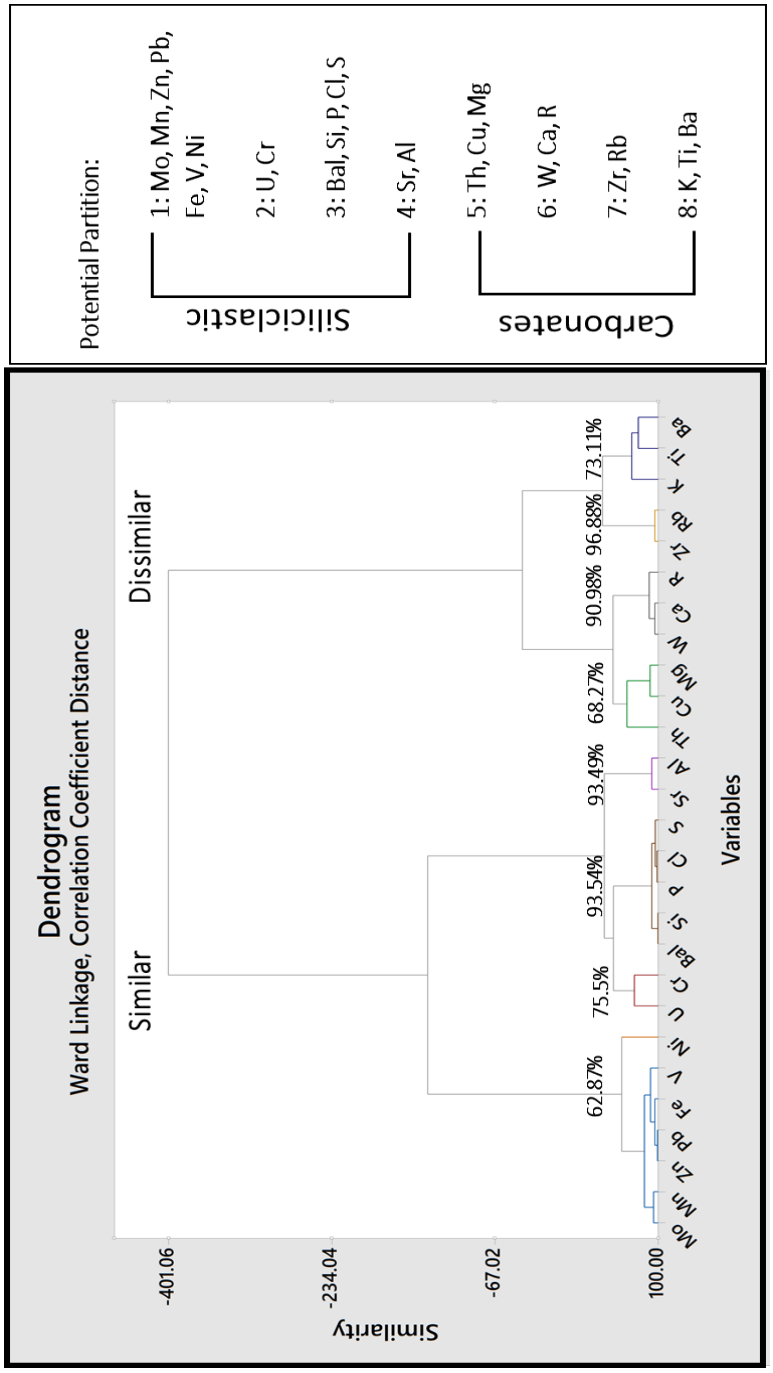

Figure 42: Dendrogram representing cluster analysis results from elemental abundances and R values from transect 6. Partitions are labeled adjacent to dendrogram.

5.4.3. Transect 7 (1st Bone Spring Carbonate B)

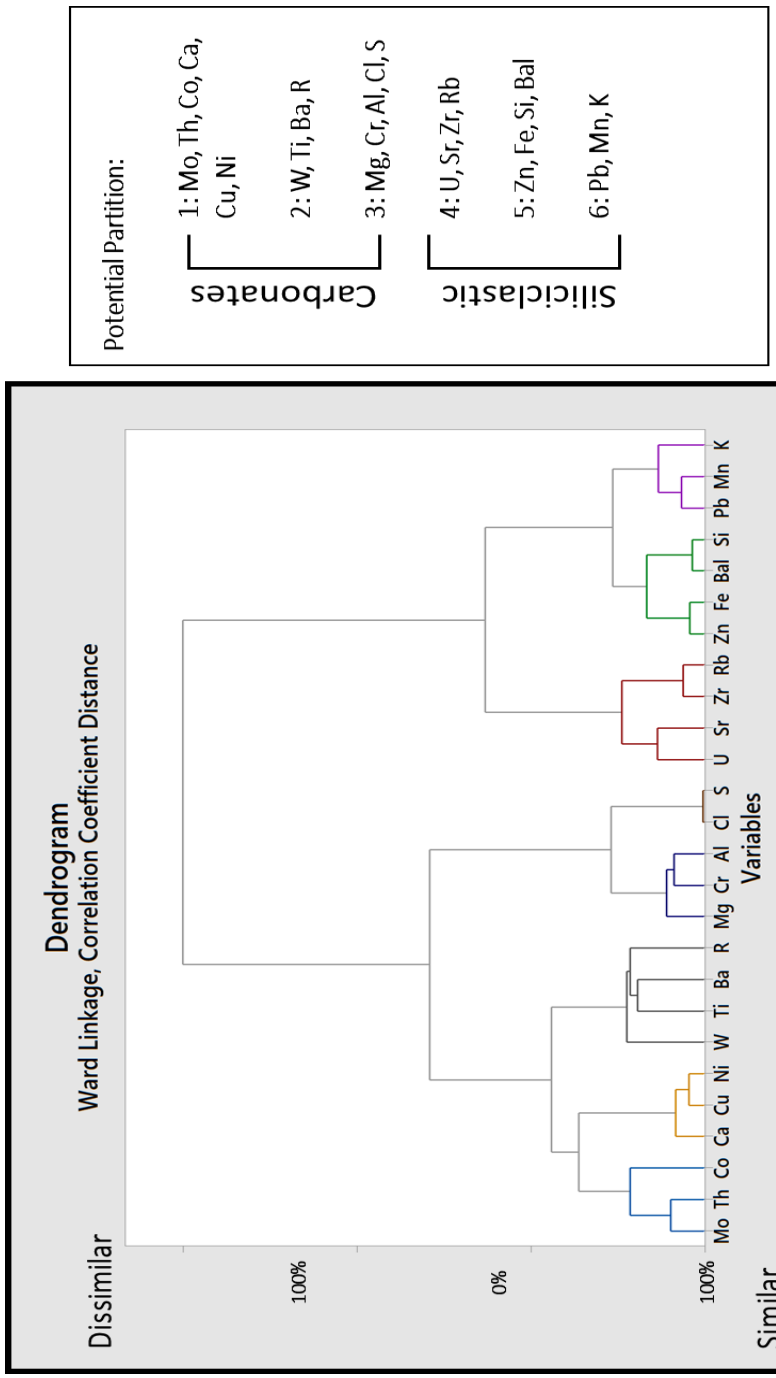

Figure 43: Dendrogram representing cluster analysis results from elemental abundances and R values from transect 7. Partitions are labeled adjacent to dendrogram.

`

5.5. XRF and LiDAR Constrained Lithology

Once statistical analysis was conducted on major and selected trace elements, XRF mineralogy was derived and correlated to LiDAR reflectance. The purpose of correlating XRF mineralogy to point cloud imagery reflectance was to constrain large scale lithology interpretations and confirm precision among interpretations within a multi-facetted geologic framework. In order to clearly and accurately infer mechanical properties and characterize fractures within Bone Canyon, a clear, laterally extensive interpretation of lithofacies is needed. Figures 44 through 47 display LiDAR reflectance of the Bone Spring Carbonate A, Bone Spring Carbonate B, Transect 8 (inferred Bone Spring Limestone), and Cutoff channel sand. LiDAR reflectance is displayed with a pie chart representation of derived XRF mineralogy present at XRF measurements indicated by red arrows.

Higher reflection (>0db) is identified with warm colors (yellow, orange, red), while lower reflectance (<0db) displayed with cooler colors (green, blue, purple). Within charts illustrating XRF mineralogy, purple indicates relative dolomite, blue indicates calcite, red indicates pyrite, brown highlights albite-mica clays, pink indicates potassium feldspar, and light blue indicates gypsum. Figures 46 and 47 show thin section petrographic photographs at approximate collection location. Overall, higher reflection illuminates intervals of large relative silica content, confirmed by mineralogy and petrographic interpretation. Lower reflection corresponds with high calcite precipitation. The attributes which are able to differentiate dolomite from other major mineral abundances such as quartz and calcite could not be observed. Furthermore, no correlation is detected for the presence of clays with LiDAR reflectance.

5.5.1. 1st Bone Spring Carbonate B

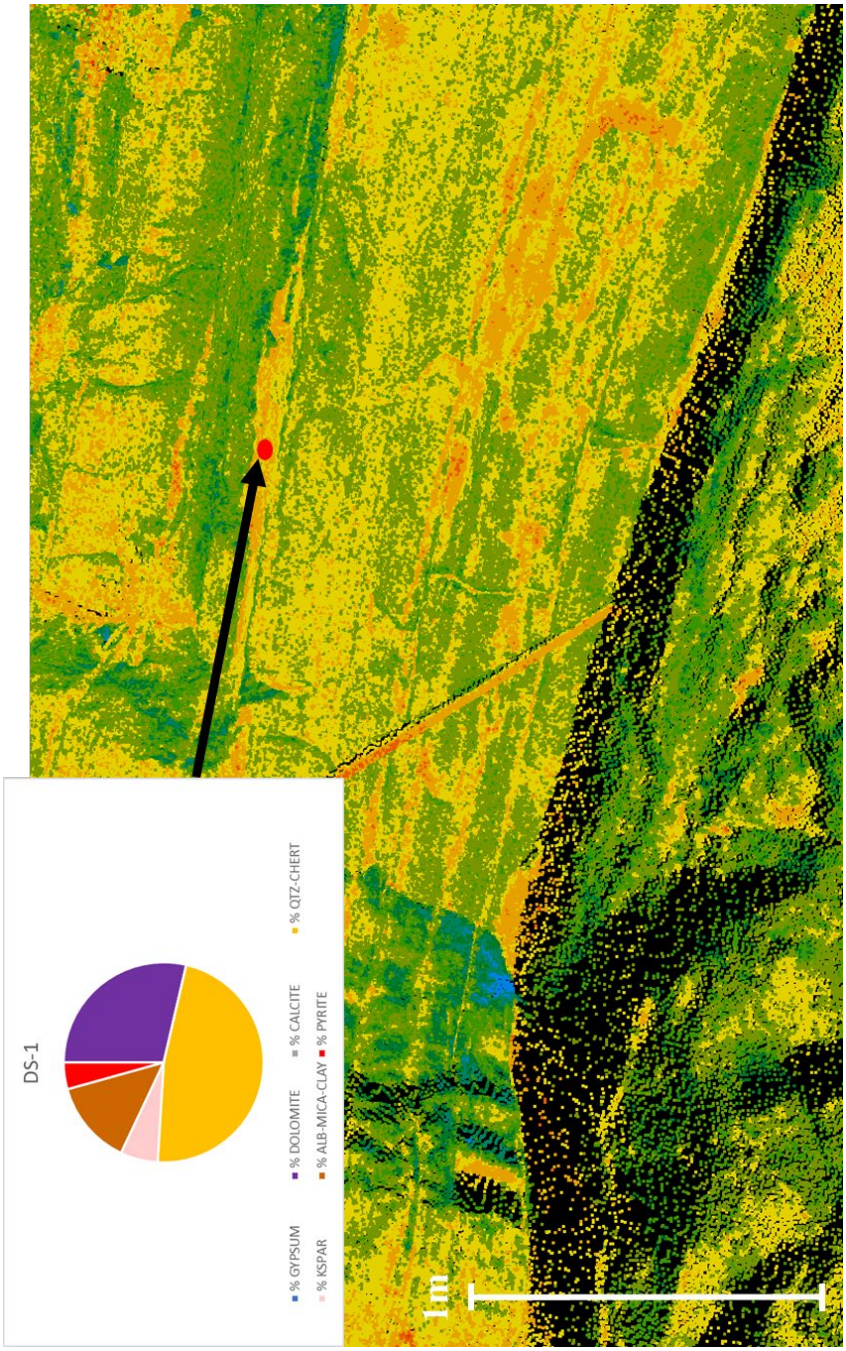

Figure 44: LiDAR reflectance displayed with derived mineralogy. Red filled circle indicates scan position. It should be noted that Transect 4 collected from studies done by Alabbad (2017) align with transect 6 of this study. Therefore, transect 4D was is displayed, as opposed to Transect 6 measurements.

5.5.2. 1st Bone Spring Carbonate A

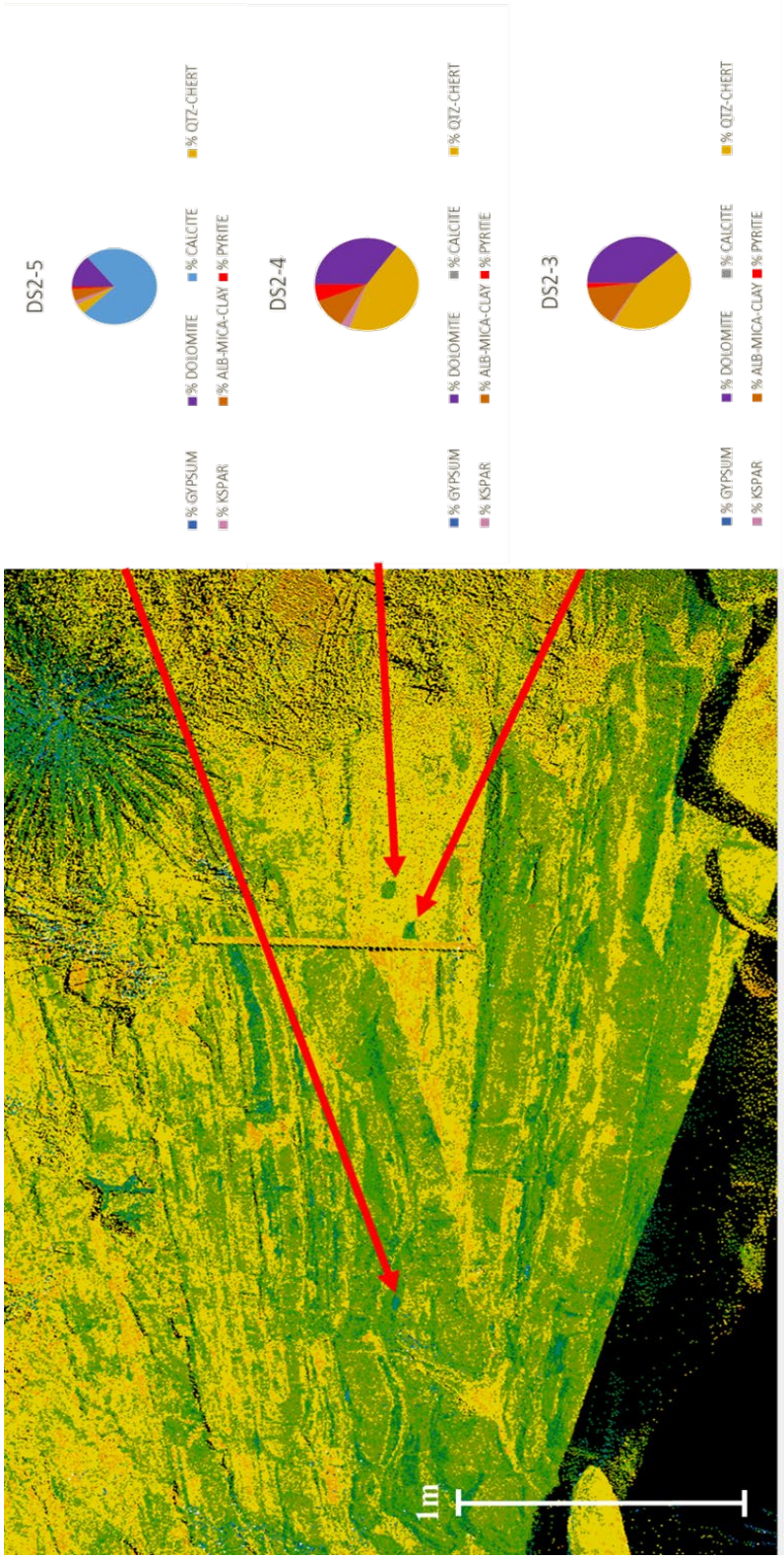

Figure 45: LiDAR reflectance displayed with derived mineralogy. Red filled circle indicates scan position. Measurement positions are 3,4,5.

`

5.5.3. Bone Spring Limestone

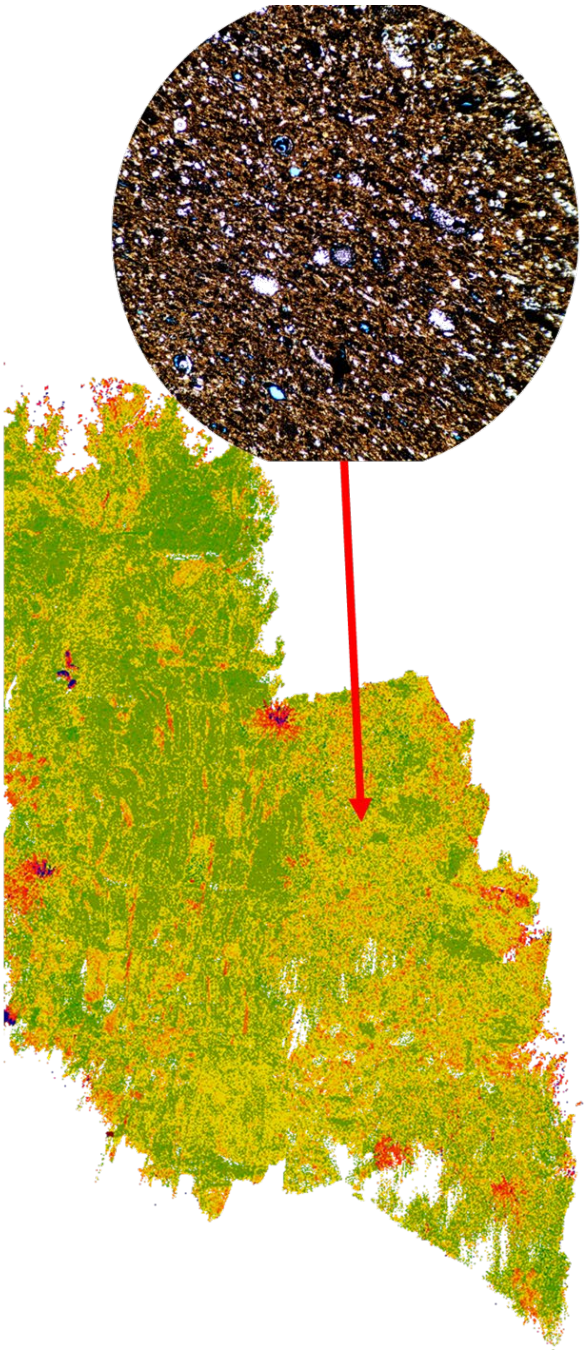

Figure 46: LiDAR reflectance displayed with petrographic slide OU-2161-PMNM. Red arrow indicates relative sample collection location.

5.5.4. Cutoff Channel

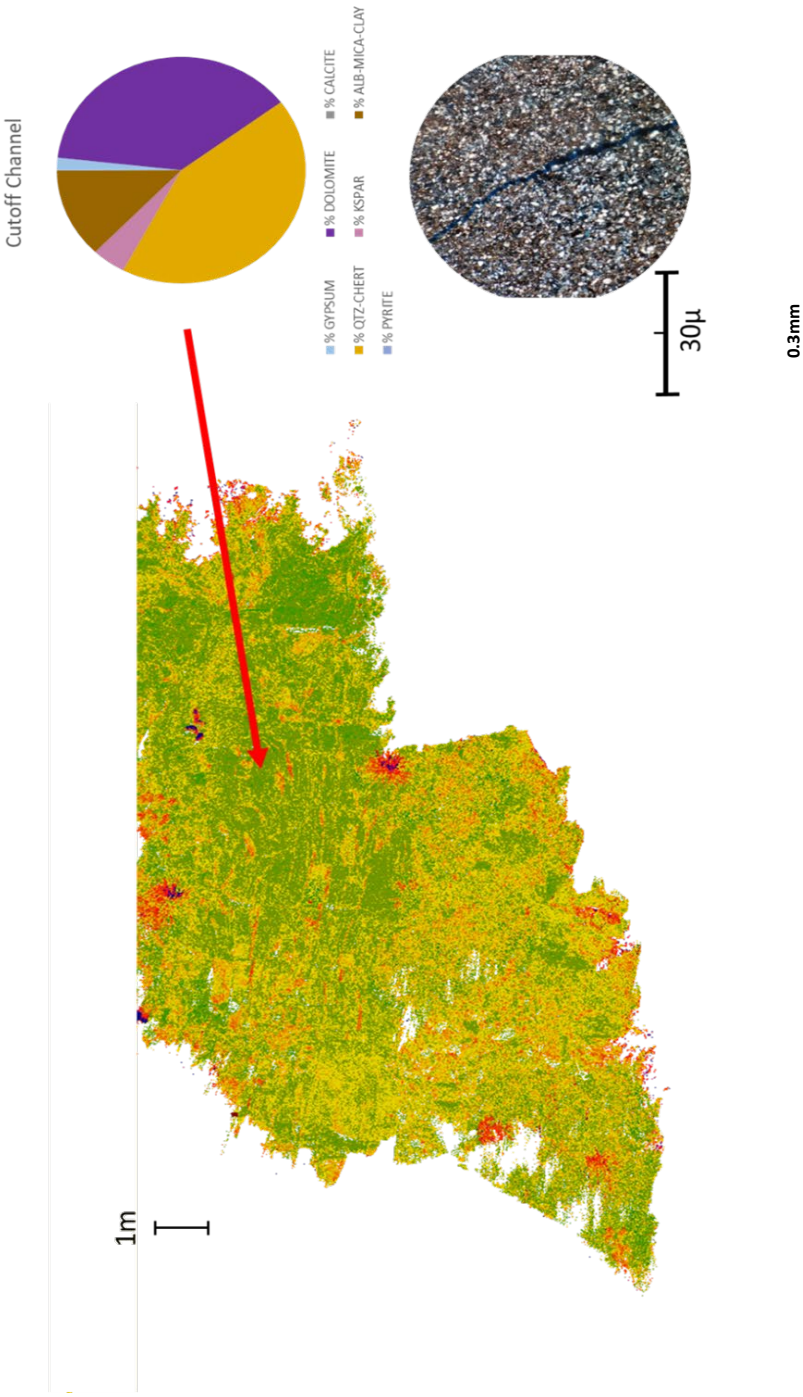

Figure 47: LiDAR reflectance displayed with petrographic slide OU-2132-PMNM, with derived mineralogy. Red arrow indicates relative sample collection location.

`

6. DISCUSSION

6.1. Anoxic/Euxinic proxy correlation

Based upon elemental data and their cluster analysis, correlative positive cluster elements such as Mo, U, V, Ni, Cu can be interpreted to suggest anoxic/euxinic depositional environments that could be associated with high organic content. Studies by Trillovallard et al (2006) concluded that high enrichment of elements such as Mo, Ni, and Cu are correspondent to high TOC enrichment, due to their association with pyrite and sulfur precipitation in organic phases. Within anoxic phases, Ni and Cu are trapped after the decay of organic material within iron sulfides (Trillovallard et al., 2006), which result in a good correlation with TOC. Within this anoxic phase, uptake of associated trace elements is restricted by the presence of compatible organic substrates (Trillovallard et al., 2006). Anoxic proxies which are from Trillavallard et al's study illustrate elements relationships observed with TOC vs Uranium, Nickel, Copper, and Vanadium. Euxinic environmental proxies defined by the relationship between TOC vs Nickel, Uranium, and Molybdenum. Elimination of Uranium and Vanadium as euxinic environmental proxy with TOC is due to U and V association with authigenic phases within euxinic environments. Figure 48 illustrates relationships with elemental proxy's vs TOC. Overall, the purpose of this correlation was to identify positive correlations with high trace element enrichment associated with TOC-rich zones and areas of high rebound intensity. Work done by Verma et al (2017) details relationships with high TOC content, high clay input and plastic deformation among enriched intervals. Research done by Verma et al (2017) has inferred that intervals which possess brittle-ductile couplets (zones identified by high-low strength packages) are the "sweet spot" for high fracability. These zones, defined in the previously mentioned study, appear to be present within the canyon. Though the study by Verma et al characterizes strength

`

couplets with mineralogy-derived strength correlations, correlations with TOC and elastic deformation are well documented (Slatt and Abousleiman, 2011; Verma et al., 2017).

Overall, trends with paleoenvironment elemental proxies have been identified within transects 2-5, 6, and 7. Scatter-plots illustrated in Figure 49 show a significant correlation between Ni and Q, which corresponds to research conducted by Williams et al (2015). Figure 50 displays trace elements Nickel, Copper with XRF-derived mineralogy and R values associated with transect 1. Reducing Vanadium concentration roughly result in decreasing rebound intensity, and vice versa. Likewise, Nickel shows similar correlation with R values. Increases in rebound intensity also seem to correlate slightly with increases in dolomite concentrations. Intervals associated with elevated silica show corresponding decreases in rebound values, as shown in Figure 25.

Figure 50 defines rebound values correlated with XRF derived mineralogy, Nickel and Copper concentrations. It should be noted that, when defined in a statistical analysis, Copper shows a neutral correlation with R values, however in practical use shows high similarities with nickel. Furthermore, for accurate correlation with elemental proxies and R values, weighted average was omitted from this correlation, and mineralogy was correlated on the measured sampling interval. High correlation between Ni, Cu vs R values can be observed, with the exception of intervals encompassing 475ft – 445ft, ~325ft - ~275ft, and ~25ft – 0ft. These findings correspond to previous studies utilizing this method (Williams, 2015; Crowell, 2018). The influx of clay minerals such as kaolinite could explain this variation in R values vs elemental proxies. Initial examinations show further correlations of high-strength intervals and increases in calcite percent. Likewise, an influx in biogenic chert precipitation show decreases in rebound intensity. This could serve to prove further correlations with rock strength and

`

paleoenvironmental interpretations. Trace amounts of gypsum were also identified within the interval 9-10ft. This could serve paleo environmental interpretations of sub-aqueous sedimentation or biogenic silica precipitation.

Transect 7, illustrated in Figure 51, identifies correlations with R values, XRF derived mineralogy, Nickel, and Copper. for accurate correlation with elemental proxies and R values, weighted average was omitted from this correlation, and mineralogy was correlated on the measured sampling interval. Both Nickel and Copper show similarity with R values when examined within a statistical analysis. Overall, like transect 6, fluctuations seem to correspond to variations in elemental proxies and carbonate/chert enrichment. Relatively, decreases in Nickel and Copper concentrations tend to correspond with drops in rebound intensity. Likewise, increases in Nickel and Copper concentrations tend to relate to an increase in R values. Like the comparisons made within transect 6, anomalies within this relationship could be explained through an influx of kaolinite-rich clays, however further examination would be required to confirm this hypothesis. Further research within Bone Canyon could reveal potential correlations with paleo-environment and rebound intensity, through geochemical analysis combined with chemostratigraphy, and highly detailed sequence stratigraphy, combined with subsurface well and seismic correlations.

`

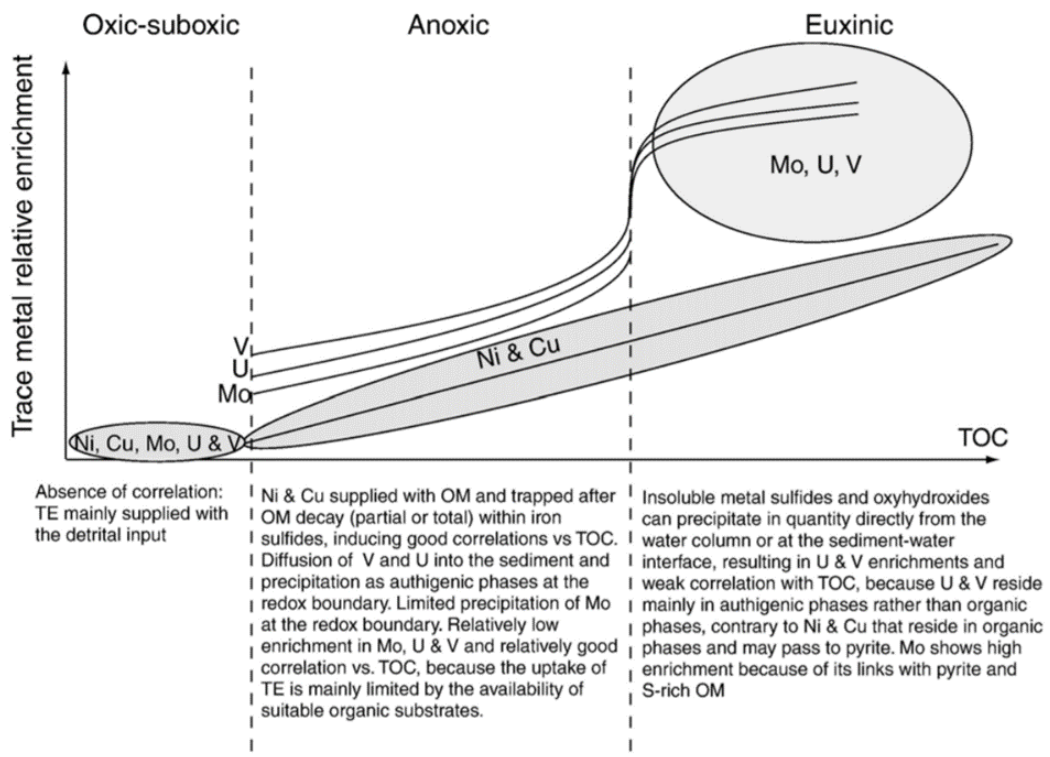

Figure 48: Schematic diagram illustrating the relative enrichment of Ni, Cu, Mo, U and V versus total organic carbon (TOC). TE stands for trace elements and OM stands for organic matter (Trillovallard et al., 2006)

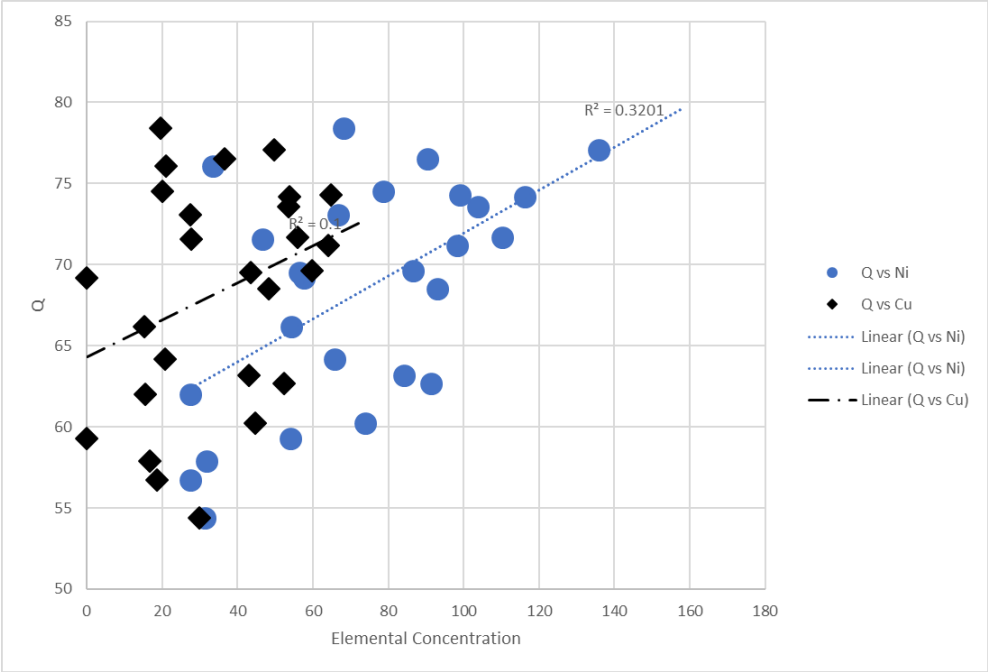

`

Figure 49: 2D scatter-plot view, depicting a substantial correlation between Q and Ni in data points collected from transects 1-10. Q vs Cu show a less substantial correlation. It should be noted that a majority of data points illustrated in figure 49 lie within a mudstone lithology, as opposed to chert.

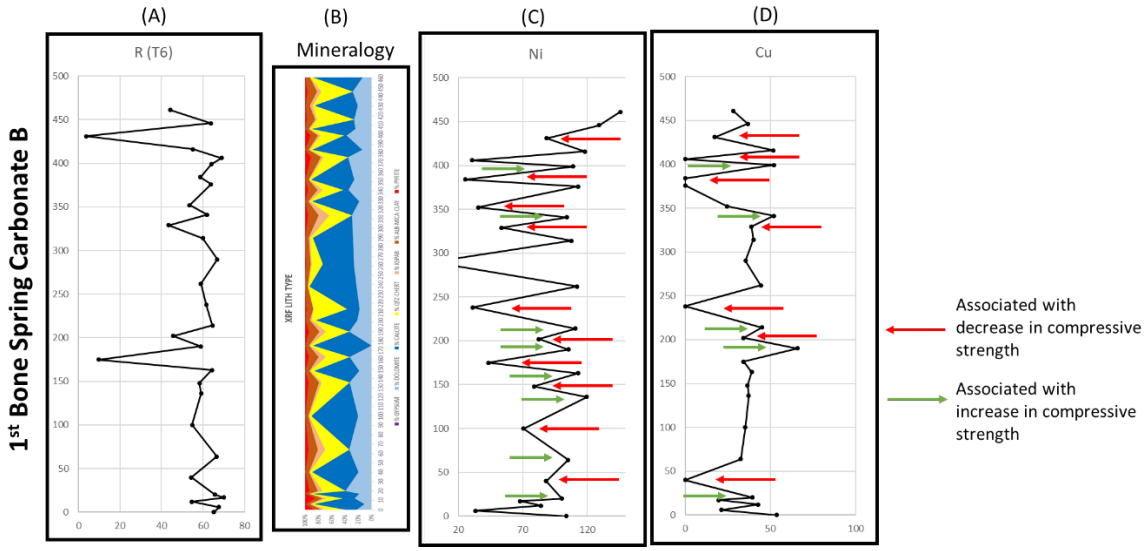

Figure 50: (A) R values derived from SilverSchmidt hardness test, (B) XRF mineralogy in weight percent, (C) nickel concentration in ppm, (D) copper concentration in ppm

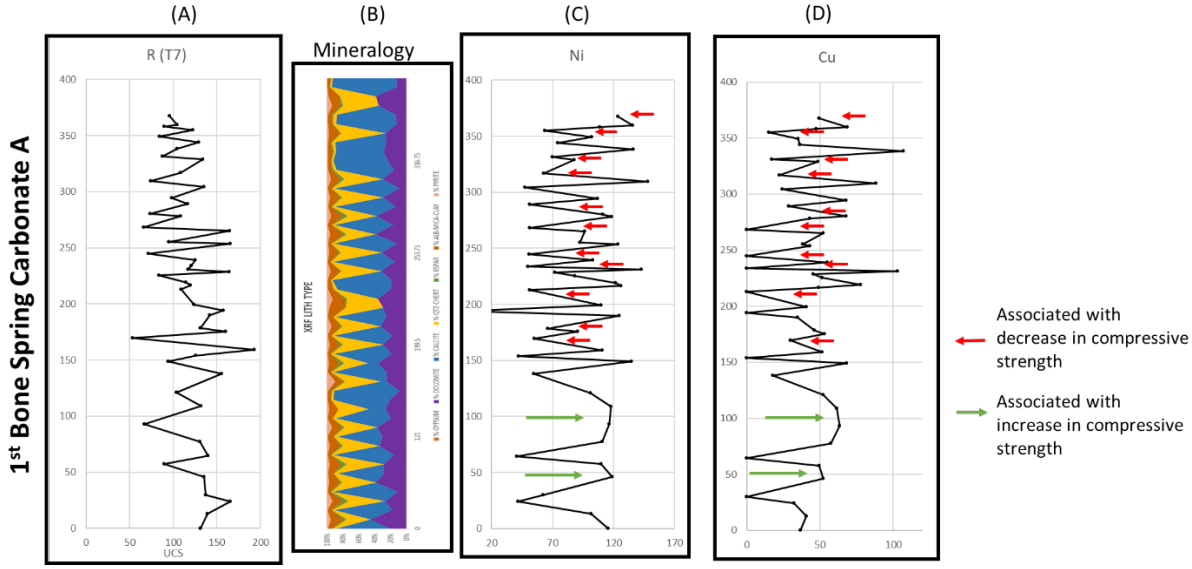

Figure 51: (A) R values from SilverSchmidt hardness test, (B) XRF mineralogy, (C) nickel concentration in ppm, (D) copper concentration in weight percent for Transect 7

`

6.2. Trends in Rebound Hardness

The identification of high-low strength couplets has been identified within the Bone Spring Carbonate, through hardness tests conducted on the measured section within Bone Canyon. Figure 52 illustrates rebound hardness (A) with XRF-derived mineralogy (B). The 1st Bone Spring Carbonate Sand and the 1st Bone Spring Carbonate B are identified to the left, with a sampling interval between 11-28 ft, with a detailed examination of transect 1 on the left, with a 1ft sampling interval. Overall, strength variation with a frequency of 1-2ft exists within a detailed interval, possibly controlled by organic content input and fine-scale paleo-environmental transitions. The accumulation of siliceous radiolarian sponges within the area comprising the Bone canyon during Leonardian time (Pray, 1988) and subsequent precipitation of chert within the upper Bone Spring could be proven as a paleo-driven factor of rebound hardness. Dolomitization of chert intervals also has a significant correlation with rebound hardness, with petrographic examination and XRF-derivation of mineralogy confirming dolomite within the upper Bone Spring. The in-situ production of chert/diagenetic precipitation of dolomite and their relationship with rebound hardness, however, seem to be less significant than paleoenvironment and oxygen input. statistical analysis shows stronger correlations with specific mineralogy precipitation.

It is important to compare bound intensity values with compressive strength tests and fracture toughness examinations, rather than derived associations with mineralogy. Therefore, when attempting to use proxies to correlate rock strength, it is important to interpret paleoenvironmental drivers as opposed to lithology. It is the secondary objective of this study to correlate rock strength to paleo-environmental indicators, with a primary objective to first characterize rock strength within the upper Bone Spring Carbonate. Further work within the

`

canyon on this subject should reveal similar relationships within stratigraphic intervals further within the canyon, such as the Bone Spring Carbonate A, Bone Spring Limestone, and Cutoff formation, though paleo-environmental interpretations should differ within the Bone Spring Limestone and Cutoff Formation.

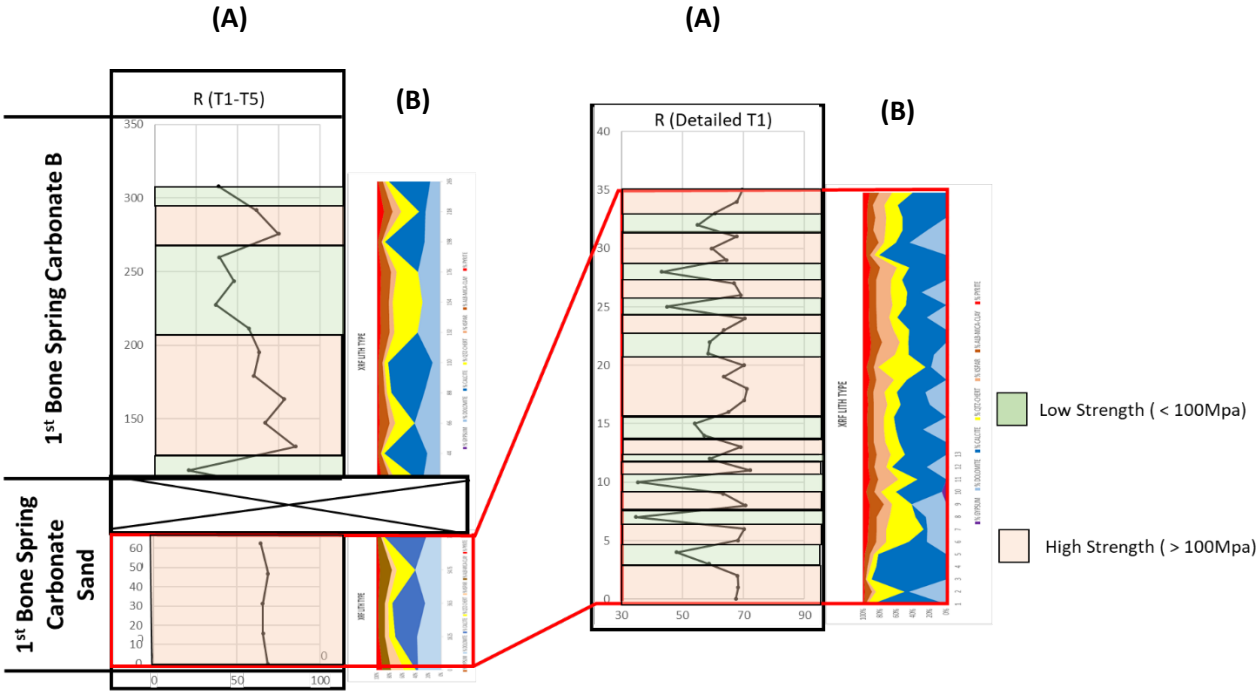

Figure 52: (left) transects 1-5 with (A) Rebound values and (B) XRF-derived mineralogy. (right) defines high-low strength couplets with identical logs views shown. Green shading shows R < 60, Red shading defines intervals where R > 60

6.3. Fracture Characterization

6.3.1. Fracture Orientation Distribution

The distribution of fracture orientations within the canyon can be observed within Figure 52, defining a proposed 2D strength model, constrained by canyon stratigraphy and determined through uniaxial strength testing of the measured section within the canyon. Overall, intervals

`

examined within the Cutoff show primary fracture orientations with a NE-SW strike, and a secondary NW-SE set. This varies from the NW-SE primary set which the majority of the Bone Spring Carbonate B examined intervals possess. There is also evidence suggesting the termination of large, NW striking fractures by an unconformable surface examined at scan position 3. NE striking fractures also examined proximal to scan position 3 are observed to permeate through this unconformity. It is possible that this unconformity examined at scan position 3 could correspond to a large unconformity examined within Shummard Canyon adjacent to Bone Canyon. The confirmation of relative age of this unconformable surface could lead to the age dating of associated stress events in Bone Canyon. Fracture traces, although partially interpreted from LiDAR imagery, were not able to be extracted using Split-FX, due to a failure of the mesh to define a fracture plane.

The curvature of the canyon wall may apply a bias to collected data and affect the ability to identify continuous fractures within the outcrop (Alabbad, 2017) from LiDAR. The orientation of Bone Canyon outcrop has been defined by Alabbad (2017) to have a curvilinear orientation (south wall, brushy canyon formation) with a dominant orientation of NW-SE. The curvilinear nature of the outcrop could prevent identification of fractures within the upper Bone Canyon. Therefore, interpretation bias should be considered for NW-SE orientations. Further examination of fracture orientations within the canyon should focus on LiDAR imagery and fracture characterization of the lower Bone Canyon, encompassing the lower Carbonate B and 1st Bone Carbonate Sand. The inference of fracture density and orientations within the lower interval are dominantly NW-SE fracture orientations with increased fracture density and average bed thickness similar to Carbonate B. This inference is based upon field observations, XRF sampling

`

and Schmidt Hammer rebound hardness testing. However, this information should be confirmed through LiDAR imagery.

6.3.2. Distribution of fracture density and bed thickness

In total, 3,407 fractures were identified within the upper section of the 1st Bone Spring Carbonate. Fracture density and average bed thickness within the canyon show an inverse relationship, with an increase of average bed thickness showing a decrease in fracture density. This is comparable to findings by McGinnis (2017). Likewise, decrease in average bed thickness reveals an increase in fracture density. Figure 53 illustrates the relationship between fracture density and average bed thickness (left track). From correlations with average bed thickness, fracture density, and rebound values, fracture density appears to become elevated where rebound values are low. According to the set standards (International Association of Engineering Geologists), (International Society for Rock Mechanics), and (geological society), R values measured from the Bone Spring outcrop represent strong rock (<50 geological society and IAEG, <60 ISRM), with varying degrees of rock hardness (Sajid & Arif, 2015). Intervals which show moderate to soft rock (>50) values include the Cutoff channel sand, Bone Spring Carbonate B, and the 1st Bone Spring Carbonate Sand. However, within the 1st Bone Spring Carbonate Sand, 1ft-scale strength couplets are prevalent, with values ranging from ~5 (weak) to 80 (extremely strong) (Sajid & Arif, 2015). These fine-scale fluctuations in organic rich, hard shale and soft, siliceous material make for ideal targets for hydraulic fracture stimulation (Verma et al., 2017).

Figure 54 defines an inverse relationship between average bedding thickness and fracture density measured in Split-FX. Also displayed, a logarithmic correlation with R^2=0.7201 (R^2=0.4042 when fracture density below unconformity is included)

6.3.3. 2D rock strength model

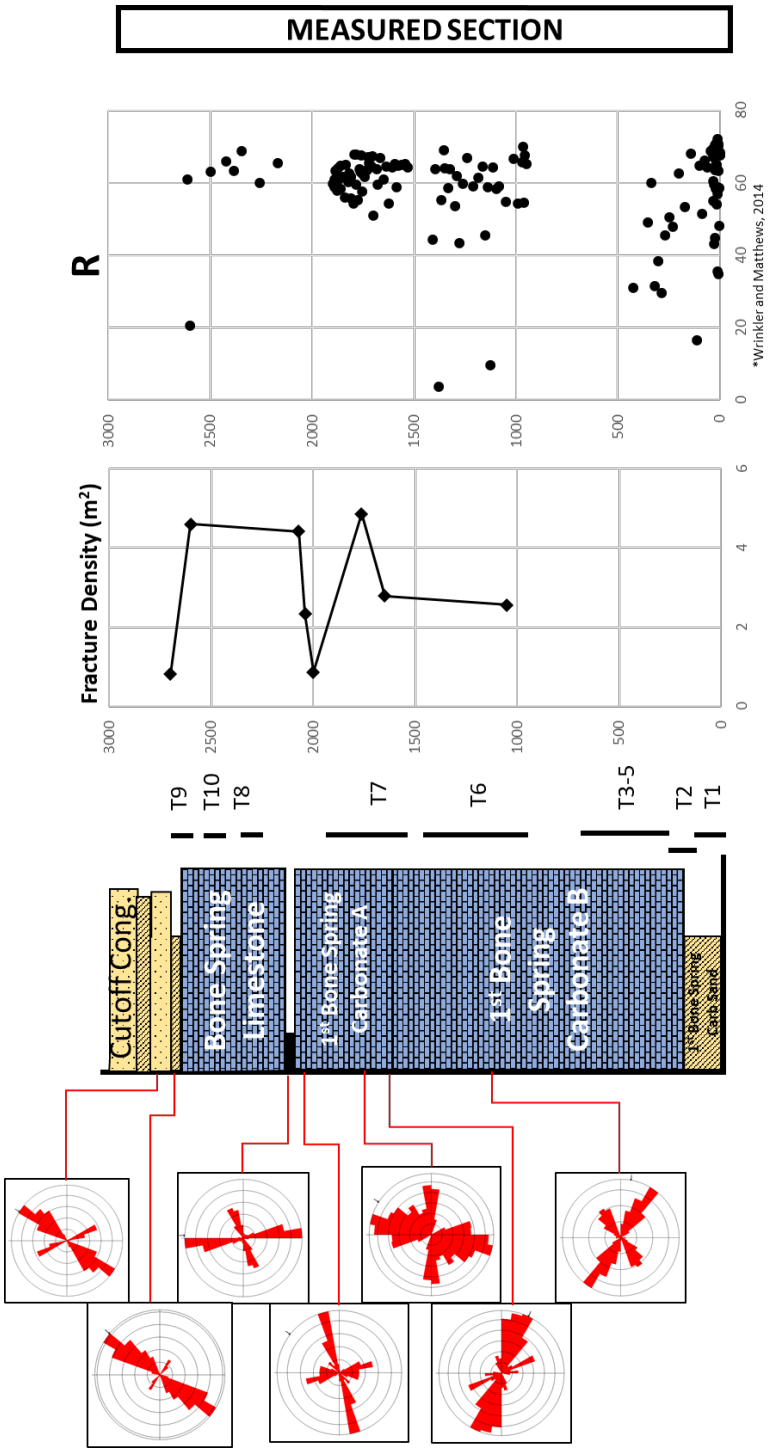

Figure 53: stratigraphic column identifying relative stratigraphy, (middle) log view plotting fracture density, (right) rebound values derived from Q (Mpa). Measured transects are also identified in their approximate stratigraphic positions, adjacent to the stratigraphic column. Measured section recorded in ft.

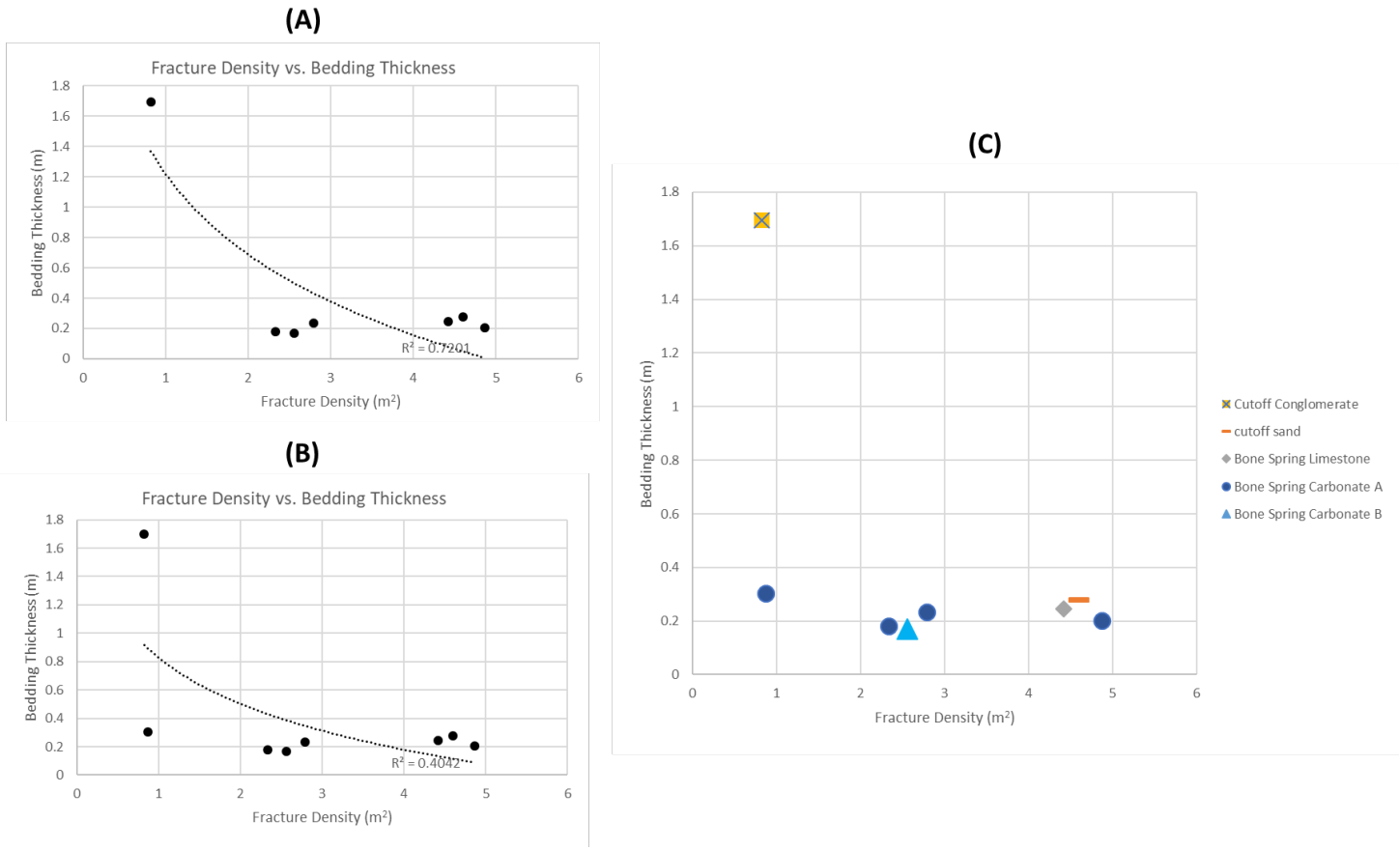

Figure 54: (A) X-Y plot illustrating a strong negative logarithmic correlation between fracture density and average bed thickness, minus the addition of fracture densities measured below the Bone Spring unconformity. (B) highlights identical correlation, with the addition of fracture densities measured at the Bone Spring unconformity. Note substantial decrease in R^2. (C) fracture density vs. average bed thickness separated by lithology.

`

6.4. Implications for Future Work

The findings of this study should be considered preliminary, with a need for further study regarding compressive strength testing. Strength inference based on triaxial compressive strength tests to would be able to varify correlations with Schmidt hammer data within the interpretted stratigraphic framework. Though UCS can be utilized for the recognition of strength properties to relate with the rock, factors such as fracture toughness can provide more relevant information (Bai, 2016). Furthermore, the verification of fine-scale high/low strength couplets within the measured intervals of the Cutoff channel sand, Cutoff formation, Bone Spring Limestone, Bone Spring Carbonate A and Bone Spring Carbonate B is necessary for identification of intervals with geomechanical properties ideal for hydraulic fracturing. Mechanical data from outcrop also should be correlated with subsurface well data, such as interpretive lithology models, dipole sonic logs, seismic data, DAS, DTS, microseismic, and relative correlation to conventional well logs in order to varify mechanical properties within the subsurface. It should be noted that the effects of weathering could eliminate fracture surfaces within outcrop, and therefore fracture densities could be elevated within the subsurface, compared to this study.

Though evidence of biogenic silica exists within the interval identified as the 1st Bone Spring Carbonate Sand, further chemostratigraphic analysis and biostratigraphy should be implemented to confirm the subdivision of the Bone Spring within Bone Canyon. Furthermore, the implementation of mechanical stratigraphy within the canyon to subsurface would not only support the geomechanical data inferred from the Bone Spring outcrop but would also serve to support stratigraphic interpretations made utilizing LiDAR imagery, satellite imagery, and XRF-derived mineralogy correlations. Likewise, geochemical analysis (for example, TOC analysis) of the Bone Spring outcrop could support proxy correlations with other factors defined in this

`

study. (Trillovollard et al., 2006). These results would allow the comparison of TOC data with uniaxial and triaxial compressive tests.

Idealistically, correlation of fracture orientations and dip information gathered from Bone Canyon correlated to subsurface image logs, such as formation imaging or borehole imaging, would support the data inferred in this study. Furthermore, the differentiation of sealed and open fractures would further support fracture characterization within the 1st Bone Spring Formation. Combined with horizontal fluctuations of fracture length and density, the definition of open and sealed fractures within the canyon can also give an integrated fracture characterization of the 1st Bone Spring Carbonate within Bone Canyon. Furthermore, initial observations from this study suggests fracture fill between the 1st Bone Spring Carbonate and the 1st Bone Spring Carbonate A are different, where chert cementation being dominant within Carbonate A. These findings would suggest a diagenetic influence. Correlation of this research and work done by Alabbad (2017) indicate vast fluctuations of fractures orientations and density. The confirmation of Alabbad's work would give insight into mechanical information within the Brushy Canyon Formation. Furthermore, the collection of density data could give insight into velocity properties within Bone Canyon and could be compared with velocity correlations derived from this study, using a common Poisson's ratio.

`

7. CONCLUSIONS

Results from this study supports the presence of fine-scale fluctuations in rock hardness within the lower interval up the upper Bone Spring formation, on the magnitude of 1-2ft. Results also suggest that anoxic/euxinic proxies indicative of a high TOC concentration can assist in the identification of fine-scale rock hardness fluctuations. A positive correlation of rebound hardness and high TOC paleo-environmental proxies can aid in the interpretation of high-low strength couplets within the 1st Bone Spring Carbonate. The lithological variations, although a factor, were observed to have less significance to variations in rock hardness than fluctuations in oxygen with paleo-time. Areas defined by low rebound measurements show a substantial correlation with areas of increased fracture density. The presence of an inverse relation with average bed thickness and R values also exists. The highest fracture densites measured within the canyon are observed within the Cutoff channel sand and the 1st Bone Spring Carbonate A. This correlates with rebound values recorded within these intervals.

The presence of bimodal strike frequency peaks in fracture data, within various measurement locations within the Bone Spring outcrop supports the identification of primary and secondary fracture sets. This is coupled with the identification of formation permeating fractures. Preliminary interpretation from this study supports the occurrence of stress events creating NW-SE fractures, followed by varying maximum stress direction events supporting the creation of NE-SW trending fracture sets. Further research would heighten the understanding of mechanical stratigraphy and characterized fractures included within these findings.

`

The Main conclusions identified from this study are as follows:

- Primary fracture orientations within the upper Bone Spring include a NW-SE trending primary set in the Bone Spring Limestone, and 1st Bone Spring Carbonate B, with a hexagonal NE-SW trending secondary set. Primary orientations are identified as dominantly NE-SE in the interbedded Chert-Mudstone Carbonate A.
- The highest fracture densities are observed within the 1st Bone Spring Carbonate interval A and the Cutoff channel. An inverse correlation was observed with bedding thickness and fracture density.
- Anoxic/Euxinic proxies show a substantial positive correlation with rebound hardness in transect 6 (1st Bone Spring Carbonate B) and transect 7 (1st Bone Spring Carbonate A). Positive correlations were also observed with dolomite volume vs Q and quartz volume vs Q
- Fine-scale (1ft scale) hardness fluctuations have been interpreted within the 1st Bone Spring Carbonate Sand. Further research could verify the relations of hardness and rock strength within the canyon.

`

REFERENCES

Adams, John Emery, et al. "Starved Pennsylvanian Midland Basin." *AAPG Bulletin* 35.12 (1951): 2600-2607.

Adams, John Emery. "Stratigraphic-tectonic development of Delaware Basin." *AAPG Bulletin* 49.11 (1965): 2140-2148.

Alabbad, Abdullah. "Outcrop-Scale Study Of The Permian Bone Spring Formation, Bone Spring Canyon, Guadalupe Mountains, Texas: Fracture Characterization." 2017

Amani, Ali, and Khalil Shahbazi. "Prediction of Rock Strength Using Drilling Data and Sonic Logs." *International Journal of Computer Applications*, vol. 81, no. 2, 2013, pp. 5–10., doi:10.5120/13982-1986.

Bachmann, Joseph, Philip Stuart, Brian Corales, Blake Fernandez, Peter Kissel, Holly Stewart, David Amoss, Blaise Angelico, Alonso Guerra-Garcia, K. Blake Hancock, Richard Roberts, and Bill Sanchez, 2014, The "New" Horizontal Permian Basin.

Bai, Mao "Why are brittleness and fracability not equivalent in designing hydraulic fracturing in tight shale gas reservoirs" *Petroleum*. Vol.2, issue 1. March 2016.

Beaubouef, R.T., Rossen C., Zelt F.B., Sulivan, M.D., Mohrig, D.C., Jennette G. Field Guide for AAPG Hedberg Field Research Conference – April 15-20, 1999: *Deep-Water Sandstones, Brushy Canyon Formation, West Texas*

Çelik, Sefer Beran, and Ibrahim Çobanoğlu. "Estimation of Uniaxial Compressive Strength from Point Load Strength, Schmidt Hardness and P-Wave Velocity." *SpringerLink*, Springer-Verlag, 15 May 2008,

Crosby, C. B., 2015, Depositional history and high resolution sequence stratigraphy of the Leonardian Bone Spring Formation, Northern Delaware Basin, Eddy and Lea Counties, New Mexico: Norman, OK, University of Oklahoma.

Colwell, Christopher L. "CORRELATION OF CHEMOSTRATIGRAPHY, MECHANICAL STRATIGRAPHY, AND TOTAL ORGANIC CARBON USING ONE CORE FROM THE BARNETT SHALE, FORT WORTH BASIN, HOOD COUNTY, TEXAS." *Home*, 1 Jan. 2018

Davis, Marshall D, and Marshall Dewayne. "Petroleum Geology Of The Leonardian Age, Harkey Mills Sandstone: A New Horizontal Target In The Permian Bone Spring Formation, Eddy And Lea Counties, Southeast New Mexico." *ResearchCommons Home*, Geology, 1 Jan. 2014, rc.library.uta.edu/uta-ir/handle/10106/24900.

Denison, R. E., Burke, W. H. Jr., Hetherington, E. A., Jr., and Otto, J.B., 1969, Basement rock framework of parts of Texas, southern New Mexico, and northern Mexico, in The

`

Geologic Framework of the Chihuahua Tectonic Belt, West Texas Geological Society, Publication 71-59, p. 3-14.

Denison, R. E., Kenny, G. S., Burke, W. H. Jr., and Hetherington, E. A., Jr., 1971, Isotopic ages of igneous and metamorphic boulders from the Haymond Formation (Pennsylvanian), Marathon Basin, Texas and their significance: Geological Society of America Bulletin, v. 80, p. 245-256.

Droege, Lauren. "Bone Spring: A Sleeping Giant." *IHS Markit*, 16 May 2018, ihsmarkit.com/research-analysis/Bone-spring-a-sleeping-giant.html.

Dumas, D. B., 1980, Seismicity in the Basin and Range province of Texas and northeastern Chihuahua, Mexico: in Dickerson, P. W., and Hoffer, J. M., (editors), Trans-Pecos Region, New Mexico Geological Society Guidebook, 31st Field Conference, p. 77-81

Galley, John E. "Oil and geology in the Permian basin of Texas and New Mexico: North America." (1958): 395-446.

Gawloski, T.F., 1987 "Nature, distribution, and petroleum potential of the Bone Spring detrital sediments, northern Delaware Basin: Mitchell Energy Corporation Publication, p. 44-69.

Ghazban, 2010 "Hydrocarbon-induced diagenetic dolomite and pyrite formation associated with the hormoz island salt dome, offshore iran"

Giddens, Emma, John D. Pigott, and Kulwadee L. Pigott. "Pleistocene Coral Reef Destruction in the Florida Keys: Paleotempestite Evidence from a High- Resolution LIDAR XRF Analysis of Windley Key Quarry." Sea 100 (2016):120

Goetz, L. K., 1980, Quaternary faulting in the Salt Basin Graben: in Dickerson, P. W., and Hoffer, J. M., (editors), Trans-Pecos Region: New Mexico Geological Society, Guidebook 31st Field Conference, p. 83-92.

Hanzel, J. E., 2014, Lidar-based fracture characterization: an outcrop-scale study of the Woodford Shale, McAlister Shale Pit, Oklahoma, Masterâ€™s thesis, Oklahoma State University, Stillwater, Oklahoma, 72 p.

Hart, B.S., 1998, New Insights on the Stratigraphy and Production Characteristics of the Bone Spring Formation: West Texas Geological Society Publication, v. 98-105, p. 119-126.

Holcombe, Rod. *GEOrient: Stereographic Projection and Rose Diagram Plotting Application - Rod Holcombe Structural Geology Software & Tools*, www.holcombe.net.au/software/georient.html.

Holt, R. M., Fjaer, E., Nes, O. M., & Alassi, H. T. (2011, January 1). A Shaly Look At Brittleness. American Rock Mechanics Association.

Hill, C. A., 1996 Geology of the Delaware Basin, Guadalupe, Apache, and Glass Mountains, New Mexico and West Texas: SEPM Publication, no. 96-39.

Hills, J.m., 1984, Sedimentation, Tectonism, and Hydrocarbon Generation in Delaware Basin, West Texas and Southeastern New Mexico: AAPG Bulletin, v. 68.3, p. 250-267.

`

Hornbuckle, John S "Process Sedimentology of the Guadalupian Rader Limestone, Delaware Basin" *The University of Oklahoma*, 2017

Katz, O., Z. Reches, and J-C. Roegiers. "Evaluation of mechanical rock properties using a Schmidt Hammer." International Journal of Rock Mechanics and Mining Sciences 37, no. 4 (2000): 723-728

Keller, G. R., Veldhuis, J. H., and Powers, D. W., 1983, An analysis of gravity and magnetic anomalies in the Diablo Plateau area: in Roberts, M., (editor), Geology of the Sierra Diablo and Southern Hueco Mountains, Texas: Society of Economic Paleontologists and Mineralogists - Permian Basin Section, Field Conference Guidebook, p. 152-165.

King, Philip Burke. *Geology of the southern Guadalupe Mountains, Texas*. Vol. 215. US Government Printing Office, 1948.

Kullman, John Aaron "Fracture Networks and Fault Zone Features in a Deep-Water Sandstone, Brushy Canyon Formation, West Texas." *Proquest* (1999)

Mazzullo, S. J., and A. M. Reid, 1987, Basinal Lower Permian facies, Permian Basin: Part II depositional setting and reservoir facies of Wolfcampian – Lower Leonardian basinal carbonates: West Texas Geological Society Bulletin, v. 26, p. 5-10. McGinnis, R. N., D. A. Ferrill, A. P. Morris, K. J. Smart, and D. Lehrmann, 2017, Mechanical stratigraphic controls on natural fracture spacing and penetration: Journal of Structural Geology, v. 95, p. 160–170,

Moreland, Travis. "Catastrophic Process Event Stratigraphy of the Rader Member in the Delaware Basin." *Catastrophic Process Event Stratigraphy of the Rader Member in the Delaware Basin*, 13 Dec. 2018, shareok.org/handle/11244/316774.

Montgomery, S.L., 1997, Permian Bone Spring Formation: Sandstone Play in the Delaware Basin, Part II-Basin: AAPG Bulletin, v. 81.9, p. 1423-1434.

Montgomery, S.L., 1997, Permian Bone Spring Formation: Sandstone Play in the Delaware Basin Part I-Slope: AAPG Bulletin, v. 81.8, p. 1239-1258.

Muehlberger, W.R., and Dickerson, P.W., 1989, Structure and stratigraphy of Trans-Pecos Texas: El Paso to Guadalupe Mountains and Big Bend Guidebook, 20-29 July. Washington, D.C.: American Geophysical Union.Payne, M.W., 1976, Basinal Sandstone Facies, Delaware Basin, West Texas and Southeast New Mexico: AAPG Bulletin. Vol. 60, no. 4, p. 517-527.

Pray, L. C., 1988, Trail Guide: day one, Bone and Shu- mard Canyon area, *in* S. T. Reid et al., eds., Guadalupe Mountains revisited, West Texas Geo- logical Society Publication, 88-84, p. 41–60.

Pigott, J.D., 2017, GEOL 5363: Carbonate Geology. Fall 2013. Unpublished Lecture notes

Sarg, J.F., Rossen, C., Lehmann, P.J., and Pray, L.C., 1988, Geologic guide to the western escarpment, Guadalupe Mountains, Texas: SEPM (Permian Basin Sec.) Pub. 88-30, p. 60.Rajabi, Ali M; Hosseini, Alireza; Heidari, Alireza "The New Empirical Formula to Estimate the Uniaxial Compressive Strength of Limestone; North of Saveh a case Study" *Journal of Engineering Geology*, Vol. 11, No. 3, Autumn 2017.

`

Rajabi, Ali & Hosseini, Alireza & Heidari, Alireza. (2017). The New Empirical Formula to Estimate the Uniaxial Compressive Strength of Limestone; North of Saveh a Case Study. Journal of Engineering Geology. 11. 159-180. RIEGL Laser Instrument Systems, 2012, RIEGL Glossary.

RIEGL Laser Instrument Systems, 2013, RIEGL VZ-400 Technical Documentation and Users Instructions.

Rickman, R., Mullen, M. J., Petre, J. E., Grieser, W. V., & Kundert, D. (2008, January 1). A Practical Use of Shale Petrophysics for Stimulation Design Optimization: All Shale Plays Are Not Clones of the Barnett Shale. Society of Petroleum Engineers. doi:10.2118/115258-MSRoberts, 2018 (?)

Ross, C.A. and J.R.P. Ross, 1994, Permian Sequence Stratigraphy and Fossil Zonation: Canadian Society of Petroleum Geologists, v. 17, p. 219-231.

Sajid, M., & Arif, M. (2015). Reliance of physico-mechanical properties on petrographic characteristics: Consequences from the study of utla granites, north-west pakistan. *Bulletin of Engineering Geology and the Environment, 74*(4), 1321-1330.

Scholle, P.A., Ulmer-Scholle, D.S., Nestell, M.K., and Nestell, G.P., 2015, Guadalupian age basinal facies in the western Delaware Mountain Group outcrop belt, Guadalupe and Apache mountians: in Trentham, R.C. (ed.), West Texas Geological Society Annual Fall Field Trip, October 9-11, 44 p.

Schreiber, B. C. "Environments of Subaqueous Gypsum Deposition." *SEPM Short Course*, no. 4, 1978, pp. 43-73. *ProQuest*

Silver, B.A. and R.G. Todd, 1969, Permian Cyclic Strata, Northern Midland and Delaware Basins, West Texas and Southeastern New Mexico: AAPG Bulletin, v. 53.11, p. 2223-2251. Slatt, R. M., and Y. Abousleiman, 2011, Multi-scale, brittleductile couplets in unconventional gas shales: Merging sequence stratigraphy and geomechanics: AAPG Search and Discovery, #80181.

Sharma, P. K., Manoj Khandelwal, and T. N. Singh. "A correlation between Schmidt hammer rebound numbers with impact strength index, slake durability index and P-wave velocity." International Journal of Earth Sciences 100, no. 1 (2011): 189-195.

Split Engineering, 2019, Tutorial 3: Split-FX user tutorial, 2005. Unpublished user tutorial

Thermo Fisher Scientific, 2010, User's Guide Version 7.0.1.

Tribovillard, N., T.J. Algeo, F. Baudin, A. Riboulleau, 2006, Analysis of marine environmental conditions based on molybdenum-uranium covariation- Applications to Mesozoic Plaeoceanography: Chemical Geology, v. 324-325, p. 46-58.

Tribovillard, N., T. Lyons, A. Riboulleau, 2006, Trace metals as paleoredox and paleoproductivity proxies: An Update: Chemical Geology, v. 232, p. 12-32.

Tyrrell Jr, Willis W. "Criteria useful in interpreting environments of unlike but time-equivalent carbonate units (Tansill-Capitan-Lamar), Capitan reef complex, West Texas and New Mexico." (1969).

`

Winkler, Stefan, and John A. Matthews. "Comparison of electronic and mechanical Schmidt hammers in the context of exposure-age dating: are Q-and R-values interconvertible?." Earth Surface Processes and Landforms 39, no. 8 (2014): 1128-1136.

Williams, J. W., Alsleben, H., & Enderlin, M. (2016). Correlation between rock strength and chemostratigraphy in barnett shale cores using energy-dispersive X-ray fluorescence (ED-XRF) and micro-rebound hammer hardness. *Abstracts with Programs - Geological Society of America, 48*(7), Abstract no. 241-8.

Wright, Wayne "Depositional History of the Desmoinesian Succession (Middle Pennsylvanian) in the Permian Basin" (2008).

Verma, Sumit, et al. "Estimation of Total Organic Carbon and Brittleness Volume."*Interpretation (Tulsa)*, vol. 4, no. 3, 2016, pp. T373-T385. *ProQuest*

Viles, H.A. & Goudie, Andrew & Grab, Stefan & Lalley, Jennifer. (2011). The use of the Schmidt Hammer and Equotip for rock hardness assessment in geomorphology and heritage science: A comparative analysis. Process. Landforms. 36. 320-333.

Yang, Kenn-Ming, Dorobek, Stephen L. (1995) "The Permian Basin of West Texas and New Mexico: Flexural Modeling and Evidence for Lithospheric Heterogeneity Across the Marathon Foreland", Stratigraphic Evolution of Foreland Basins, Steven L. Dorobek, Gerald M. Ross

Yilmaz I, Sendir H (2002) Correlation of Schmidt hardness with unconfined compressive strength and young's modulus in gypsum from Sivas (Turkey). Eng Geol 66:211–219

Zhang, D., Dai, Y., Ma, X., Zhang, L., Zhong, B., Wu, J., & Tao, Z. (2018). An analysis for the influences of fracture network system on multi-stage fractured horizontal well productivity in shale gas reservoirs. *Energies*, *11*(2), 414.

`

APPENDIX A: XRF mineralogy

Transect	Letter	DEPTH (ft)	% GYPSUM	% DOLOMITE	% CALCITE	% QTZ-CHERT	% KSPAR	% ALB-MICA-CLAY	% PYRITE	Psuedo-Gamma
1		1	0	0	89.72628228	5.405775258	1.55376063	2.074802911	1.23937892	
1		2	0.355104032	44.12061831	5.518589713	34.78511928	4.201840257	8.857816507	2.1609119	
1		3	0	0	89.95993996	5.682711951	0.868563778	2.426965618	1.061818694	
1		4	0	0	84.16271581	6.602914772	3.72553974	3.654294425	1.854535252	
1		5	0	0	81.51400054	5.240031212	4.775806369	5.956268318	2.513893564	
1		6	0	23.56286854	21.7156957	26.58983435	11.91291514	10.58145171	5.637234558	
1		7	0	22.7684642	4.684080361	44.79153469	11.15135439	10.11338903	6.491177334	
1		8	0	24.19836278	12.6583435	31.05061228	15.5641522	9.012607483	7.515921757	
1		9	0	41.77372695	0	23.10430888	9.720750283	17.61957068	7.781643219	
1		10	5.730243237	0	54.95445212	17.42413327	7.976277122	9.90468869	4.010205562	
1		11	0	0	34.63680769	23.3057076	23.63579824	9.857336489	8.564349979	
1		12	0	23.35628172	41.69923388	6.925186687	14.45708493	7.189513449	6.372699337	
1		13	0	0	49.38064762	17.47120458	16.45862236	9.616666004	7.07285944	
1		14	0	0	56.73760738	16.38044518	13.97559174	7.151155447	5.755200253	
1		15	0	27.69317525	32.97784297	14.42028185	11.52980921	7.866455151	5.512435556	
1		16	0	0	62.93965165	12.02894678	12.06978643	7.797564955	5.16405018	
1		17	0	20.09153997	34.63070826	15.92773325	16.32825448	6.945577873	6.076186174	
1		18	0	25.05035609	34.53358016	14.52345419	13.59205164	7.215186662	5.085371269	
1		19	0	0	47.10345611	15.73430906	21.04459374	8.292128931	7.825512156	
1		20	0	18.31030915	6.536771465	57.0950722	4.864512791	8.843456194	4.349878205	
1		21	0	14.54293269	30.43150726	16.86019678	20.8634676	8.609950207	8.691945463	
1		22	0	0	45.91999638	9.81714197	21.10831493	13.18122431	9.973322412	
1		23	0	0	44.48820174	18.76032215	19.49091606	9.355934418	7.90462564	
1		24	0	23.51713561	35.16661971	9.860106159	15.11936546	9.453972107	6.882800961	
1		25	0	0	48.49167584	16.00548501	19.38850447	8.928065227	7.186269449	
1		26	0	29.52665817	17.51575941	20.01030718	16.92098106	8.669048782	7.357245396	
1		27	0	0	52.96100793	13.11817316	17.83743068	9.538310286	6.545077939	
1		28	0	0	44.70184983	14.48249069	20.21625652	11.47757592	9.121827032	
1		29	0	0	80.52664643	5.728348041	5.123387835	4.640005869	3.981611827	
1		30	0	43.83390505	16.632731	14.47840987	6.235339852	14.78010108	4.039513147	
1		31	0	22.85185135	29.71407732	20.6933963	14.0066018	7.047695969	5.686377262	
1		32	0	0	52.31063985	19.4409945	13.21868674	10.02246182	5.007217087	
1		33	0	0	58.43867932	15.65619004	13.64040505	6.598824842	5.665900751	
1		34	0	0	40.72948147	24.44610888	15.60526852	11.34056315	7.878577972	
1	D	49.625	0	40.35711694	0	28.90404874	7.045157663	19.07098773	4.62268892	
1	E	65.25	0	22.90567474	65.35620499	3.234498886	1.71814852	5.69089137	1.0945815	
2	A	75.6875	0	25.85658306	30.5580227	16.12329978	12.9453452	9.304581427	5.21216783	
2	B	88.875	0	36.55637301	22.9752811	10.4727457	14.67044527	11.24251285	4.08264207	
2	C	102.0625	0	22.29414064	12.87995855	18.32631992	23.94583925	13.94088277	8.61285887	
2	D	115	0	14.08970494	30.46902286	18.21289476	19.09404243	13.55025961	4.58407541	
3	A	131.08	0	18.67881169	70.46325213	2.805178659	1.858513277	5.285543212	0.908701031	
3	B	147.16	0	28.41986755	0.43219265	39.76809747	8.468313063	15.49077424	7.420755024	
3	C	163.24	0	21.05683671	68.22844809	4.192706727	0.98567038	4.84470551	0.691632583	
3	D	179.32	0	41.28611189	0	30.84268381	8.694649903	16.12400686	3.052547534	
4	A	195.4	0	25.80399967	51.76586653	7.077148497	3.664546122	9.835191474	1.853247709	
4	B	211.48	0	12.59562599	70.78143915	5.830431246	2.913719374	6.600283384	1.278500853	
4	C	227.56	0	36.4013403	0	36.90405296	7.58728015	14.16528456	4.942042024	
4	D	243.64	0	28.63189474	0	47.33932889	6.063418059	13.65190256	4.31345575	
5	A	259.72	0	35.48025248	0	34.24464325	8.72182163	15.61277336	5.940509276	
5	B	275.8	0	24.87926738	62.89789609	4.339584144	0.84963646	6.314447285	0.719168636	
5	C	291.88	0	23.70399934	9.967264778	28.80909877	13.2545816	13.74241038	10.52264513	
5	D	307.96	0	16.12069421	66.00563621	5.79887166	3.672471235	6.909843919	1.492482767	
6		0	0	22.95275399	16.47490743	29.1428374	6.269692974	11.43725992	13.72254828	38901.04
6		6	0	10.48005893	75.94726336	4.278104626	2.17520154	5.816943927	1.302427613	27517.44
6		12	0	25.40798268	18.16510833	24.79931162	5.39343065	10.77549054	15.45867617	33626.6
6		17	0	18.86326182	69.71237444	3.715192214	1.045916683	5.159338085	1.503916761	14312.12
6		20	0	39.14246699	0	34.74588386	7.206331582	11.83634409	7.068973474	38370.36
6		40	0	19.6318174	69.68410459	3.660005754	1.222040554	4.798912073	1.003119638	16978.84
6		64	0	33.36949638	0	36.42101392	11.11866809	13.60019523	5.490626365	50959.96
6		100	0	20.31137238	70.4583663	3.399121383	0.751769051	4.317610903	0.761759986	10393.04
6		136	0	32.76928772	0	42.0821446	4.375717597	15.59543285	5.17741723	22203.2
6		148	0	18.48044737	68.30536405	5.621564105	1.312095586	5.395226598	0.885302294	16155.6
6		163	0	32.97458846	0	35.7039527	11.10109742	14.18367908	6.03668234	55369.84
6		175	0	0	88.11168193	4.298901578	1.532426807	5.090597193	0.966392491	19036.68
6		190	0	33.52730142	0	35.42034251	9.600115099	15.58829714	5.863943832	45043.16
6		202	0	21.78723228	61.95687033	6.309591668	2.680593766	5.779846331	1.485865624	32140.4
6		214	0	17.89371439	18.97657957	50.24739143	0.724030618	9.787825805	2.370458193	3527.04
6		238	0	22.73611675	70.80090157	2.318944943	0	3.677333405	0.466703333	3588.88
6		262	0	26.54165593	46.69659107	16.88552306	1.786907244	6.482480241	1.606842463	15556.88
6		290	0	27.78850481	60.48577014	3.804833178	2.344788981	4.725644304	0.850458581	30378.52
6		314	0	29.66095558	0	33.89204471	16.07231365	15.85889549	4.515790563	75180.8
6		329	0	18.89217445	70.30875551	3.980467244	1.759448534	4.123179421	0.935974843	24015.04
6		341	0	34.93289856	7.926772468	30.32012668	8.099068528	13.84892566	4.872208108	41684.64
6		352	0	26.33249309	65.05447793	1.874793846	1.145848603	4.951677026	0.640709501	17471.6
6		376	0	35.23416246	0	37.04408264	4.116171301	14.79050826	8.815075347	22575.4
6		384	0	14.23262861	75.16503026	3.550829254	1.646101128	4.579664376	0.82574637	20754.36
6		399	0	37.48808359	3.934724387	35.30628755	4.179677597	10.68779518	8.403431684	25617.12
6		406	0	24.29533985	65.57247584	2.763862773	1.878369452	4.65731868	0.832633407	25856.92
6		416	0	26.39714527	0	55.46597205	2.776029013	12.46489115	2.895962511	14984.2
6		431	0	21.24120285	64.71577784	2.369925012	4.420395776	5.918959718	1.333738803	58673.36
6		446	0	28.25403738	0	47.60417329	5.976277863	14.35087074	3.814640731	31121.64
6		461	0	13.7492067	74.36113144	4.056255188	0.632269067	6.431332511	0.769805098	8292.4

Transect	Letter	DEPTH (ft)	% GYPSUM	% DOLOMITE	% CALCITE	% QTZ-CHERT	% KSPAR	% ALB-MICA-CLAY	% PYRITE	Psuedo-Gamma	Transect	Letter	DEPTH (ft)	% GYPSUM	% DOLOMITE	% CALCITE	% QTZ-CHERT	% KSPAR	% ALB-MICA-CLA'	% PYRITE	Psuedo-Gamma
7		0	0	21.0745216	67.70924366	3.971752989	0.939831848	5.453639537	0.851010361	13020.84	8	A		0	0	93.68771094	1.613403014	0	4.365985565	0.332900481	
7		13	0	45.15639593	0	30.16791207	4.018519501	16.46449237	4.192680123	26155.08	8	B		0	31.65079514	11.43778869	37.47511694	3.722602414	12.78531009	2.928386721	
7		24	0	18.12833004	72.52753144	3.249230649	0.356091975	5.10957216	0.629243742	5034.16	8	C		0	13.15984358	79.40614202	1.870532961	0	5.172469755	0.391011684	
7		30	0	26.66510585	0.620931184	45.78837724	6.812905498	13.5537224	6.558975836	33420.28	8	D		0	26.55027628	0	52.21787116	1.143463775	15.29450622	4.79388256	
7		46	0	11.16952467	81.35896604	1.988984884	0.902182999	3.965556615	0.614784794	13475.92	10	A		0	20.39053368	72.38139264	2.458430696	0	4.312987466	0.456655525	
7		57.5	0	38.63982355	0	42.37542453	2.616020818	13.3616909	3.007040202	15574.28	10	B		0	24.75092768	11.75460388	30.69404374	9.988065828	11.8579748	10.95438407	
7		64.5	0	28.46389271	57.86854755	5.088997385	0	7.834123905	0.744438452	3603793.76	9	A		0.521672646	10.98937	80.72324392	3.358881696	0.42956938	3.959043521	0.018218843	
7		77.5	0	28.0267871	0	47.72158187	6.301358844	14.42945193	3.520820261	31625.2	9	B		1.773052176	38.00023723	0	42.97544678	4.409655302	12.77109494	0.070513571	
7		93	0	15.83752395	76.16372878	2.91291159	0	4.716985432	0.368850255	4271.24											
7		109	0	34.120071	0	46.31896777	2.346928482	13.66414144	3.549891302	12743.12											
7		121	0	30.64140756	56.25766157	4.768395155	0	7.732463337	0.600072377	3603580.48											
7		138	0	36.88720391	0	41.4168972	2.961012145	12.68877394	6.046112803	15859.44											
7		149	0	19.87933103	68.5551161	4.257981681	0	6.60747129	0.700099902	5871.68											
7		154	0	26.79435426	20.75779201	38.04063565	0.514745094	11.21191421	2.680558776	3003.64											
7		159	0	21.08529785	70.9461893	2.672849557	0	4.780025573	0.515637727	3711.72											
7		169.5	0	9.007497791	81.9340274	2.750413608	1.299205088	4.180968178	0.827887935	18319.32											
7		175.5	0	25.66338573	6.532880077	45.31868706	2.198040605	10.30951298	9.977493553	12075.8											
7		178.5	0	24.6537918	67.41080582	2.78217186	0	4.571234411	0.581996112	3721.48											
7		190	0	35.94885955	12.50382242	30.15982424	5.389407582	13.72437445	2.273711758	34040.76											
7		194	0	18.81470185	72.31632848	3.929499449	0.301140323	4.070901552	0.56742834	4416.52											
7		199.5	0	29.58777688	0	50.61441262	3.208390274	13.03607241	3.553347814	14942.28											
7		213	0	17.79137965	73.88760676	2.851863391	0	4.83425164	0.634898553	4415.52											
7		216.75	0	32.67752847	0	47.85609154	2.747412485	11.32605646	5.39291105	14040.08											
7		219.25	0	25.37443683	64.09978493	2.407735659	0	7.717970476	0.400072108	3603563.52											
7		225.5	0	29.21206727	0	47.25585023	1.374833985	19.32480367	2.832444849	5660.12											
7		228.5	0	36.10066308	0	39.05710166	2.695369823	15.44888158	6.697983848	15095.48											
7		231	0	20.38864684	66.85059046	4.219227434	0.442489832	7.010806674	1.088238757	6033.4											
7		233.75	0	18.54450398	74.93266284	1.6906025	0	4.453368224	0.378862462	3531.6											
7		239.25	0	31.76965292	0	50.36821212	1.666869312	11.87925323	4.316012421	8711.8											
7		244.75	0	15.01616858	77.70610741	2.836647562	0	4.066950571	0.374125877	3461											
7		253.75	0	31.30868499	0	51.86818028	2.130423356	12.02670486	2.666006509	10268.64											
7		255.25	0	11.71058701	79.72659485	3.125345928	0.551620482	4.088292483	0.79755924	7894.2											
7		265.25	0	39.22460826	0	36.14549075	4.095055586	16.4632739	4.071571496	21795.08											
7		268.25	0	16.80973496	73.85976067	3.138030231	0	5.668694155	0.52377998	3563.96											
7		278.25	0	37.74916955	0	36.12010046	6.053726442	14.92441643	5.152587127	31441.64											
7		280.25	0	13.49142375	76.28835398	4.016099505	0.577585637	4.675998352	0.950538782	7717.32											
7		289.25	0	29.22188833	0	52.04976976	2.207265139	12.42436482	4.096711956	11167.44											
7		294.25	0	9.02328043	82.05246077	2.87695276	0	5.447687545	0.599618491	5575.04											
7		304.25	0	30.00170113	0	48.54998705	4.34298021	11.91686324	5.188468373	22347.28											
7		309.75	0	15.68812651	72.57624356	4.129349575	1.18493438	5.267643929	1.153702046	15557.92											
7		316.75	0	23.75147695	68.22429458	2.364864157	0	5.150574523	0.50878979	3638.24											
7		328.75	0	28.9233773	59.57120671	3.266200174	1.511410998	5.579185995	1.148618817	19924.88											
7		331.25	0	25.6172124	64.16349492	3.934435805	0.482190507	4.965189565	0.837476799	6750.6											
7		338.25	0	26.29339489	0	55.8621225	1.618848834	13.87826683	2.347366954	7302.64											
7		344.25	0	12.37141715	76.53875202	3.660489502	0.519490675	6.060421256	0.849429403	6848.44											
7		349.25	0	14.06539187	73.75289691	4.331810828	1.66719102	5.060079888	1.122629484	21272.84											
7		355.25	0	34.91649969	0	45.51000029	2.814809784	10.81658542	5.94210482	15483.8											
7		358.25	0	38.49091707	0	44.83556203	0.629554595	14.23804976	1.805916533	3272.16											
7		359.75	0	12.7609806	81.4182519	2.313748326	0	3.109612336	0.397406839	3549.8											
7		367.75	0	12.00810282	80.42906899	1.973833223	0.381639436	4.521994577	0.685360953	5458.6											

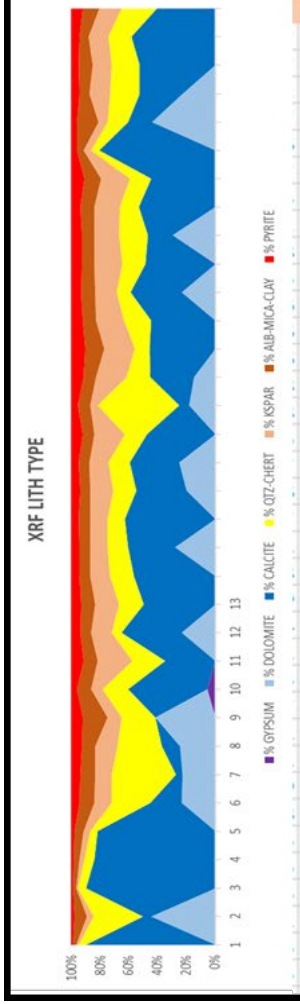

DEPTH	% GYPSUM	% DOLOMITE	% CALCITE	% QTZ-CHERT	% KSPAR	% ALB-MICA-CLAY	% PYRITE
1	0	0	89.72628228	5.405775258	1.55376063	2.074802911	1.23937892
2	0.355104032	44.12061831	5.518589713	34.78511928	4.201840257	8.857816507	2.1609119
3	0	0	89.95993996	5.682711951	0.868563778	2.426965618	1.061818694
4	0	0	84.16271581	6.602914772	3.72553974	3.654294425	1.854535252
5	0	0	81.51400054	5.240031212	4.775806369	5.956268318	2.513893564
6	0	23.56286854	21.7156957	26.58983435	11.91291514	10.58145171	5.637234558
7	0	22.7684642	4.684080361	44.79153469	11.15135439	10.11338903	6.491177334
8	0	24.19836278	12.6583435	31.05061228	15.5641522	9.012607483	7.515921757
9	0	41.77372695	0	23.10430888	9.720750283	17.61957068	7.781643219
10	5.730243237	0	54.95445212	17.42413327	7.976277122	9.90468869	4.010205562
11	0	0	34.63680769	23.3057076	23.63579824	9.857336489	8.564349979
12	0	23.35628172	41.69923388	6.925186687	14.45708493	7.189513449	6.372699337
13	0	0	49.38064762	17.47120458	16.45862236	9.616666004	7.07285944
14	0	0	56.73760738	16.38044518	13.97559174	7.151155447	5.755200253
15	0	27.69317525	32.97784297	14.42028185	11.52980921	7.866455151	5.512435556
16	0	0	62.93965165	12.02894678	12.06978643	7.797564955	5.16405018
17	0	20.09153997	34.63070826	15.92773325	16.32825448	6.945577873	6.076186174
18	0	25.05035609	34.53358016	14.52345419	13.59205164	7.215186662	5.085371269
19	0	0	47.10345611	15.73430906	21.04459374	8.292128931	7.825512156
20	0	18.31030915	6.536771465	57.0950722	4.864512791	8.843456194	4.349878205
21	0	14.54293269	30.43150726	16.86019678	20.8634676	8.609950207	8.691945463
22	0	0	45.91999638	9.81714197	21.10831493	13.18122431	9.973322412
23	0	0	44.48820174	18.76032215	19.49091606	9.355934418	7.90462564
24	0	23.51713561	35.16661971	9.860106159	15.11936546	9.453972107	6.882800961
25	0	0	48.49167584	16.00548501	19.38850447	8.928065227	7.186269449
26	0	29.52665817	17.51575941	20.01030718	16.92098106	8.669048782	7.357245396
27	0	0	52.96100793	13.11817316	17.83743068	9.538310286	6.545077939
28	0	0	44.70184983	14.48249069	20.21625652	11.47757592	9.121827032
29	0	0	80.52664643	5.728348041	5.123387835	4.640005869	3.981611827
30	0	43.83390505	16.632731	14.47840987	6.235339852	14.78010108	4.039513147
31	0	22.85185135	29.71407732	20.6933963	14.0066018	7.047695969	5.686377262
32	0	0	52.31063985	19.4409945	13.21868674	10.02246182	5.007217087
33	0	0	58.43867932	15.65619004	13.64040505	6.598824842	5.665900751
34	0	0	40.72948147	24.44610888	15.60526852	11.34056315	7.878577972

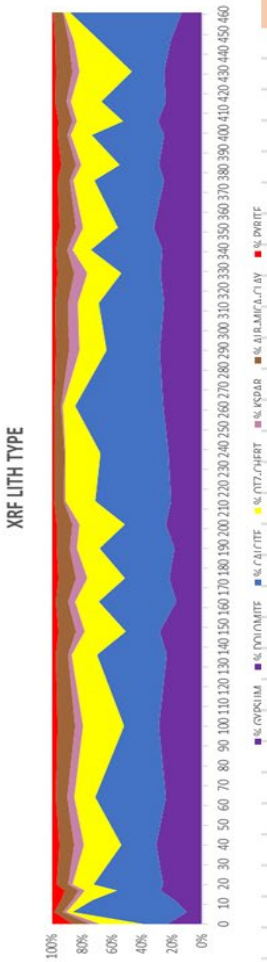

DEPTH	% GYPSUM	% DOLOMITE	% CALCITE	% QTZ-CHERT	% KSPAR	ALB-MICA-CL	% PYRITE	Pseudo-Gamma
0	0	22.952754	16.47490743	29.1428374	6.269693	11.43726	13.722548	38901.04
6	0	10.480059	75.94726336	4.278104626	2.1752015	5.8169439	1.3024276	27517.44
12	0	25.407983	18.16510833	24.79931162	5.3934306	10.775491	15.458676	33626.6
17	0	18.863262	69.71237444	3.715192214	1.0459167	5.1593381	1.5039168	14312.12
20	0	39.142467	0	34.74588386	7.2063316	11.836344	7.0689735	38370.36
40	0	19.631817	69.68410459	3.660005754	1.2220406	4.7989121	1.0031196	16978.84
64	0	33.369496	0	36.42101392	11.118668	13.600195	5.4906264	50959.96
100	0	20.311372	70.4583663	3.399121383	0.7517691	4.3176109	0.76176	10393.04
136	0	32.769288	0	42.0821446	4.3757176	15.595433	5.1774172	22203.2
148	0	18.480447	68.30536405	5.621564105	1.3120956	5.3952266	0.8853023	16155.6
163	0	32.974588	0	35.7039527	11.101097	14.183679	6.0366823	55369.84
175	0	0	88.11168193	4.298901578	1.5324268	5.0905972	0.9663925	19036.68
190	0	33.527301	0	35.42034251	9.6001151	15.588297	5.8639438	45043.16
202	0	21.787232	61.95687033	6.309591668	2.6805938	5.7798463	1.4858656	32140.4
214	0	17.893714	18.97657957	50.24739143	0.7240306	9.7878258	2.3704582	3527.04
238	0	22.736117	70.80090157	2.318944943	0	3.6773334	0.4667033	3588.88
262	0	26.541656	46.69659107	16.88552306	1.7869072	6.4824802	1.6068425	15556.88
290	0	27.788505	60.48577014	3.804833178	2.344789	4.7256443	0.8504586	30378.52
314	0	29.660956	0	33.89204471	16.072314	15.858895	4.5157906	75180.8
329	0	18.892174	70.30875551	3.980467244	1.7594485	4.1231794	0.9359748	24015.04
341	0	34.932899	7.926772468	30.32012668	8.0990685	13.848926	4.8722081	41684.64
352	0	26.332493	65.05447793	1.874793846	1.1458486	4.951677	0.6407095	17471.6
376	0	35.234162	0	37.04408264	4.1161713	14.790508	8.8150753	22575.4
384	0	14.232629	75.16503026	3.550829254	1.6461011	4.5796644	0.8257464	20754.36
399	0	37.488084	3.934724387	35.30628755	4.1796776	10.687795	8.4034317	25617.12
406	0	24.29534	65.57247584	2.763862773	1.8783695	4.6573187	0.8326334	25856.92
416	0	26.397145	0	55.46597205	2.776029	12.464891	2.8959625	14984.2
431	0	21.241203	64.71577784	2.369925012	4.4203958	5.9189597	1.3337388	58673.36
446	0	28.254037	0	47.60417329	5.9762779	14.350871	3.8146407	31121.64
461	0	13.749207	74.36113144	4.056255188	0.6322691	6.4313325	0.7698051	8292.4

`

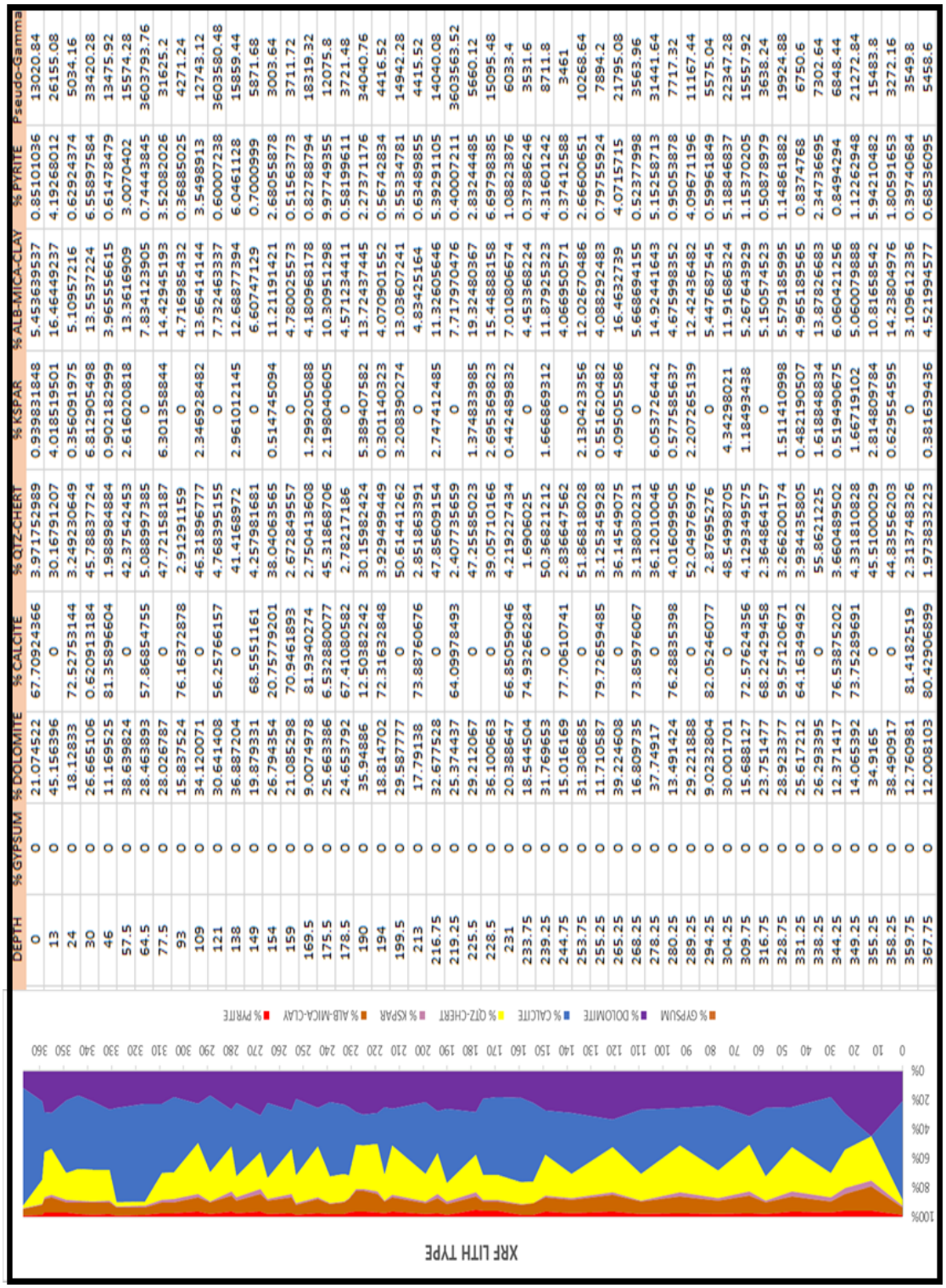

DEPTH	% GYPSUM	% DOLOMITE	% CALCITE	% QTZ-CHERT	% KSPAR	% ALB-MICA-CLAY	% PYRITE	Pseudo-Gamma
0	0	21.074522	67.70924366	3.971752989	0.939831848	5.453639537	0.851010036	13020.84
13	0	45.156396	0	30.16791207	4.018519501	16.46449237	4.19268012	26155.08
24	0	18.12833	72.52753144	3.249230649	0.356091975	5.109572216	0.62924374	5034.16
30	0	26.665106	0.620913184	45.78837724	6.812905498	13.5537224	6.55897584	33420.28
46	0	11.169525	81.35896604	1.988984884	0.902182999	3.965556615	0.61478479	13475.92
57.5	0	38.639824	0	42.37542453	2.616020818	13.3616909	3.0070402	15574.28
64.5	0	28.463893	57.86854755	5.088997385	0	7.834123905	0.74443845	3603793.76
77.5	0	28.026787	0	47.72158187	6.301358844	14.42945193	3.52082026	31625.2
93	0	15.837524	76.16372878	2.91291159	0	4.716985432	0.36885025	4271.24
109	0	34.120071	0	46.31896777	2.346928482	13.66414144	3.5498913	12743.12
121	0	30.641408	56.25766157	4.768395155	0	7.732463337	0.60007238	3603580.48
138	0	36.887204	0	41.4168972	2.961012145	12.68877394	6.0461128	15859.44
149	0	19.879331	68.5551161	4.257981681	0	6.60747129	0.7000999	5871.68
154	0	26.794354	20.75779201	38.04063565	0.514745094	11.21191421	2.68055878	3003.64
159	0	21.085298	70.9461893	2.672849557	0	4.780025573	0.51563773	3711.72
169.5	0	9.0074978	81.9340274	2.750413608	1.299205088	4.180968178	0.82788794	18319.32
175.5	0	25.663386	6.532880077	45.31868706	2.198040605	10.30951298	9.97749355	12075.8
178.5	0	24.653792	67.41080582	2.78217186	0	4.571234411	0.58199611	3721.48
190	0	35.94886	12.50382242	30.15982424	5.389407582	13.72437445	2.27371176	34040.76
194	0	18.814702	72.31632848	3.929499449	0.301140323	4.070901552	0.56742834	4416.52
199.5	0	29.587777	0	50.61441262	3.208390274	13.03607241	3.55334781	14942.28
213	0	17.79138	73.88760676	2.851863391	0	4.83425164	0.63489855	4415.52
216.75	0	32.677528	0	47.85609154	2.747412485	11.32605646	5.39291105	14040.08
219.25	0	25.374437	64.09978493	2.407735559	0	7.717970476	0.40007211	3603563.52
225.5	0	29.212067	0	47.25585023	1.374833985	19.32480367	2.83244485	5660.12
228.5	0	36.100663	0	39.05710166	2.695369823	15.44888158	6.69798385	15095.48
231	0	20.388647	66.85059046	4.219227434	0.442489832	7.010806674	1.08823876	6033.4
233.75	0	18.544504	74.93266284	1.6906025	0	4.453368224	0.37886246	3531.6
239.25	0	31.769653	0	50.36821212	1.666869312	11.87925323	4.31601242	8711.8
244.75	0	15.016169	77.70610741	2.836647562	0	4.066950571	0.37412588	3461
253.75	0	31.308685	0	51.86818028	2.130423356	12.02670486	2.66600651	10268.64
255.25	0	11.710587	79.72659485	3.125345928	0.551620482	4.088292483	0.79755924	7894.2
265.25	0	39.224608	0	36.14549075	4.095055586	16.4632739	4.0715715	21795.08
268.25	0	16.809735	73.85976067	3.138030231	0	5.668694155	0.52377998	3563.96
278.25	0	37.74917	0	36.12010046	6.053726442	14.92441643	5.15258713	31441.64
280.25	0	13.491424	76.28835398	4.016099505	0.577585637	4.675998352	0.95053878	7717.32
289.25	0	29.221888	0	52.04976976	2.207265139	12.42436482	4.09671196	11167.44
294.25	0	9.0232804	82.05246077	2.87695276	0	5.447687545	0.59961849	5575.04
304.25	0	30.001701	0	48.54998705	4.342980211	11.91686324	5.18846837	22347.28
309.75	0	15.688127	72.57624356	4.129349575	1.184934388	5.267643929	1.15370205	15557.92
316.75	0	23.751477	68.22429458	2.364864157	0	5.150574523	0.50878979	3638.24
328.75	0	28.923377	59.57120671	3.266200174	1.511410998	5.579185995	1.14861882	19924.88
331.25	0	25.617212	64.16349492	3.934435805	0.482190507	4.965189565	0.8374768	6750.6
338.25	0	26.293395	0	55.8621225	1.618848834	13.87826683	2.34736695	7302.64
344.25	0	12.371417	76.53875202	3.660489502	0.519490675	6.060421256	0.8494294	6848.44
349.25	0	14.065392	73.75289691	4.331810828	1.66719102	5.060079888	1.12262948	21272.84
355.25	0	34.9165	0	45.51000029	2.814809784	10.81658542	5.94210482	15483.8
358.25	0	38.490917	0	44.83556203	0.629554595	14.23804976	1.80591653	3272.16
359.75	0	12.760981	81.4182519	2.313748326	0	3.109612336	0.39740684	3549.8
367.75	0	12.008103	80.42906899	1.973833223	0.381639436	4.521994577	0.68536095	5458.6

`

APPENDIX B: Raw SilverSchmidt data

Shot count						Q	Valid	Total	Std dev.	Form	Form-Factor	Carb-Factor	Transect	Letter
2179	77	78.5	74.5	77.5	76.5	76.8	5	5	1.5	Cylinder (87%)	0.8	0.96	1	A
2184	67	74.5	75	77	76.5	74	5	5	4	Cylinder (82%)	0.8	0.96	1	B
2189	73	78	70.5	70.5	77.5	73.9	5	5	3.7	Cylinder (82%)	0.8	0.96	1	C
2194	79	78.5	79	75	74	77.1	5	5	2.4	Cylinder (87%)	0.8	0.96	1	D
2199	73.5	72	75.5	71	71.5	72.7	5	5	1.8	Cylinder (82%)	0.8	0.96	1	E
2219	78	75	75	72.5	72	74.5	5	5	2.4	Cylinder (84%)	0.8	0.96	2	A
2224	57	62	60.5	58.5	63	60.2	5	5	2.5	Cylinder (78%)	0.8	0.96	2	B
2229	74	74	71	72.5	74	73.1	5	5	1.3	Cylinder (82%)	0.8	0.96	2	C
2234	17	21	25	32	33.5	25.7	5	5	7	Cylinder (80%)	0.8	0.96	2	D
2239	76.5	76	76.5	78	75.5	76.5	5	5	0.9	Cylinder (87%)	0.8	0.96	3	A
2244	63	58.5	66.5	59.5	62.5	62	5	5	3.2	Cylinder (80%)	0.8	0.96	3	B
2254	75	75	69.5	72	64.5	71.2	5	5	4.4	Cylinder (80%)	0.8	0.96	3	C
2264	55.5	61.5	55	55.5	56	56.7	5	5	2.7	Cylinder (81%)	0.8	0.96	3	D
2269	60.5	62	61	60	53	59.3	5	5	3.6	Cylinder (78%)	0.8	0.96	4	A
2274	58	51	56	62.5	44.5	54.4	5	5	6.9	Cylinder (83%)	0.8	0.96	4	B
2279	37.5	37	40.5	37.5	40.5	38.6	5	5	1.7	Cylinder (80%)	0.8	0.96	4	C
2284	47	48.5	46.5	50	44.5	47.3	5	5	2.1	Cylinder (80%)	0.8	0.96	4	D
2299	45	41	44.5	28.5	43	40.4	5	5	6.8	Cylinder (80%)	0.8	0.96	5	A
2304	71.5	70	66	63	72	68.5	5	5	3.9	Cylinder (82%)	0.8	0.96	5	B
2309	61.5	51.5	58.5	59	59	57.9	5	5	3.8	Cylinder (81%)	0.8	0.96	5	C
2319	36.5	39.5	42.5	36	45.5	40	5	5	4	Cylinder (80%)	0.8	0.96	5	D
2324	74	74.5	72.5	70	77	73.6	5	5	2.6	Cylinder (82%)	0.8	0.96	6	
2329	72.5	77	77	78.5	75.5	76.1	5	5	2.3	Cylinder (87%)	0.8	0.96	6	
2338	61	63.5	62.5	64.5	64.5	63.2	5	5	1.5	Cylinder (82%)	0.8	0.96	6	
2343	78	77.5	78	81	77.5	78.4	5	5	1.5	Cylinder (87%)	0.8	0.96	6	
3401	72	75	75	75	74	74.2	5	5	1.3	Cylinder (87%)	0.8	0.96	6	
3406	66	62	67.5	59	60.5	63	5	5	3.6	Cylinder (87%)	0.8	0.96	6	
3411	69	77	75.5	79.5	74	75	5	5	3.9	Cylinder (87%)	0.8	0.96	6	
3416	59	64.5	67.5	64	62	63.4	5	5	3.2	Cylinder (87%)	0.8	0.96	6	
3421	66	67.5	66.5	69.5	69	67.7	5	5	1.5	Cylinder (87%)	0.8	0.96	6	
3426	65	66.5	69	68	65.5	66.8	5	5	1.7	Cylinder (87%)	0.8	0.96	6	
3431	73	72	69.5	75	74	72.7	5	5	9.3	Cube 150mm (100%)	1	1	6	
3436	23.5	18	19.5	18.5	16	19.1	5	5	2.8	Cube 150mm (100%)	1	1	6	
3441	65.5	67	67	69.5	68	67.4	5	5	5	Cube 150mm (100%)	1	1	6	
3446	56.5	55	57.5	50	53	54.4	5	5	5.5	Cube 150mm (100%)	1	1	6	
3462	75.5	74.5	71.5	72.5	71	73	5	5	1.9	Cube 150mm (100%)	1	1	6	
3467	69.5	72	65.5	72	71	70	5	5	2.7	Cube 150mm (100%)	1	1	6	
3472	66.5	71	65.5	62.5	72	67.5	5	5	4	Cube 150mm (100%)	1	1	6	
3477	74	71.5	77.5	78.5	74.5	75.2	5	5	2.8	Cube 150mm (100%)	1	1	6	
3482	65.5	71	70.5	63	72	68.4	5	5	3.9	Cube 150mm (100%)	1	1	6	
3487	57.5	46	51	47.5	59.5	52.3	5	5	21.3	Cube 150mm (100%)	1	1	6	
3492	74	71.5	66.5	71	69	70.4	5	5	2.8	Cube 150mm (100%)	1	1	6	
3497	59	63.5	64	62.5	62	62.2	5	5	2	Cube 150mm (100%)	1	1	6	
3506	78	71	75.5	66.5	70.5	72.3	5	5	19.5	Cube 150mm (100%)	1	1	6	
3511	61.5	64.5	71.5	67.5	71	67.2	5	5	14.3	Cube 150mm (100%)	1	1	6	
3516	76	67	76.5	73	69.5	72.4	5	5	17.8	Cube 150mm (100%)	1	1	6	
3526	80	79	73	76.5	78	77.3	5	5	2.7	Cube 150mm (100%)	1	1	6	
3531	64.5	62	61.5	68	63	63.8	5	5	7.5	Cube 150mm (100%)	1	1	6	
3536	9	17.5	13	13		13.125	4	4	3.5	Cube 150mm (100%)	1	1	6	
3540	72.5	70.5	73	72	73	72.2	5	5	4.3	Cube 150mm (100%)	1	1	6	
3545	51	53	52.5	47	62	53.1	5	5	9.5	Cube 150mm (100%)	1	1	6	

Shot count											Q	Valid	Total	Std dev.	Form	Form-Factc	Carb-Facto	Transect	Shot count						Q	Valid	Total	Std dev.	Form	Form-Factor	Carb-Factor	Transect	Letter
2563	70.5	69.5	72.5	73.5	73.5	76	72	72	76	70.5	76.3	10	10	2.2	Cylinder (82%)	0.8	0.96	7	2368	77.5	76	74	79	79	77.1	5	5	2.1	Cylinder (87%)	0.8	0.96	8	A
2601	74.5	67	76.5	76.5	72	71.5	75	78	72.5	74.5	73.5	10	10	3.2	Cylinder (82%)	0.8	0.96	7	2373	74	73.5	67	71.5	72.5	71.7	5	5	2.8	Cylinder (80%)	0.8	0.96	8	B
2616	79.5	76.5	76.5	79	72.5	72.5	77	78	75.5	77	73.3	10	10	2.4	Cylinder (87%)	0.8	0.96	7	2380	71	76.5	76.5	73.5	74	74.3	5	5	2.3	Cylinder (82%)	0.8	0.96	8	C
2627	73	72.5	75								67.3	3	3	1.3	Cylinder (82%)	0.8	0.96	7	2385	75.5	68	72.5	75	67	71.6	5	5	3.9	Cylinder (80%)	0.8	0.96	8	D
2651	69.5	77.5	76	74	78	65	78	68	74	74.5	73.8	10	10	4.5	Cylinder (82%)	0.8	0.96	7	2395	29.5	34	28.5	26	31	29.8	10	10	2.1	Cylinder (80%)	0.8	0.96	10	A
2661	64	68	72.5	61	60.5	73.5	66	69.5	70.5	66.5	72.8	10	10	4.5	Cylinder (82%)	0.8	0.96	7	2405	68	69	69.5	70	71	69.5	5	5	1.1	Cylinder (82%)	0.8	0.96	10	B
2675	79	73.5	72.5	77	73.5	69	78	73	68.5	67	63.0	10	10	4.1	Cylinder (82%)	0.8	0.96	7	2410	78.5	79.5	78.5	78	76.5	78.2	5	5	1.1	Cylinder (87%)	0.8	0.96	9	A
2687	74.5	66.5	73.5	75.5	73	73	76	70.5	72.5	76	72.9	10	10	2.9	Cylinder (82%)	0.8	0.96	7	2418	76.5	75	73.5	74	74	74.6	5	5	1.2	Cylinder (84%)	0.8	0.96	9	B
2697	62.5	64.5	60	67.5	61	63.5	61	63.5	64	67	69.4	10	10	2.5	Cylinder (82%)	0.8	0.96	7															
2721	71	77.5	71	76.5	68.5	75	75	70.5	72	77.5	75.3	10	10	3.2	Cylinder (82%)	0.8	0.96	7															
2731	68	61.5	72	67	70.5	73	69	73.5	70.5	68.5	68.1	10	10	3.5	Cylinder (82%)	0.8	0.96	7															
2745	71	76	78.5	74	77.5	76	75	75	75	68.5	72.3	10	10	3	Cylinder (84%)	0.8	0.96	7															
2755	68	66	62.5	62	65.5	72	74	70.5	72	74	78.5	10	10	4.5	Cylinder (82%)	0.8	0.96	7															
2768	73	73.5	74.5	69	70.5	70.5	73	70.5	76	66	59.7	10	10	2.9	Cylinder (80%)	0.8	0.96	7															
2781	70	76	82.5	78.5	80.5	80	80	78.5	80.5	76	78.3	10	10	3.5	Cylinder (87%)	0.8	0.96	7															
2794	66	60	57.5	61.5	58	56	59	60	59	66.5	72.9	10	10	3.5	Cylinder (78%)	0.8	0.96	7															
2805	74.5	71	74.5	72	79.5	78.5	79	73	80.5	70	74.0	10	10	3.8	Cylinder (87%)	0.8	0.96	7															
2827	75.5	73.5	73	68	77	76.5	68	73	71.5	66.5	75.6	10	10	3.7	Cylinder (82%)	0.8	0.96	7															
2854	71	76.5	71	74	73	77	75	73	75.5	76	72.1	10	10	2.2	Cylinder (82%)	0.8	0.96	7															
2867	78	74.5	76	66	79.5	80.5	73	80	72.5	69.5	70.2	10	10	4.8	Cylinder (84%)	0.8	0.96	7															
2879	68.5	71.5	72	72	75	74	76	72	67.5	75	71.6	10	10	2.8	Cylinder (82%)	0.8	0.96	7															
2890	62	71	69	71.5	70	68	74	68	78	69.5	70.8	10	10	4.2	Cylinder (80%)	0.8	0.96	7															
2902	72	71	74	70.5	72.5	70.5	75	64	75	75.5	66.3	10	10	3.4	Cylinder (80%)	0.8	0.96	7															
2913	75	74	72	69	72.5	70	68	70.5	66.5	67.5	76.1	10	10	2.8	Cylinder (80%)	0.8	0.96	7															
2923	73.5	67.5	69.5	69.5	62.5	60.5	63	67.5	63	69	71.2	10	10	4.1	Cylinder (83%)	0.8	0.96	7															
2940	83	75.5	76.5	83	70.5	71	75	75.5	75.5	73	71.6	10	10	4.3	Cylinder (87%)	0.8	0.96	7															
2958	74	71.5	71.5	68.5	72	69	76	69	70	67	72.2	10	10	2.6	Cylinder (80%)	0.8	0.96	7															
2968	63	75.5	71	76.5	71	70.5	74	70	73	76	63.9	10	10	4	Cylinder (80%)	0.8	0.96	7															
2978	67	69.5	69	78.5	72.5	69	78	74.5	71.5	73	76.3	10	10	3.9	Cylinder (82%)	0.8	0.96	7															
2990	64	61.5	64	61.5	68	65	62	64.5	65	62.5	68.2	10	10	2	Cylinder (82%)	0.8	0.96	7															
3004	75.5	76	79	76.5	76	77	77	75.5	74	78	76.2	10	10	1.4	Cylinder (87%)	0.8	0.96	7															
3017	66	68	71.5	69	68	70	69	62	70.5	66	62.9	10	10	2.7	Cylinder (82%)	0.8	0.96	7															
3035	79.5	73	76.5	78.5	71.5	75	79	81	72	75.5	70.1	10	10	3.3	Cylinder (87%)	0.8	0.96	7															
3048	60	59	56.5	67.5	59	65	69	62	68.5	62	64.3	10	10	4.3	Cylinder (80%)	0.8	0.96	7															
3062	73	71.5	70.5	72.5	71.5	65	65	71.5	71	67.5	71.1	10	10	3.1	Cylinder (80%)	0.8	0.96	7															
3075	67	64.5	62.5	69.5	70	60.5	64	61	60.5	64.5	68.7	10	10	3.5	Cylinder (82%)	0.8	0.96	7															
3086	65	75.5	70	68	73.5	73.5	73	71	71	68.5	73.3	10	10	3.1	Cylinder (80%)	0.8	0.96	7															
3096	70.5	66	71.5	73	71.5	70	66	69	60.5	69.5	64.6	10	10	3.7	Cylinder (82%)	0.8	0.96	7															
3124	71	73	77.5	81	70	71	67	75	74.5	76.5	70.1	10	10	4.1	Cylinder (82%)	0.8	0.96	7															
3169	61.5	67.5	69	72	60.5	60	68	61	61.5	65	73.2	10	10	4.3	Cylinder (82%)	0.8	0.96	7															
3193	67.5	69.5	72.5	71.5	63	75.5	72	75	64	69.5	67.0	10	10	4.2	Cylinder (80%)	0.8	0.96	7															
3228	78.5	73	81.5	67.5	76	84	64	67	67	86	69.5	10	10	7.9	Cylinder (84%)	0.8	0.96	7															
3241	60	67	69	69	61	64.5	70	72	70.5	74.5	72.6	10	10	4.7	Cylinder (82%)	0.8	0.96	7															
3257	68	79	73	64.5	60.5	72	68	73.5	67	67	66.4	10	10	5.2	Cylinder (82%)	0.8	0.96	7															
3267	72	75	76.5	76.5	74	65.5	74	71.5	68.5	77.5	71.9	10	10	3.8	Cylinder (82%)	0.8	0.96	7															
3277	66.5	67.5	67.5	65.5	65	67	68	69.5	61	63.5	67.3	10	10	2.5	Cylinder (83%)	0.8	0.96	7															
3294	66	74.5	75	67	67	80	75	75.5	67.5	64	69.5	10	10	5.4	Cylinder (80%)	0.8	0.96	7															
3323	60	73	63	69.5	72.5	71	67	64.5	65.5	72.5	68.2	10	10	5.2	Cylinder (82%)	0.8	0.96	7															
3336	71	72.5	68.5	70.5	62	68	66	74	73.5	70.5	69.6	10	10	4.5	Cylinder (82%)	0.8	0.96	7															
3348	63.5	66.5	74.5	71.5	64.5	67	72	70	65	69.5	68.4	10	10	3.6	Cylinder (82%)	0.8	0.96	7															

DEPTH (ft)	BI (Wang et al)	Rebound Factor	ln(E)	ln(U)	Young's Modulus(Mpa)	UCS(Mpa)	P-wave (m/s)	S-wave (m/s)
0		67.519	3.953	5.085	52.068	161.542	4387.912	2533.362
1	0.054	68.232	3.985	5.133	53.786	169.443	4470.621	2581.114
2	0.792	68.028	3.976	5.119	53.291	167.147	4446.832	2567.379
3	0.057	58.559	3.512	4.484	33.531	88.627	3469.801	2003.291
4	0.066	48.122	2.906	3.785	18.279	44.044	2639.685	1524.023
5	0.052	68.130	3.980	5.126	53.538	168.291	4458.710	2574.238
6	0.502	70.319	4.078	5.272	59.036	194.877	4721.916	2726.200
7	0.676	34.784	1.902	2.892	6.702	18.021	1861.147	1074.534
8	0.552	70.675	4.094	5.296	59.966	199.586	4766.211	2751.773
9	0.649	63.395	3.758	4.808	42.852	122.545	3938.548	2273.922
10	0.185	35.446	1.961	2.936	7.104	18.838	1893.701	1093.329
11	0.233	72.254	4.162	5.402	64.202	221.846	4967.421	2867.942
12	0.303	58.813	3.526	4.501	33.983	90.151	3493.019	2016.696
13	0.175	69.148	4.026	5.194	56.050	180.173	4579.255	2643.834
14	0.164	57.031	3.431	4.382	30.901	80.006	3333.697	1924.711
15	0.421	53.977	3.261	4.177	26.066	65.199	3077.297	1776.678
16	0.120	65.075	3.839	4.921	46.461	137.145	4115.783	2376.248
17	0.360	70.217	4.074	5.266	58.772	193.552	4709.337	2718.937
18	0.396	71.133	4.114	5.327	61.176	205.808	4823.772	2785.006
19	0.157	63.548	3.765	4.819	43.172	123.805	3954.340	2283.039
20	0.754	70.166	4.071	5.262	58.641	192.893	4703.059	2715.313
21	0.314	58.406	3.504	4.474	33.261	87.725	3455.944	1995.290
22	0.098	58.915	3.531	4.508	34.166	90.768	3502.350	2022.083
23	0.188	63.650	3.770	4.826	43.386	124.653	3964.903	2289.138
24	0.334	70.523	4.087	5.286	59.566	197.554	4747.177	2740.784
25	0.160	44.813	2.686	3.563	14.666	35.286	2420.466	1397.456
26	0.495	69.199	4.029	5.197	56.178	180.788	4585.367	2647.363
27	0.131	66.959	3.927	5.047	50.745	155.593	4324.001	2496.463
28	0.145	43.184	2.571	3.454	13.080	31.637	2319.327	1339.064
29	0.057	64.362	3.805	4.873	44.906	130.750	4039.639	2332.286
30	0.583	59.577	3.566	4.553	35.366	94.884	3563.610	2057.451
31	0.435	67.723	3.962	5.098	52.555	163.761	4411.385	2546.915
32	0.194	54.995	3.318	4.246	27.616	69.802	3160.494	1824.712
33	0.157	60.595	3.618	4.621	37.268	101.583	3659.955	2113.076
34	0.244	67.773	3.964	5.102	52.677	164.321	4417.273	2550.314
35		69.606	4.047	5.225	57.206	185.790	4634.559	2675.764

DEPTH (ft)	BI (Wang et al)	rebound factor	ln(E)	ln(U)	Youngs Modulus(Mpa)	UCS (Mpa)	P-wave (m/s)	S-wave (m/s)
0	0.521	65.177	3.843	4.928	46.686	138.084	4126.777	2382.596
6	0.148	67.723	3.962	5.098	52.555	163.761	4411.385	2546.915
12	0.502	54.588	3.295	4.218	26.988	67.923	3126.948	1805.344
17	0.226	70.064	4.067	5.255	58.378	191.582	4690.530	2708.079
20	0.739	65.788	3.872	4.969	48.052	143.853	4193.362	2421.039
40	0.233	54.384	3.284	4.205	26.679	67.003	3110.309	1795.738
64	0.698	66.603	3.910	5.023	49.915	151.922	4283.816	2473.262
100	0.237	54.791	3.307	4.232	27.301	68.856	3143.676	1815.002
136	0.749	59.170	3.545	4.525	34.624	92.330	3525.786	2035.613
148	0.241	58.253	3.496	4.464	32.993	86.831	3442.143	1987.322
163	0.687	64.261	3.800	4.866	44.686	129.861	4028.876	2326.073
175	0.043	9.685	-2.050	1.210	0.129	3.353	964.263	556.718
190	0.689	58.864	3.529	4.505	34.074	90.459	3497.681	2019.387
202	0.281	45.628	2.741	3.618	15.506	37.265	2472.677	1427.601
214	0.681	64.566	3.814	4.887	45.346	132.546	4061.249	2344.763
238	0.251	61.512	3.665	4.682	39.037	108.015	3748.891	2164.423
262	0.434	58.966	3.534	4.512	34.257	91.079	3507.025	2024.782
290	0.316	66.806	3.920	5.037	50.388	154.009	4306.733	2486.494
314	0.636	59.882	3.582	4.573	35.929	96.846	3592.244	2073.983
329	0.229	43.489	2.593	3.475	13.368	32.291	2337.963	1349.824
341	0.653	61.919	3.685	4.710	39.842	111.003	3789.109	2187.643
352	0.282	53.570	3.237	4.150	25.463	63.444	3044.634	1757.820
376	0.723	63.853	3.780	4.839	43.817	126.365	3986.114	2301.384
384	0.178	58.661	3.518	4.491	33.711	89.233	3479.070	2008.642
399	0.728	63.955	3.785	4.846	44.033	127.230	3996.762	2307.532
406	0.271	68.944	4.017	5.180	55.541	177.731	4554.888	2629.766
416	0.819	55.199	3.330	4.259	27.933	70.761	3177.401	1834.474
431	0.236	3.601	-5.107	0.802	0.006	2.231	822.189	474.691
446	0.759	63.752	3.775	4.832	43.601	125.506	3975.494	2295.253
461	0.178	44.304	2.650	3.529	14.157	34.102	2388.395	1378.940

`

DEPTH(ft)	BI	Rebound Factor	ln(E)	ln(U)	Youngs Modulus (Mpa)	UCS (Mpa)	P-wave(m/s)	S-wave (m/s)
		60.19	3.597	4.594	36.499	98.848	3621.108	2090.648
		64.57	3.814	4.887	45.346	132.546	4061.249	2344.763
		61.31	3.654	4.669	38.639	106.551	3728.943	2152.906
		62.99	3.738	4.781	42.007	119.246	3896.745	2249.787
		55.56	3.350	4.283	28.494	72.471	3207.207	1851.682
		65.33	3.851	4.938	47.025	139.504	4143.323	2392.149
		60.34	3.605	4.604	36.786	99.865	3635.627	2099.030
0	0.250	64.16	3.795	4.860	44.468	128.978	4018.143	2319.876
13	0.753	65.38	3.853	4.942	47.138	139.981	4148.854	2395.342
24	0.214	67.98	3.973	5.115	53.168		4440.904	2563.957
30	0.725	65.08	3.839	4.921	46.461	137.145	4115.783	2376.248
46	0.132	64.97	3.834	4.914	46.236	136.213	4104.818	2369.918
57.5	0.810	58.66	3.518	4.491	33.711	89.233	3479.070	2008.642
64.5	0.336	64.67	3.819	4.894	45.568	133.453	4072.098	2351.027
77.5	0.757	64.67	3.819	4.894	45.568	133.453	4072.098	2351.027
93	0.188	54.79	3.307	4.232	27.301	68.856	3143.676	1815.002
109	0.804	64.97	3.834	4.914	46.236	136.213	4104.818	2369.918
121	0.354	60.80	3.628	4.635	37.656	102.978	3679.535	2124.380
138	0.783	66.25	3.894	4.999	49.094	148.338	4244.005	2450.277
149	0.241	60.14	3.595	4.590	36.404	98.512	3616.282	2087.861
154	0.648	63.19	3.748	4.795	42.428	120.884	3917.591	2261.822
159	0.238	69.91	4.060	5.245	57.986		4671.798	2697.264
169.5	0.118	51.69	3.127	4.024	22.796	55.922	2898.022	1673.174
175.5	0.710	66.81	3.920	5.037	50.388	154.009	4306.733	2486.494
178.5	0.274	63.80	3.778	4.836	43.709	125.935	3980.801	2298.316
190	0.661	65.79	3.872	4.969	48.052	143.853	4193.362	2421.039
194	0.227	66.55	3.908	5.020	49.797	151.405	4278.106	2469.966
199.5	0.802	63.90	3.782	4.843	43.925	126.797	3991.434	2304.456
213	0.206	61.61	3.670	4.689	39.238	108.754	3758.905	2170.205
216.75	0.805	63.50	3.763	4.815	43.065	123.384	3949.069	2279.996
219.25	0.278	62.02	3.690	4.716	40.045	111.763	3799.230	2193.487
225.5	0.765	58.00	3.483	4.447	32.549	85.363	3419.263	1974.112
228.5	0.752	67.42	3.948	5.078	51.826	160.444	4376.222	2526.613
231	0.246	62.33	3.705	4.737	40.658	114.074	3829.758	2211.112
233.75	0.202	63.60	3.768	4.822	43.279	124.228	3959.618	2286.087
239.25	0.821	63.80	3.778	4.836	43.709	125.935	3980.801	2298.316
244.75	0.179	55.20	3.330	4.259	27.933	70.761	3177.401	1834.474
253.75	0.832	68.08	3.978	5.122	53.415	167.718	4452.767	2570.806
255.25	0.148	59.42	3.558	4.542	35.086	93.918	3549.379	2049.235
265.25	0.754	67.77	3.964	5.102	52.677	164.321	4417.273	2550.314
268.25	0.199	54.18	3.272	4.191	26.371	66.095	3093.759	1786.183
278.25	0.739	61.36	3.657	4.672	38.739	106.915	3733.920	2155.780
280.25	0.175	55.76	3.361	4.297	28.818	73.467	3224.365	1861.588
289.25	0.813	62.38	3.708	4.740	40.760	114.464	3834.869	2214.063
294.25	0.119	60.24	3.600	4.597	36.594	99.186	3625.942	2093.438
304.25	0.786	65.23	3.846	4.931	46.798	138.556	4132.285	2385.776
309.75	0.198	56.01	3.375	4.314	29.227	74.730	3245.940	1874.045
316.75	0.261	61.51	3.665	4.682	39.037	108.015	3748.891	2164.423
328.75	0.322	66.04	3.884	4.986	48.629	146.327	4221.422	2437.239
331.25	0.296	59.22	3.547	4.529	34.716	92.645	3530.492	2038.330
338.25	0.822	60.75	3.626	4.631	37.559	102.628	3674.630	2121.549
344.25	0.160	64.67	3.819	4.894	45.568	133.453	4072.098	2351.027
349.25	0.184	57.54	3.458	4.416	31.761	82.782	3378.461	1950.556
355.25	0.804	62.63	3.720	4.757	41.277	116.433	3860.530	2228.878
358.25	0.833	59.32	3.553	4.536	34.901	93.279	3539.923	2043.775
359.75	0.151	61.10	3.644	4.655	38.244	105.107	3709.100	2141.450
367.75	0.140	59.83	3.579	4.570	35.835	96.516	3587.456	2071.219